EXPERIMENTAL ANALYSIS AND MODEL DEVELOPMENT OF DUAL MODE, TURBULENT JET IGNITION (DM-TJI) ENGINE OPERATING WITH GASOLINE AND ALTERNATIVE FUELS

By

Yidnekachew Messele Ayele

A DISSERTATION

Submitted to
Michigan State University
in partial fulfillment of the requirements
for the degree of

Mechanical Engineering - Doctor of Philosophy

2022

ABSTRACT

EXPERIMENTAL ANALYSIS AND MODEL DEVELOPMENT OF DUAL MODE, TURBULENT JET IGNITION (DM-TJI) ENGINE OPERATING WITH GASOLINE AND ALTERNATIVE FUELS

By

Yidnekachew Messele Ayele

Gasoline fuel is the most convenient energy source for light-duty vehicles in energy density and refueling time. However, the emission regulations for internal combustion engines force the industry to exploit innovative combustion technologies. The spark-ignition engine was forced to be cleaner and more efficient, changing from regular combustion engines to a more advanced internal combustion engine and electrification. The current scenario shows that automotive companies and researchers are exploring hybrid powertrains with advanced internal combustion engine technologies with electrification or pure electric vehicles. The Dual Mode, Turbulent Jet Ignition (DM-TJI) system is one of the promising advanced combustion systems, powered by active air/fuel scavenging pre-chamber ignition systems. The distributed ignition sites created by the pre-chamber flames improve the combustion engine's efficiency, simultaneously mitigating combustion knock at a high engine compression ratio and enabling lean-burn or high level of external EGR dilution operation. This study analyzes the performance of a single-cylinder DM-TJI metal engine with gasoline and alternative fuels.

The first part of the study presents the experimental investigations on three pre-chamber nozzle orifice diameters at various engine speeds and 10 bar engine load. The combustion parameters for each tested orifice diameter are presented for the incremental engine speeds. A numerical analysis was conducted using the GT-Power model simulation tool to support the experimental result. The DM-TJI engine's maximum gross indicated efficiency was examined and found to be 44.56%, with a higher EGR dilution rate of 45%. This orifice diameter study reported on the first published results of the desertion. Additional experimental data were collected for the selected orifice diameter at a wide range of engine operating test matrices. A predictive engine model was introduced with experimental data validation. The experimental data and predictive model generated the engine performance and fuel map for a real-world fuel economy study. Conventional and hybrid powertrain vehicles were developed with GT-Suite commercial software. Each powertrain model was calibrated in terms of components (battery, electric motors) capacity, internal combustion engine operative points, energy management strategy, and gear ratios with chassis dynamometer measured data of the vehicle drive cycle. A selected U.S. Environmental Protection Agency (EPA) driving schedule was implemented on the GT-Suite powertrain. The DM-TJI engine drive cycle fuel economy is compared to an industry-based conventional vehicle with the same powertrain except for the engine map. The results show the DM-TJI engine fuel economy improvement between 10.5%-17.29% and CO2 emissions reductions between 9.51%-14.75% for the selected driving schedule. Mild and parallel hybrid powertrain further improve the fuel economy by 9.23% and 29.88%, respectively, compared to the conventional powertrain of the DM-TJI engine. The CO2 emission was reduced by 23%.

Finally, the single-cylinder DM-TJI metal engine performance under different alternative fuels was studied. An experimental test was carried out at stoichiometric conditions with different fuels, engine speed, engine load, and EGR dilution rates. Compared to gasoline fuel, E80 ethanol blend fuel produces 4.47% less CO2 and 25.75% less CO emission, and methane fuel produces 27.91% less CO2 and 57.85% less CO emission. E80 ethanol blend has the highest indicated efficiency of 45.61% with 45% EGR dilution. Methane fuel has a maximum indicated efficiency of 45.03% with 38.5% EGR dilution.

ACKNOWLEDGEMENTS

First and foremost, I would like to express my gratitude to my adviser Prof. Harold Schock for giving me the opportunity to be his student and his continuous support. I learned from him through direct comments and leadership. I would also like to thank my committee members, Prof. George Zhu, Prof. Elisa Toulson, and Prof. Elias Strangas for their comment and guidance. I am grateful to Thomas Stuecken for his novel technical advice and enjoyable lab sessions. I would like to show my sincerest gratitude to Professor Abraham Engeda for all the support and his mentoring during my first year. I would like to acknowledge Kevin Moran, Jennifer Higel, Brian Rowley, John Przybyl and Brian Deimling for their technical support during different stages of my work. I would also like to acknowledge Dale Pickelman of Hanon Systems for his technical support. Special thanks to the current and former graduate students: Dr. Mekuannint Messele, Dr. Sedigheh Tolou, Dr. Cyrus Atis Arupratan, Dr. Sabah Sadiyah Chowdhury and Daniel Nicklowitz for all the support and sharing their knowledge.

I would like to express my gratitude to my family back in Ethiopia – my mother, my father, and my siblings for their love and unwavering support throughout this endeavor ‘አመሰግናለሁ’. I know that this is a proud moment for them too. Finally, I would like to thank my wife Hilawit Worku for her constant guidance and tireless support throughout my personal and professional life. I have been the most fortunate to have you alongside me through this seemed-to-be endless journey at times. Thank you for being there every step of the way.

TABLE OF CONTENTS

LIST OF TABLES

LIST OF FIGURES

KEY TO ABBREVIATIONS

ALPHA	Advanced light-duty powertrain and hybrid analysis
ANL	Argonne national laboratory
aTDCF	After top dead center firing
aTDCGE	After top dead center gas exchange
BEV	Battery electric vehicles
BMEP	Brake mean effective pressure
BMS	Battery management system
BSFC	Brake specific fuel consumption
bTDCF	Before top dead center firing
bTDCGE	Before top dead center gas exchange
BTE	Brake thermal efficiency
CA50	Combustion phasing
CAC	Charge air cooler
CAD	Crank angle degree
CAFF	Corporate average fuel economy
CAS	Combustion analysis system
CFD	Computational fluid dynamics
CNG	Compressed natural gas
CO	Carbon monoxide
CO2	Carbon dioxide
$\mathrm{COV_{IMEP}}$	Coefficient of variation of $IMEP_g$

CPOA	Cylinder pressure only analysis
CR	Compression ratio
DI	Direct injector
DM-TJI	Dual mode turbulent jet ignition
ECM	Equivalent circuit models
ECU	Engine controller unite
ECU	Engine controller unit
EGR	Exhaust gas recirculation
EM	Electrical motor
EPA	Environmental protection agency
EV	Electric vehicle
FAS	Flywheel alternator starter
FMEP	Friction mean effective pressure
FTP	Federal test procedure
GHG	Greenhouse gas
HC	Unburned hydrocarbons
HEV	Hybrid electric vehicle
HIL	Hardware-in-the-loop
HRR	Heat release rate
HWFET	Highway fuel economy test procedure
ICCT	International council on clean transport
ICE	Internal combustion engine
IMEPg	Indicated gross mean effective pressure

ISNOx	Indicated specific nitrogen oxides
LDVs	Light-duty vehicles
LFE	Laminar flow element
LNG	Liquefied natural gas
MBF	Mass burn fraction
MBT	Maximum brake torque
NG	Natural gas
NI	National instruments
NOx	Oxides of nitrogen
NVFEL	National vehicle and fuel emissions laboratory
OCV	Open-circuit voltage
PFI	Port fuel injector
PM	Particulate matter representing carbon particles or soot
POD	Pressure oscillation difference
RCM	Rapid compression machine
RMS	Root mean square
SDK	Software development kit
SI	Spark ignition
SoC	Start of combustion
SOC	State of charge
TCU	Transmission controller unit
TDC	Top dead center
TJI	Turbulent jet ignition

TPA	Three pressure analysis
TWC	Three-way catalyst
UDDS	Urban dynamometer driving schedule
US	United States
VSC	Vehicle supervisor control
WLTC	Worldwide harmonized light vehicles cycle

Chapter 1: Introduction

1.1 Motivation

Vehicle manufacturing is one of the most regulated industries in the world and is required to meet legislation worldwide that controls all aspects of the product. Emissions regulations were first introduced in the 1970s to control exhaust pollutants. The regulated gases measured during prescribed tests control NOx (oxides of nitrogen), CO (carbon monoxide), HC (unburned hydrocarbons), and PM (particulate matter representing carbon particles or soot). Carbon dioxide was also measured correlating to fuel consumption during the test [1]. Environmental degradation is a global reality that the world faces today. It is mainly due to continuous and uncontrolled emissions of hazardous and polluting elements to the atmosphere from various segments of human activities. The transportation sector consumes nearly one-quarter of primary energy globally. Passenger transportation, especially light-duty vehicles, is responsible for most transportation energy use [2]. Emissions from the transport sector are a significant contributor to climate change, with about 14% of annual (2010) emissions (including non-CO2 gases) and around a quarter of CO2 emissions from burning fossil fuels. Almost all (95%) of the world's transportation energy comes from petroleum-based fuels, primarily gasoline and diesel [3].

The global number of cars on the road will nearly double by 2040 [4]. Significant fuel economy improvements are required to stabilize and reduce greenhouse gas emissions. The transportation sector has witnessed many technological advancements to enhance fuel efficiency and reduce vehicle emissions. Stringent fuel economy and emissions regulations have initiated these regulations that stem from increasing concerns over greenhouse gas emissions, depleting air quality, and fossil-based resource depletion. Among these technologies, advanced combustion engine, electric vehicle (EV) and hybrid electric vehicle (HEV) powertrains has been widely implemented in the automotive industry.

Throughout the years, the electric and hybrid vehicle market has grown. Influenced by government regulations and consumer demand, auto manufacturers have continued to pursue technologies to improve efficiency and fuel economy [5]. Moreover, EVs still require significant technological development and infrastructural integration before they become commercially viable, which leads to HEV being a better investment for the transition period. In addition to the conventional internal combustion engine (ICE), HEV powertrains are characterized by a secondary electric energy storage device (batteries) and electric propulsion motors, leading to higher operational efficiency. Fuel efficiency is the key benefit of HEVs, and this can be achieved by downsizing engines, optimizing engine operations, improving acceleration performance, recovering kinetic energy during deceleration and coasting, turning off the engine during standstill, and utilizing the electric energy stored in the battery.

1.2 Background

The automotive industry is facing extraordinary challenges due to energy and environmental issues. Growing concerns about global warming and energy security have led to stringent fuel efficiency and CO2 emission standards for new passenger vehicles. As the push for green energy continues to gain momentum in today’s industry, the automotive industry primarily focuses on developing a fuel-efficient, clean, and sustainable transportation system.

Various vehicle standards worldwide can play an essential role in addressing the problem. The goal of fuel economy standards to limit the amount of carbon dioxide emitted by vehicles is crucial to mitigate global warming. There is a great deal of policy activity around the world. Ten years ago, only four governments had introduced mandatory greenhouse gas (GHG) emission/fuel economy standards. Today, ten governments have established fuel economy or GHG emission standards for light-duty vehicles (LDVs). All are among the top 15 vehicle markets worldwide: nearly 80% of new LDVs sold globally are currently subject to GHG emission or fuel economy standards.

Fuel economy standards progress and target are reviewed in the International Council on Clean Transport (ICCT) report. The review adopts reference standards corresponding to two of the most common ways to measure and regulate fuel consumption and GHG emissions from passenger vehicles. The European Union requires the fleet CO2 emissions of light-duty vehicles to be below 95 g/km and 145 g/km for light commercial vehicles, corresponding to average fuel consumption of 4.1 L/100 km for petrol-fueled vehicles and 3.6 L/100 km for those with Diesel engines, respectively [6,7]. In the United States (US), a CO_2 target of 109 g per km is intended for 2020. The US set a requirement of 54.5 MPG fleet-wide Corporate Average Fuel Economy (CAFE) by 2025. The actual and projected fleet average fuel economy of the world's major countries from 2000 to 2030 are shown in Figure 1.1 and Figure 1.2.

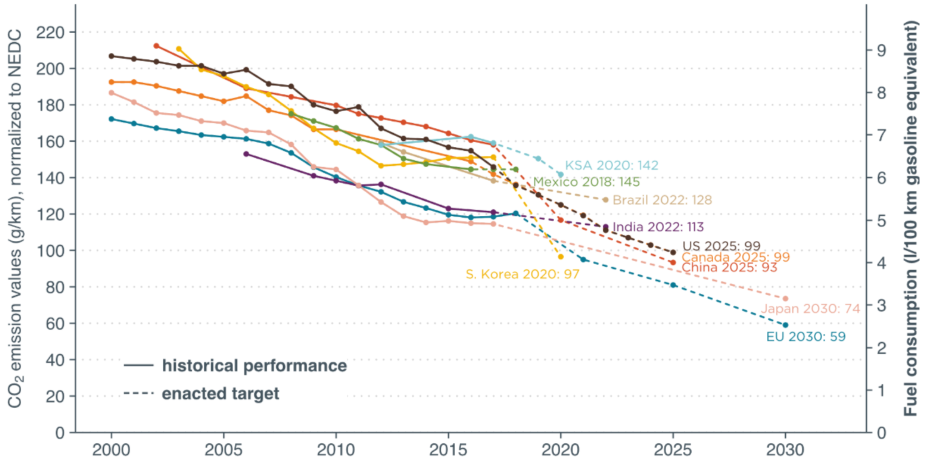

Figure 1.1 *Passenger car CO2 emission and fuel consumption values, normalized to NEDC* [8].

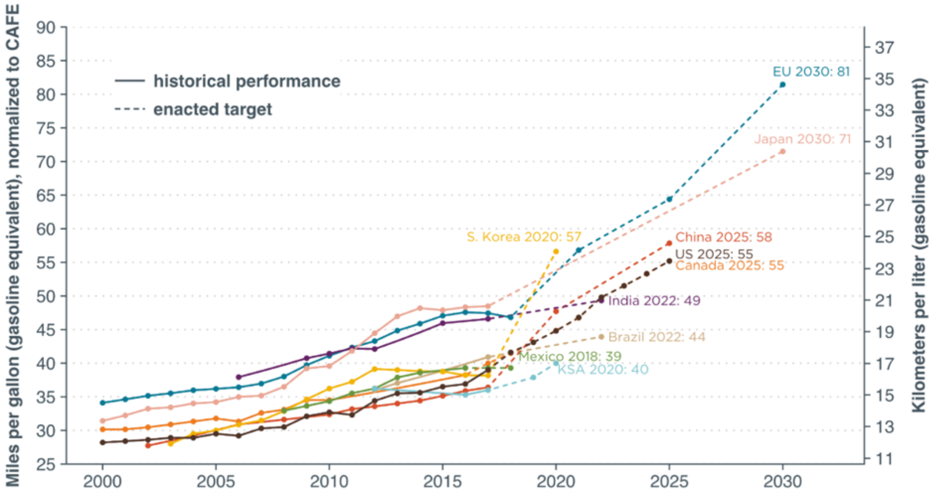

Figure 1.2 *Passenger car fuel economy, normalized to CAFE [7]*

When all vehicle technology contributions to low-carbon targets are included, it is estimated that vehicle technology advances might deliver around 10% of the overall decrease. The remaining 90% of the target is to be achieved by powertrain technology [9]. Change from ICE vehicles to battery electric vehicles (BEV) or electric motors (electrified powertrains) have zero tailpipe emissions, but they face associated challenges such as high battery costs and low driving ranges. In addition, a lack of electrical energy from clean sources, rejection of users to the change, and lack of infrastructure introduce new problems [6,10]. Therefore, hybrid drive train technologies are considered short and mid-term solutions to reducing automobile fuel consumption and emissions without compromising vehicle performance.

1.3 Hybrid Electric Vehicles

The concept of HEV is almost as old as the automobile itself. The first hybrid vehicles reported were shown at the Paris Salon of 1899 [11]. The vehicle was a parallel hybrid with a gasoline engine, assisted by an electric motor and lead-acid batteries. When the driving power required was higher than the engine rating, the electric motor provided additional power.

In the past decade, EV and HEV research accelerated due to oil prices and environmental concerns. The technologies have been improved significantly in battery technology. They offer solutions to critical issues related to today's conventional vehicles by diversification of energy resources, drive load equalization, improved sustainability, quiet operation, lower operating costs, and considerably lower emissions during operation without high extra cost.

Normalized energy flow for various vehicle configurations of ICE and HEV can be compared as shown in Figure 1.3. It can be observed that HEV achieves higher fuel efficiency through utilizing the energy lost during engine idle-stop, brake regeneration, and ensuring the ideal operating range for the engine [12]. HEVs can save 23%–49% more fuel than their conventional ICE counterparts [13]. HEVs can be classified into three categories based on their design characteristics: series, parallel, and a combination of both series-parallel (power-split) [14]. If we categorize the hybrid vehicles by their ability to charge from the grid, there are two types: the conventional HEV and plug-in HEV. There is no fundamental difference between the conventional HEV and plug-in HEV in the power train and mechanical connections. Based on the degree of electrification, HEVs can be classified as Micro, Mild, and Full or Strong Hybrid [15,16]. Micro-hybrids incorporate only a simple "Start&Stop" function for the ICE system that removes idling fuel consumption using a small integrated alternator/starter to shut down the engine when the vehicle comes to a complete stop and start it up when the driver releases the brake pedal. Once the vehicle is in motion, the ICE propels the vehicle and permits some energy recovery during braking. The main benefit of such a characteristic is the opportunity to recover part of the brake energy during vehicle deceleration phases. This energy is usually wasted in conventional powertrains. While full hybrids can significantly reduce fuel consumption, they use high-voltage powertrains with robust electrical motor and require additional components, including extra safety features [10]. This increases the complexity of the powertrain's design, and cost presents a barrier to widespread adoption. In between the two extremes, mild hybrid can recuperate a significant amount of energy at a lower cost with the following advantages: higher power to weight ratio, lower risk factor owing to lower operating voltage, easy mechanical integration on production vehicles, and no requirement for a complex energy management control strategy compared to a full HEV.

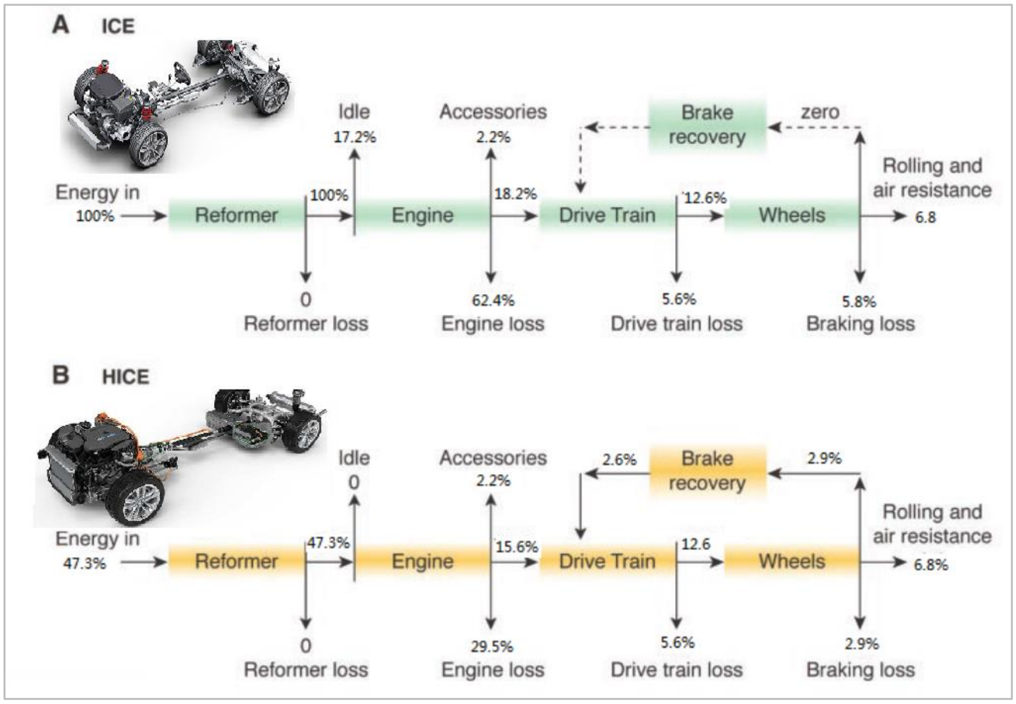

Figure 1.3 *Energy flow for various vehicle configurations with the same effective wheel propulsion. (A) Baseline ICE powertrain, (B) Hybrid vehicle that includes an electric motor and a parallel drive train [13].*

Mild hybrids vehicles use engine downsizing while meeting the power demand at the wheels, low-load electric driving to deliver power to the wheels, engine start-stop to remove idling fuel consumption, and series regenerative braking to achieve high fuel economy [17]. The most popular of such advantages is the possibility of downsizing the original internal combustion engine while meeting the power demand at the wheels. In turn, a smaller engine can be loaded closer to its maximum-efficiency curve, which is close to its maximum torque curve. This advantage is brought about by the capability of the hybrid powertrain to deliver power to the wheels from both the internal combustion engine and the electric motor. This power delivery assist in the propulsion maintains acceleration performance of the vehicle. Mild hybrids vehicles technology can be used with different engine types, including CI, SI, and HCCI engines which may also run on different fuels [10].

A traditional mild hybrid system consists of an electric motor connected to the engine crankshaft using a belt drive. The remaining drive train from the engine through the wheel remains the same as the conventional vehicle. Currently, there are five standard HEV layouts. Namely: P0 – Electrical motor (EM) at the front end of the engine, P1 – EM on the crankshaft between the engine and Clutch, P2 – EM at the input of the gearbox, P3 – EM at the output of the gearbox, and P4 – EM at the axle which has no mechanical connection to the driveline. All the different hybrid layouts schematically represented in Figure 1.4 with the conventional mid-size passenger vehicle architecture (Architecture A), equipped with an internal combustion engine and transmission, and assumed as the reference architecture to evaluate the potentialities of different hybrids powertrains.

Architecture B is a P0 system corresponding to a micro-hybrid, an EM coupled to the engine crankshaft by a belt featuring a Belt Alternator Starter, allowing the replacement of the engine starter of a conventional vehicle. The tractive energy of the vehicle available during deceleration is transferred to the electric machine to charge the battery. However, there are energy losses during the regenerative brake energy recovery process. The primary source of energy losses is due to engine inertia, engine friction, inverter losses, and belt-pulley system losses [18]. Depending on the size of the electric machine, different power management strategies may be enabled. In particular, with the low power machine, ‘Start&Stop’ regenerative braking and electric boosting (i.e. power assist during acceleration) can be performed [19].

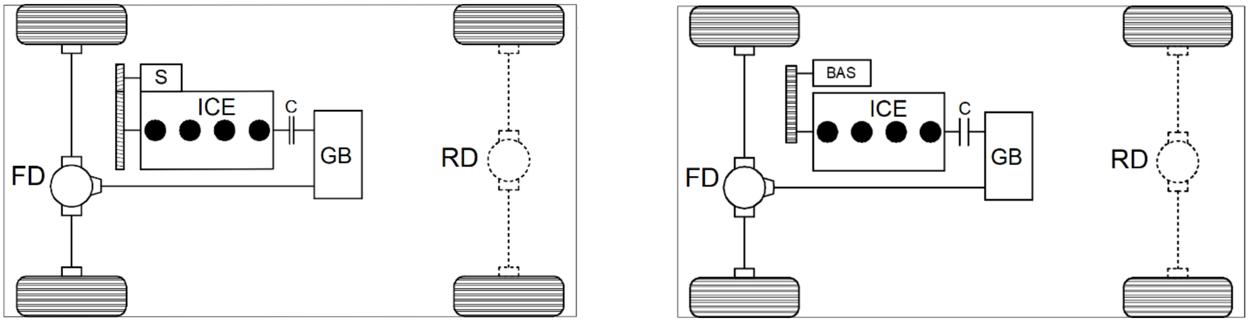

Architecture A

Architecture B (P0)

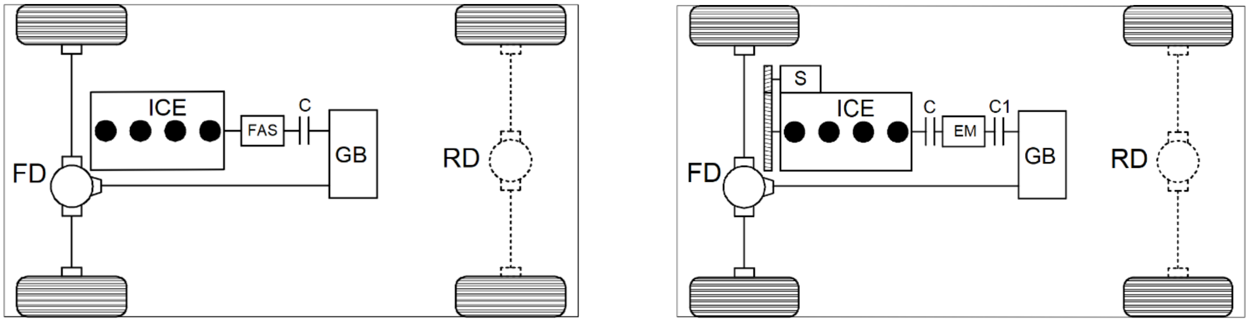

Architecture C (P1)

Architecture D (P2)

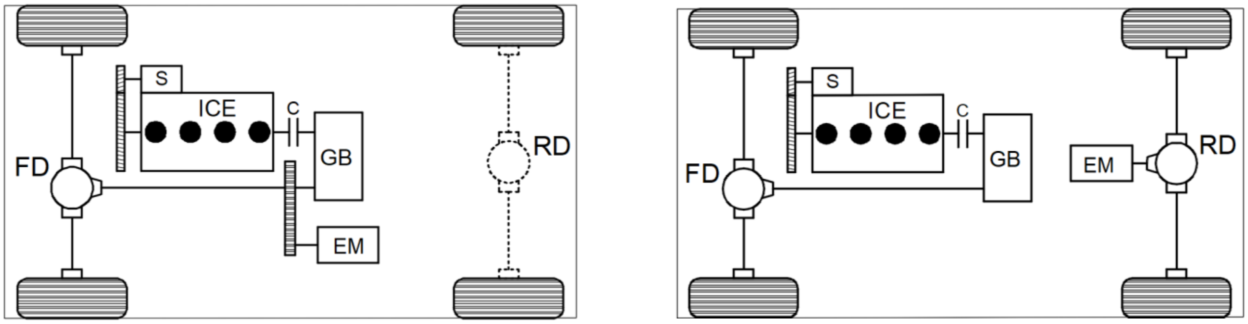

Architecture E (P3)

Architecture F (P4)

Figure 1.4 *Schematic representation of reference conventional powertrain (A) and HEV architectures (B, C, D, E and F)*

In a P1 architecture, the EM directly mounted on the crankshaft between the ICE and the gearbox removes the belt's limitation, usually called Flywheel Alternator Starter (FAS). It also can supply torque to assist the engine and recuperation energy during the braking. Similar to the P0, P1 has comparatively lower efficiency. The EM always has to overcome the engine drag torque. P1 machines are not usually geared to the engine; hence the machine design and topology will differ from a typical P0 machine [20].

P2 architecture used two clutches on the powertrain; the first clutch (C in Figure 1.4) is located between ICE and FAS, the second clutch (C1 in Figure 1.4) is located between FAS and the gearbox. During regenerative braking or pure electric drive, the electric motor is not forced to drag the engine's torque. The P2 layout has a unique advantage; the EM can work at high-efficiency points for more of the engine cycle; the different gear ratios in the gearbox allow the EM operating point to be better matched to the vehicle speed [20]. On the other hand, the increase in the powertrain length caused by the additional clutch might make architecture P2 unsuitable for transversal mounting, which is the standard solution for this passenger car class [21].

P3 architecture is similar to the P2, except the EM placed at the gearbox's output coupled with a fixed transmission ratio. The EM must be designed with quite different features because P3 architecture does not use the main transmission's variable gear ratio. The EM speed range should cover the whole vehicle speed range (unless an additional disconnect device is included). On the other hand, the gearbox can be neutral to reduce the inertia losses [20].

In P4 architecture, the EM is mounted at the rear differential and becomes an electrical axle, which experiences pure EV operation. Compare to the rest of the architecture, the efficiency of P4 is higher on electric drive and regenerative brake operation because it is free from engine drag torque, gearbox losses, and inertia. P4 architecture has a single gear ratio which limits the EM speed in a range, and EM may not always work at the most efficient possible operating points [20]. To make the P4 architecture more efficient, it is possible to combine with P0 or P1 and to gain the advantage of direct battery charging.

1.4 High Efficiency IC Engines

HEVs can be considered a potential technology to promote electric drive and emission reduction depending on the extent of their mode of use, vehicle design, and electric source. However, the primary power share of the HEVs is produced by ICE. With the frequent stops and restarts of the engines, the lowered exhaust gas temperature, and reduced effectiveness of the oxidation catalyst, HEVs showed no reduction in emissions compared to the conventional ICE vehicles [13]. The target of 75 g CO2/km tailpipe emissions could not be achieved with HEV and standard gasoline engine in a typical compact class passenger car [10]. Without improved thermal efficiency and reduced exhaust emission of ICE, hybridization will not give us the leverage to meet the regulation emission standards

Burning air-fuel mixtures that are lean or diluted with exhaust gases has shown the capability to improve spark ignition engines' efficiency and fuel consumption through higher mixture-specific heat ratio and reduced heat loss due to lower in-cylinder temperature, as well as reduced pumping loss. In addition to that, a lean operation can reduce NOx emissions by facilitating low-temperature combustion [22]. However, the lean limit is restricted to the capability of the ignition system to reliably ignite the fuel-lean mixture combustion stability, due to the less favorable ignition quality of the mixture and the slow flame propagation through the lower temperature lean mixture. Poor combustion stability increases HC and CO emissions due to misfire and partial burning cycles, while power output substantially decreases [23,24]. Several ignitions and combustion strategies have been investigated in the past to achieve lean-burn engine operation. Among all combustion enhancement systems, implementing higher energy distributed ignition sources, which led to the development of modern pre-chamber combustion-initiated systems, is one of the most successful technologies that have been extensively studied.

Turbulent Jet Ignition (TJI) is an ignition improvement method for the combustion of ultra-lean and low-temperature mixtures by replacing the spark plug in a standard spark ignition engine with a pre-chamber that initiates combustion. The TJI system is a modern pre-chamber-based jet ignition system characterized by small pre-chamber volume (<3% of the clearance volume), auxiliary pre-chamber fueling, and multiple small orifices connecting the main and the pre-chamber [25]. Most TJI systems consist of a pre-chamber and main chamber connected with one or more small orifices. Combustion is initiated in the pre-chamber using conventional Spark Ignition (SI), which causes a high-pressure increase and forces the hot products of combustion to discharge through one or more small orifices into the main chamber, which enables fast burn rates due to the ignition system producing multiple widely distributed ignition sites and consumes the main charge rapidly with minimal combustion variability. The distributed ignition sites enable relatively small flame travel distances enabling short combustion durations and high burn rates through a complex coupling of turbulence generation, chemical kinetics, and thermal effects [26–28]. The fast burn rates allow for increased levels of dilution compared to conventional spark ignition combustion. Additionally, the system has been developed to operate on readily available commercial fuels (gasoline, propane, natural gas) [26,29].

The TJI combustion system's primary challenge is maintaining combustion stability inside the pre-chamber with high exhaust gas recirculation (EGR) intake charge dilution. The Dual Mode, Turbulent Jet Ignition (DM-TJI) system is a combustion technology where an auxiliary fresh air supply apart from an auxiliary fuel is provided into the pre-chamber [25,30]. The main modification of the TJI system is the supplementary air supply and its method of delivery to the pre-chamber. The DM-TJI engine provides high EGR diluted boosted application with high knock limit and better gross indicated efficiency. This makes it a preferable choice for hybrid powertrain applications.

1.5 Objective

The pre-chamber ignition concept was studied at Michigan State University for nearly two decades. The efforts resulted in a granted patent describing an internal combustion engine that implemented a Dual Mode, Turbulent Jet Ignition (JETFIRE®). The ignition system is contained in what is termed a Jetfire® cartridge. The previous research contribution plays a significant role in the success of the DM-TJI engine system. Vedula et al. [31] reported the net indicated thermal efficiency of the first optical engine prototype DM-TJI engine for both lean and 30% nitrogen diluted, near stoichiometric operation. He also studied the effect of pre-chamber fuel injection timing, including pre-chamber air injection and different injection pressures on iso-octane/air combustion in a DM-TJI system equipped rapid compression machine for a global lambda of 3.0. Tolou et al. [32] developed a physics-based GT-Power model of the Prototype II DM-TJI system and predicted the ancillary work required to operate the additional components of the DM-TJI system. Atis et al. [33] demonstrate up to 50% external EGR (v/v) dilution rate with the Prototype III DM-TJI or the Jetfire® cartridge equipped metal engine at 1500 rpm engine speed.

In this dissertation, the performance of the single-cylinder Prototype III DM-TJI metal engine evaluates at different engine speeds and orifice diameters. The experimental result and numerical combustion model were used to generate a four-cylinder engine configuration performance and fuel map. Conventional and hybrid vehicles were developed, and the drive cycle fuel economy was studied. Finally, the DM-TJI metal engine fuel flexibility was studied with E80 ethanol blend and methane alternative fuels. The alternative fuel EGR tolerance limit and maximum fuel efficiency were evaluated. The exhaust emission compared between the fuels.

1.6 Thesis Outline

In Chapter 1, the background and motivation behind the current work regarding the necessity of an EGR diluted combustion engine to achieve higher thermal efficiency incorporated with the hybrid powertrain for the current and future generation light-duty powertrain vehicle is discussed.

Chapter 2 describes the different stages of the Jetfire® ignition system and DM-TJI engine development. The effect of pre-chamber nozzle orifice diameter on engine speed performance at 40% EGR diluted conditions has been investigated experimentally on a single-cylinder DM-TJI engine at Michigan State University. The maximum engine efficiency was investigated on specific engine running points and compared with other similar engines' performance.

Chapter 3 studies the numerical simulation and model development of a DM-TJI engine. A 1D DM-TJI engine model with a 0D/1D combustion model approach was performed using GT-Power. Experiments were conducted to calibrate the developed model and verify the result. The calibrated engine system model was further studied to propose a predictive, generalized model for a DM-TJI engine. Engine efficiency and fuel map were generated using the generalized model for the DM-TJI engine covering a wide range of loads and speeds.

Chapter 4 demonstrates the powertrain architecture's selection, design, and optimization. Conventional, mild and parallel hybrid powertrain developed on GT-Suite powertrain model consists of three layers; systems, components, and functions. Equivalent circuit lithium-ion battery cell models have been studied for vehicle battery power management system development. Matlab/Simulink blocks are used to create an integrated model with easily changeable parameters for estimating the battery parameters. The battery pack model test data result is used for model validation. Rule-based controllers developed for hybrid powertrains include the engine controller, battery management system, transmission controller, and regenerative brake controller. The control system validates with a tested hybrid vehicle. The engine fuel map generated in Chapter 3 analyzed the three different powertrains developed for fuel consumption, CO2, and NOx emission over light-duty vehicle driving cycles.

Chapter 5 studies the DM-TJI metal engine fuel flexibility with E80 ethanol blend and methane alternative fuels. The EGR tolerance limit of the alternative fuels was evaluated. The fuel maximum thermal efficiency determined. The exhaust emission compared between the fuels.

Finally, the results and conclusions of the dissertation are summarized in chapter 6. This chapter also concludes with a list of remarks and recommended steps for future work.

Chapter 2: Development of a Pre-chamber Combustion for Spark Ignition Engines in Vehicle Applications

2.1 Introduction

The transport industry accounts for about 22% of the global primary energy consumed and is an important greenhouse gas emitter. With the current trend, it is estimated that in 2030 the transport sector will be responsible for 75% of GHG emissions [34,35]. Currently, the world has more than 1.2 billion passenger cars and 380 million commercial vehicles. Global industrialization and urbanization are likely to increase gasoline engine output in the future years. Hence creditable projections suggest 120 million new vehicle registrations by the year 2030. In addition to increasing electrification, at least 75% of vehicles are based on combustion engines [36]. The increasing strict emission regulations for internal combustion engines worldwide force car manufacturers to exploit innovative combustion technologies. Ambitious vehicle fleet CO2 emission reduction and fuel economy targets have been set for light-duty vehicles worldwide. Europe announced the most progressive emissions legislation so far, with an intended target of 95 g of CO2/km in 2021. A reduction of at least 37.5% must be achieved in 2030 in comparison to 2021 based on the Worldwide Harmonized Light vehicle Test Procedure [37,38].

In order to achieve these targets, the structure of the global automotive market is expected to change from pure thermal toward more advanced internal combustion engine-based powertrains with mild electrification. According to vehicle market studies, the cumulative share of gasoline hybrid powertrain vehicles will exceed 30% of worldwide sales in 2030 [38], a viable step toward electrification. A spark-ignition engine is a dominant choice for a hybrid powertrain due to its low cost and high-power density. It will also be essential to develop highly efficient internal engines to limit the constraints and requirements for the electrical components, such as the battery size. This is an essential step towards meeting environmental goals. These highly efficient internal combustion engines will also maximize vehicle efficiency in highway driving conditions where hybridization does not significantly benefit.

2.2 Pre-Chamber Ignition Concept

Several approaches are used to increase spark-ignition engine thermal efficiency, such as engine downsizing, high compression ratio, tumble enhancement, (late) intake valve closure, and charge dilution. Increasing the thermodynamic efficiency theoretically improves the overall energy efficiency. Based on the Otto cycle efficiency ($\eta_{th} = 1 - \frac{1}{CR^{\gamma-1}}$), the theoretical efficiency can be achieved by both increasing the compression ratio (CR) of the engine and by increasing the ratio of specific heats (γ) [37]. The compression ratio is mainly linked to the engine geometry and the specific heat ratio coefficient influenced by the air-fuel equivalent ratio of the combustion process. However, increasing both values shows major drawbacks in real engineering applications. Increasing the compression ratio has shown increases the in-cylinder temperature and pressure, leading to increased heat transfer losses and knock tendency. Burning high-diluted mixtures on a high engine compression ratio have shown the capability to improve engine efficiency in several ways. The heat losses through the combustion chamber walls are significantly reduced, and the pumping losses are reduced when the engine operates at medium-to-low loads. Conventional SI engines operating at partial loads use a throttle valve to restrict the intake flow, contributing significantly to the engine pumping work. High-diluted mixtures offer the potential to mitigate SI knock at high engine load [39–41].

Due to reduced laminar flame speeds and slower ignition kernel development, an extremely lean combustion mixture poses ignitability and stable combustion challenges. Thus, higher ignition energy is needed to ignite a leaner mixture, which may require non-conventional and costly technology. Many alternative ignition systems were examined to improve the dilution tolerance of the traditional SI engine. Some alternatives are plasma ignition, laser-induced ignition, high-energy spark plugs, corona discharge ignition, multi-strike ignition, and pre-chamber ignition systems [34,40]. However, high cost, unproven durability, and electrical interference remain challenging for many ignition technologies, except the pre-chamber ignition system. A compelling concept for burning diluted combustion can be a pre-chamber combustion system [26]. This technology effectively achieves lean combustion by improving engine dilution tolerance and knock performance. In such configurations, a mixture of fuel and air ignited in the pre-chamber, and the burning jets discharged into the main chamber. The pre-chamber inner volume is small compared to the main chamber clearance volume, usually occupying a volume that is roughly between 2% and 5% of the cylinder volume at the top dead center [41]. Both volumes exchange mass and energy through multiple nozzles. The turbulent jets from the pre-chamber create highly dispersed volumetric ignition and enhance turbulence, accelerating the combustion process within the main chamber [39,40].

The pre-chamber SI engine was first proposed by Ricardo in the 1920s and extensively developed in the Soviet Union and Japan [42]. The Ricardo 2-stroke engine incorporated two valves for intake/exhaust and a third auxiliary intake valve through which the rich fuel-air mixture was supplied to the pre-chamber. A separate intake manifold feeds a fuel-rich mixture through a small intake valve containing a spark plug into the pre-chamber connected to the main chamber through a nozzle. At the same time, a lean mixture is fed to the main chamber through the intake manifold.

A spark then ignites the rich mixture. After combustion starts in the pre-chamber, the rich burning mixture issues as a jet through one or more orifices into the main chamber, entraining and igniting the leaner main chamber mixture [43]. This 3-valve engine design inspired many other similar charge stratifications with pre-chamber concepts. A comprehensive review of the evolvement and progress of different pre-chamber initiated combustion systems was presented by Alvarez et al. [34] and Toulson et al. [43].

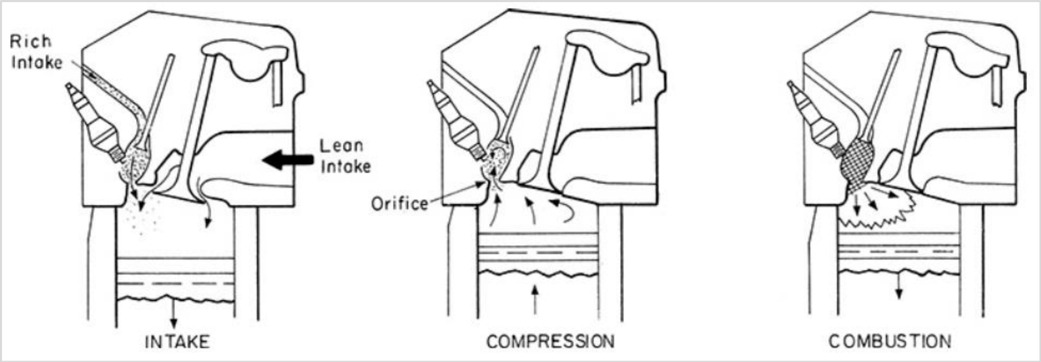

Figure 2.1 *Schematic of three-valve torch-ignition stratified-charge spark-ignition engine*[42]

2.2.1 Turbulent Jet Ignition (TJI)

The promising ignition enhancement technology for ultra-lean combustion with high-energy efficiency is turbulent jet ignition (TJI), a pre-chamber ignition enhancement concept for use in internal combustion engines that uses a distributed ignition source through the use of a chemically active turbulent jet [43]. The TJI system involves a small pre-chamber, a multi-orifice nozzle, and the main chamber. Nikolai Semenov first introduced the concept of jet ignition in late 1950, he directed with Lev Ivanovich Gussak, that the first jet ignition engine was developed [44]. TJI is a further refinement of the jet ignition concept for direct application to standard spark-ignition engines. The TJI system adopts a pre-chamber that houses a spark plug and optionally fuel/air injectors, which react as the ignition source by replacing the spark plug in a conventional spark-ignition engine. This technology is promising due to its fast burn rates and the ability to ignite mixtures with increased levels of dilution when compared to conventional spark ignition [22,24]. A rich fuel/air mixture is supplied to the pre-chamber to ensure successful ignition, and the main chamber can accommodate sufficient lean mixture for enhanced thermal efficiency.

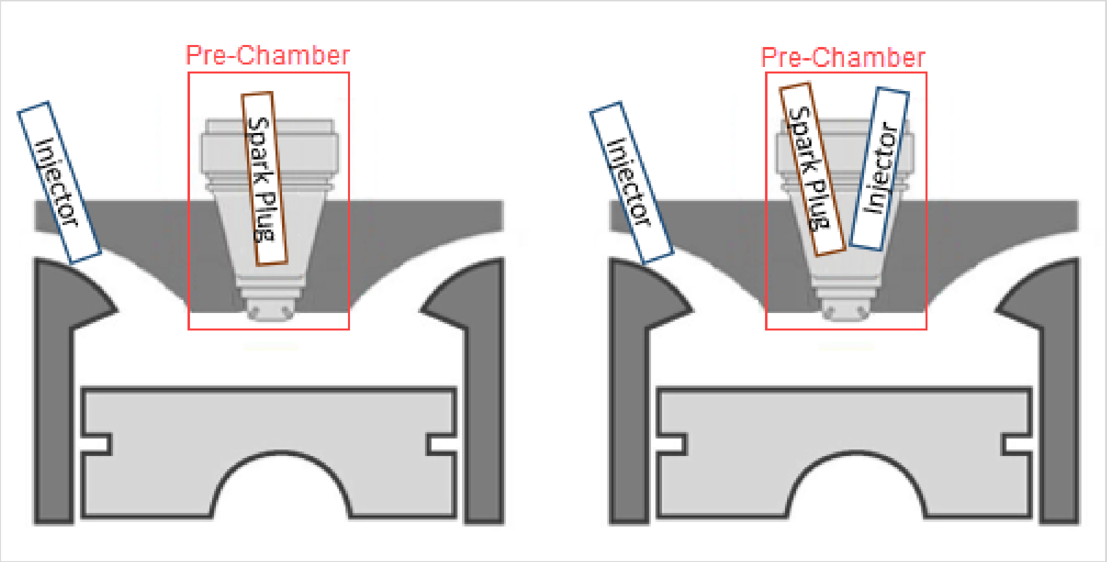

Figure 2.2 *Passive (left) and active (right) pre-chamber configurations*

There are two main configurations of TJI pre-chambers combustions known as ‘Passive’ and ‘Active’ pre-chambers, as shown in Figure 2.2 [45]. In the passive configuration, the pre-chamber contains only a spark plug, and there is no auxiliary fuel supplied into the pre-chamber. The fuel delivered in the main chamber is forced into the pre-chamber during the compression stroke. The air-to-fuel ratio is not directly controlled, so that the fuel/air mixture has to rely on natural scavenging during the intake stroke to enter the pre-chamber. Therefore, the passive pre-chamber design causes difficulty for precise charge preparation inside the pre-chamber, leading to more severe combustion instabilities and a higher chance of misfiring. The passive system cannot deliver the same maximum efficiency benefit as the active configuration when operating ultra-lean [45].

In the active configuration, an auxiliary fuel supplier inside the pre-chamber contains a second flow injector that can provide additional fueling to the pre-chamber. Its air-to-fuel ratio is controlled at optimum values close to rich conditions from the main chamber [41].

Two different strategies can be used to achieve a dilution mixture in the combustion chamber: excess air dilution, referred to as the lean-burn strategy, and EGR. Both approaches offer similar benefits in achieving low-temperature combustion to realize better thermal efficiency benefits and emission improvements. In terms of improving fuel economy, the lean-burn system is generally more effective than the EGR system because the specific heat ratio of excess air is higher than that of recirculated exhaust gas. However, lean-burn operation with excess air dilution in SI engines has difficulty meeting the legal NOx emission requirement. A significant challenge with the lean burn strategy is that it cannot utilize highly effective efficiency of the widely used three-way catalyst (TWC).

On the other hand, an EGR system with a three-way catalyst is more effective in reducing NOx emissions. If a large quantity of recirculated exhaust gas can be introduced under stoichiometric operating conditions, NOx emissions can be reduced by the three-way catalyst, and fuel economy can be improved to almost the same level achieved by conventional lean-burn technology. In gasoline-fueled SI engines, the TWC has proved to be very efficient at reducing the engine out of HC, CO, and NOx emissions. The limitation is that the engine needs to operate very close to stoichiometric conditions to make the catalytic conversion efficient. The catalytic converter efficiency is low if the air/fuel ratio moves slightly toward the lean limit [46]. The basic demands of higher technologies in SI engines come from high brake thermal efficiency and low engine-out emissions while maintaining low investment and maintenance costs. Lean combustion in modern SI engines has been shown to provide improved thermal efficiency; it also produces higher NOx emission compared to operation at high EGR dilution while maintaining overall stoichiometric conditions. This makes using a TWC nearly impossible and necessitates additional after-treatment systems such as a lean NOx trap or selective catalytic reduction catalysts. An alternative strategy can be EGR [25] to overcome this problem. If the inlet charge is diluted by EGR or high levels of cylinder trapped residual, similar advantages to the excess air dilution operation can be attained while maintaining the stoichiometric air-fuel ratio that permits the effective usage of TWC.

2.2.2 Dual-Mode Turbulent Jet Ignition

Using EGR as the diluent instead of excess air makes using a TWC possible, but it requires the engine to operate with a very high level of EGR to reach the efficiency of very lean systems. However, high EGR decreases the laminar flame speed compared to the lean operating conditions because of the lower oxygen concentration in the mixture [47]. With excess air dilution, there is a high percentage of excess air available in the pre-chamber so that a small additional amount of fuel injection still enables the formation of an ignitable mixture in the pre-chamber. However, TJI systems cannot operate effectively under dilute conditions with very high levels of EGR due to their difficulty in reliably igniting the pre-chamber. With a high level of EGR mixed with the intake air-fuel reactants along with the trapped residuals, it becomes challenging to control the pre-chamber mixture at stoichiometry using only the auxiliary pre-chamber fuel injection [25]. This leads to pre-chamber misfires, which propagate to misfires in the main chamber, and the combustion stability suffers. To overcome this problem, a DM-TJI system was introduced [48].

The DM-TJI system is an engine combustion technology in which the pre-chamber is equipped with an auxiliary air supply along with the auxiliary fuel injector [25,49–51]. The DM-TJI system is the modified version of the TJI system with the additional air supply and the method of delivery to the pre-chamber [38,49,52]. The DM-TJI system enhances the pre-chamber stoichiometry control, independently of the main chamber, for better combustion stability in the pre-chamber and main chamber. Spark ignition in the pre-chamber creates highly energetic chemically active turbulent jets that pass through a multi orifice nozzle to enter the main chamber and initiate combustion at multiple sites distributed around the highly dilute mixture inside the main chamber. This is particularly important to achieve the fast burn rates due to the low flame velocities inherent in a highly dilute the air-fuel mixture. The additional air supply to the pre-chamber through auxiliary air supply gives three advantages on the highly EGR diluted combustion. First, it helps purge the pre-chamber effectively from combustion residuals. Second, it maintains the pre-chamber mixture at an ignitable state when the main chamber is mixed with high EGR dilution. Third, the system can use the conventional TWC by permitting stoichiometric operation with a high level of EGR dilution.

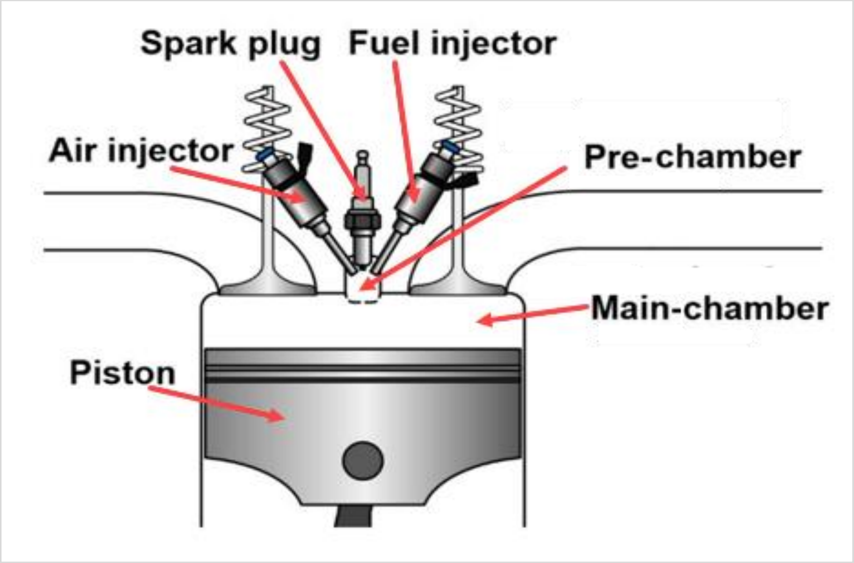

***Figure 2.3** DM-TJI engine architecture* [53]

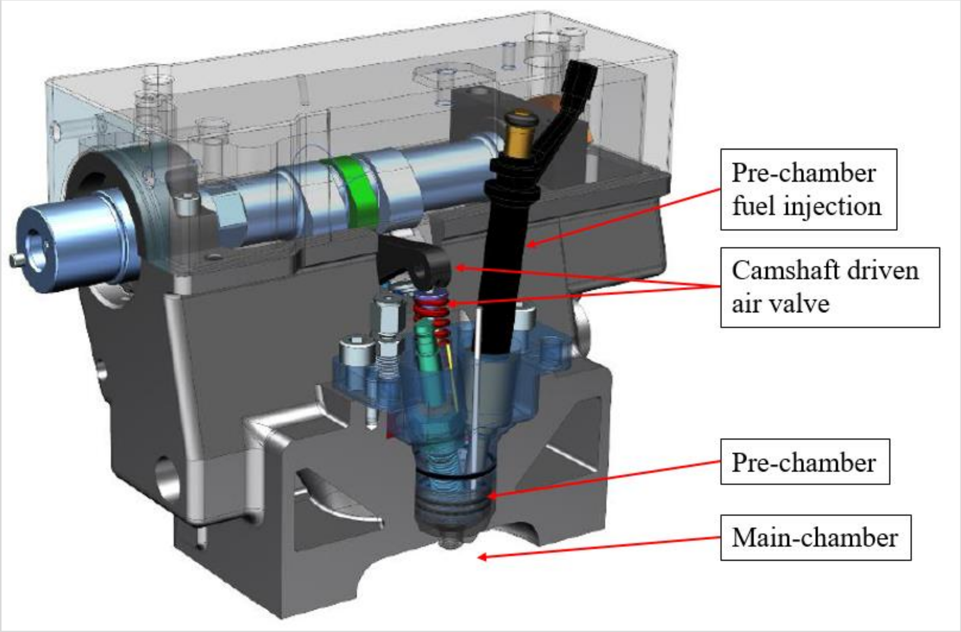

Figure 2.4 *Sectional view of DM-TJI system engine head with the pre-chamber system (CAD model rendering)*

There have been several studies on the DM-TJI engine. Vedula et al. [30] studied the effect of pre-chamber fuel injection timing, including pre-chamber air injection and different injection pressures on iso-octane/air combustion in a DM-TJI system equipped rapid compression machine for a global lambda of 3.0. Song et al. [53] studied a control-oriented combustion model for a single-cylinder prototype I DM-TJI engine with speeds between 1200 and 2000 rpm with IMEP between 4.2 and 7.2 bar using liquid fuel for both pre and main combustion chambers. Vedula et al. [51] reported a net thermal efficiency of 45.5%±0.5% for the prototype I DM-TJI engine at Michigan State University (MSU) with a compression ratio of 12.0 and wide-open throttle using both lean air-fuel mixture and 30% nitrogen-diluted near-stoichiometric mixture. Tolou et al. [50] predicted the ancillary work required to operate a prototype II DM-TJI system and developed a GT-Power model that employed a two-zone analysis for pre and main combustion chambers. Atis et al. [25] studied Prototype II DM-TJI optical engine at MSU and showed that the system could maintain stable operation ($COV_{IMEP}<2\%$) with 40% external EGR at stoichiometric ($\lambda\sim1$) operating conditions. The study also demonstrated while a correlation between the nozzle orifice diameters and overall burn duration. Atis et al. [49] studied a comparative experimental study of lean burn and EGR diluted operation in a pre-chamber air-fuel scavenged Prototype III DM-TJI system in a high compression ratio, single-cylinder fueled with gasoline. The study shows EGR dilution was more effective in NOx emission reduction than excess air dilution. A maximum of 38.5% net indicated thermal efficiency with a 40% EGR dilution rate running at a load of 6 bar IMEPg at 1500 rpm.

2.3 Pre-Chamber Nozzle Orifice Diameter

Most TJI systems consist of a pre-chamber and main chamber connected with one or more small orifices. Combustion initiated in the pre-chamber using conventional SI causes a high-pressure increase. It forces the hot products of combustion to discharge through one or more small orifices into the main chamber. Compared to the more traditional pre-chamber used in diesel engines with large volume, single orifice diameters, a smaller pre-chamber with multiple orifice nozzles and smaller orifice diameters can improve the lean limit of an SI engine [40]. The multiple orifice nozzle produces multiple distributed ignition sites throughout the main chamber. With rapid burning, there is less residence time available for end-gas to reach knocking conditions. This enables the use of a higher compression ratio, further increasing thermal efficiency. The orifice diameter and number are critical to any TJI system, and their influence on the transient jet development is worthy of further study.

Previous studies have investigated TJI and the influence of nozzle geometry by employing various means of experimental testing, numerical modeling, and image visualization and processing.

However, there is no comprehensive overview in the literature of how the nozzle geometry affects the TJI process. Bunce et al. [54] studied five different pre-chamber nozzle designs and diameter range between 0.64 and 1.36mm on a light-duty gasoline engine. Both large and small nozzle diameters will cause non-ideal engine combustion and resulting efficiency. Roethlisberger et al. [55] tested a TJI igniter in a diesel engine with four different orifice diameters ranging from 1.41 to 2.24mm and found that a small total nozzle cross-sectional area was advantageous for jet penetration and combustion initiation. However, there was a limit to how small the orifice could be reduced before the occurrence of ignition misfire. Gentz et al. [26] identified slight variations of burn duration between the different diameters, at which point the burn duration increases as the diameter increases. Thelen et al. [56] studied fully three-dimensional CFD simulations with four different orifice diameters; an orifice diameter of 1.5 mm provides the fastest ignition and the fastest overall combustion burn duration. Gentz et al. [57] show that a 1.5 mm orifice exhibited the fastest flame initiation compared with 2 and 3mm single-orifice nozzles with a premixed propane/air mixture studied by visualizing the combustion in an optically accessible rapid compression machine (RCM). Atis et al. [25] studied a range of pre-chamber nozzle orifice diameters with lean and EGR diluted conditions. In general, smaller orifice diameters resulted in shorter overall burn duration due to more favorable distribution in ignition sites. Yu et al. [40] investigated several passive pre-chamber design to examine the engine performance tradeoffs with nozzle diameter, pre-chamber volume, number of nozzles, and pre-chamber fuel enrichment for excess air and external air EGR dilution strategies. Increasing the number of nozzles at a fixed nozzle area-to-volume ratio can improve efficiency tradeoff while maintaining a shorter burn rate due to longer flame jet penetration and higher turbulence.

Most pre-chamber orifice diameter studies are conducted on RCM or on a single-cylinder engine test with a specific fixed engine speed. This chapter focuses on results of engine speed variation on pre-chamber nozzle orifice diameter. Three different orifice diameters (1.25, 1.5, and 1.75mm) are selected based on the preliminary study result of the Prototype II DM-TJI optical engine. The engine speed varies in a range of 1500–2300 rpm. The engine speed range is limited by the test setup.

2.4 Experimental Setup and Arrangement

2.4.1 Engine Setup

The engine used in this study is a single-cylinder Prototype III DM-TJI metal engine. The engine's stroke was 95 mm, and the bore was 86 mm with a connecting rod length of 170 mm. Table 2.1 shows the dimensions and other detailed experimental engine specifications—an intake manifold with pockets for port fuel injectors designed and installed for injection of main-chamber fuel. The test bench incorporated a boost-cart assembly. The first stage EATON TVS R410 supercharger was used alone for lower load along with a charge air cooler (CAC). The second stage supercharger (EATON TVS R900) was added for the higher load to ensure that enough boost and EGR rate could be maintained. Upstream throttle, a blow-off valve, and an EGR valve are used to control intake conditions for boosted operation. The EGR line is connected from the exhaust system to the boost-cart using the EGR valve. A large intake plenum was utilized to ensure proper mixing of EGR before entering the combustion chamber. The intake air-EGR mixture temperature was maintained at 45°C for all the tests.

The recirculating exhaust gas cools down before it reaches the EGR valve assembly using the EGR cooler. The CAC controls the EGR temperatures to a specific level to avoid condensation due to the high EGR rate and maintain a constant intake charge temperature throughout the tests. A pressure delta across the EGR system was maintained using the upstream throttle and the EGR valve. A cooling system had a separate controller and coolant pump to circulate a 50:50 ethylene glycol-water mixture through the engine to maintain the cylinder head temperature at 90°C using an electrically powered heating element.

Table 2.1 *Engine specification used for orifice comparison*

Parameter	**Description**
Bore	86 mm
Stroke	95 mm
Connecting rod length	170 mm
Main chamber swept volume	0.55 L
Compression ratio	13.3:1
Number of Cylinders	1
Strokes	4
Fuel injection pressure	100 bar
Injection system	Direct in pre-chamber and port in the main chamber
Pre-chamber volume	2900 mm^3 (~6 % of clearance volume)
Number of Nozzle orifice and configuration	6 holes, Symmetric
Orifice diameter	1.25mm, 1.5mm and 1.75mm
Number of Valves	2-intake, 2-exhaust, 1-pre-chamber
Pre-chamber air supply pressure	30-75 psi (gauge)
Valve timing for max lift	Intake timing - 90 CAD aTDCGE, Air valve timing - 110 CAD bTDCF Exhaust timing - 90 CAD bTDCGE
Intake system	Naturally aspirated and boosted

Using a PID (proportional-integral-differential) controller, the temperature was maintained at this set temperature during the entire testing time. When the engine coolant exit temperature is above 90°C, the chiller valve opens, and the coolant circulates through the heat exchanger until the temperature is back to 90°C. The compressed air was introduced into the pre-chamber from the shop's compressed air supply line through the air valve actuated by the intake camshaft containing a separate air-valve cam lobe. The compressed air pressure was regulated via a pressure regulator. A DC dynamometer was used to control the engine speed. Figure 2.5 and Figure 2.6 shows a schematic diagram of the engine assembly experimental set-up with a fully instrumented test cell.

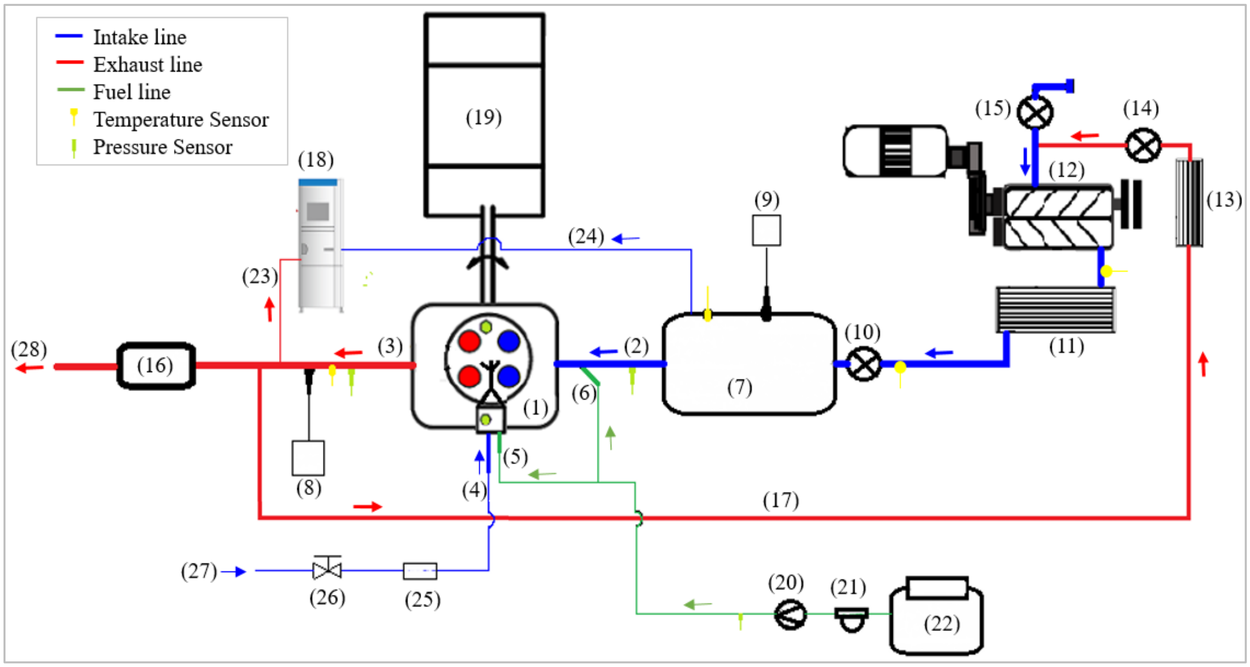

Figure 2.5 *Schematic diagram of the experimental set-up*

(1) Engine head with pre-chamber, (2) Intake runner (3) Exhaust runner (4) Pre-chamber air valve (5) Pre-chamber fuel injector (6) Main chamber injector (7) Intake plenum (8) Lambda sensor (9) Intake O_2 *sensor (10) Intake throttle (11) CAS (12) Supercharger (13) EGR cooler (14) EGR valve (15) Upstream throttle (16) Muffler (17) EGR line (18) HORIBA exhaust analyzer (19) Dynamometer (20) Fuel pump (21) Fuel flow meter (22) Fuel thank (23) Exhaust emission line (24) Intake* CO_2 *line (25) LFE (26) Pre-chamber pressure regulator (27) Shop compressed air supply (28) Vent*

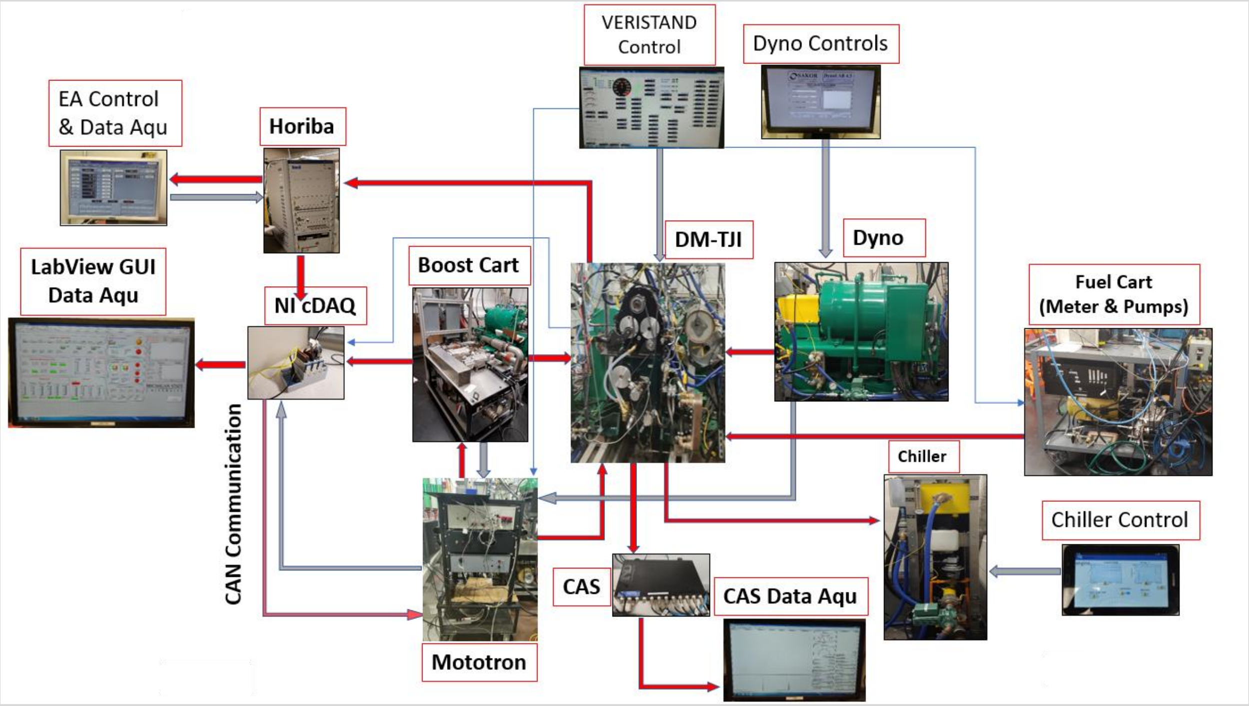

Figure 2.6 *Engine test rig*

2.4.2 Pre-Chamber Ignition System

The pre-chamber ignition system used in this study is a redesigned prototype III Jetfire® cartridge. The first two prototypes were optical engines; the first prototype [51] had an air injector inside the pre-chamber to deliver auxiliary air, whereas the second prototype [25] replaced the pre-chamber air injector with a hydraulically controlled poppet valve for pre-chamber air delivery. The current Prototype III DM-TJI engine [49] replaces the hydraulically controlled pre-chamber air valve with a more compact Jetfire® cartridge design which contains a more production viable intake camshaft-driven air valve. The engine head has a pent roof head modified to incorporate the pre-chamber Jetfire® cartridge and air-valve driving assembly, as shown in Figure 2.7. The pre-chamber Jetfire® cartridge design packages contain the conventional spark plug, fuel injector, and auxiliary air valve.

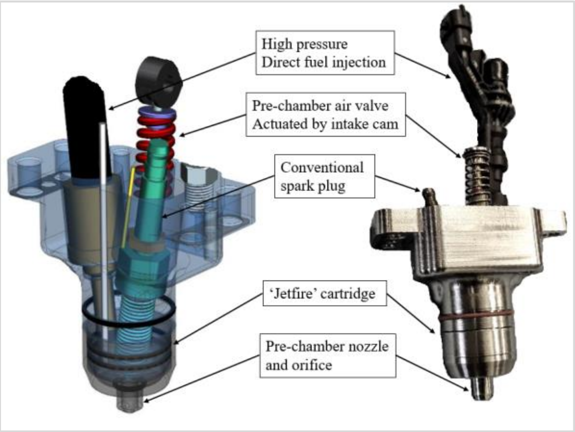

Figure 2.7 *Pre-chamber Jetfire cartridge package CAD design and actual picture*

2.4.3 Engine Instrumentation

The engine was tested in a fully instrumented engine test cell with all the standard temperature, pressure, humidity, and engine-specific measurements, including air and fuel flow, dynamometer, and emission instruments, as shown in Figure 2.5 and Figure 2.6. A measuring spark plug with an integrated pressure transducer, Kistler 6115CF-8CQ01-4-1, was employed for the pre-chamber pressure measurement. Pre-chamber combustion was initiated by this 'hot' spark plug and a conventional automotive inductive ignition system with 60mJ of ignition energy. The main chamber pressure was measured separately using a second pressure sensor, Kistler 6052A, installed in the engine head. Piezoresistive pressure transducers Kistler 4045A and Kulite EWCTV-312 were installed on the intake and exhaust runner to measure the port pressures.

Two data acquisition systems were used. The first was an A&D Technology Combustion Analysis System (CAS) for high-speed, crank angle resolved pressure data. Sampling resolution of the pre- and main chamber pressure was set to 0.1 crank angle degree (CAD) and for the port pressure at 0.5 CAD. The second was a National Instruments (NI) data acquisition device for low-frequency data. Time-averaged data of temperatures, pressures, fuel flow rates, and emissions were measured.

Type K thermocouples were added to the intake manifold, exhaust manifold, selected coolant lines, and the oil gallery to measure and monitor the temperatures. A Meriam laminar flow element (LFE), Z50MJ10-11, was installed to measure the pre-chamber airflow, which was installed in the pressurized air-line upstream of a compressed air plenum. The plenum is used to minimize pressure fluctuation. A multivariable digital transmitter, MDT500 by Meriam Process Technologies, was used to transfer the LFE reading to the Meriam software development kit (SDK). Ambient pressure, temperature, and relative humidity were measured using Omega sensors (Omega PX409 and Omega HX93BC-RP1).

The lambda was measured by the emission bench and lambda sensor (ECM Lambda-5200) that are installed in the exhaust system. Exhaust emissions were measured using a Horiba MEXA-7100 DEGR automotive emission bench that contains CO2, CO, THC, O2, and NOx analyzers. The analyzer also measures the EGR rate by a dedicated separate intake CO2 sampling line connected to the intake manifold to measure the volumetric EGR rate. The volumetric EGR rate was cross-checked with pressure compensated O_2 sensors (ECM Lambda-5200) installed in the intake manifold. An in-house control system containing NI-PXI chassis and Mototron ECM-5554 controllers managed within an NI Veristand environment was used to control the main engine control parameters such as spark timing, pre- and main chamber fuel injection timings and durations, intake runner throttle, and EGR valve positions. The most relevant global parameters related to the combustion process, such as the indicated gross mean effective pressure (IMEPg), start of combustion (SoC), combustion phasing (CA50), combustion duration (CA10-90), maximum cylinder pressure, pressure gradient, combustion stability, heat release rate (HRR) and cylinder mean gas temperature were calculated from the cylinder pressure signal.

2.4.4 Engine Fueling System

A fuel cart contains a fuel tank, Coriolis fuel flow meter, and a high-pressure fuel pump used to deliver high-pressure DI injectors. The fuel supply line divided into two lines, each of which provided fuel to a separate chamber, which fueled both the pre- and the main chambers. Pre-chamber fuel was supplied with a custom-developed two holes low-flow DI injector, whereas the main chamber fuel was supplied in PFI configuration but with a higher flow rate six holes DI injector. A LabView program and a NI system are used to control fuel line pressure. Both the pre-chamber and main chamber fuel injection pressures were set at 100 bar. The main chamber fuel was injected at 360 CAD bTDCF using three split injection pulses, and the pre-chamber fuel was injected at 70 CAD bTDCF using a two split injection strategy. All tests were performed with Tier III regular certification gasoline fuel. The combined pre- and main chamber fuel flow rate was measured using a Micro Motion CMFS007M Coriolis flow meter.

2.5 Engine Operating Conditions

Two experiment tests were conducted in the test setup: the first condition is comparing three different nozzle orifice diameters with the same engine running conditions only by changing the orifice diameter. The second condition is determining the maximum engine efficiency points by varying the engine running conditions for each orifice diameter.

2.5.1 Nozzle Orifice Diameter Analysis

Experiments were conducted with three different pre-chamber nozzle orifice sizes, while the layout of the orifices was kept the same. The pre-chamber nozzle orifice diameters used for the three configurations were 1.25mm, 1.5mm, and 1.75mm. The intake and exhaust valve open for maximum lift at 90 CAD aTDCGE and 90 CAD bTDCGE, respectively. Main chamber fuel was injected at 360 CAD bTDCF using three split injection pulses, and pre-chamber fuel was injected at 70 CAD bTDCF using two split injections. The pre-chamber purge air upstream pressure was set at 75 psi (gauge) for orifice comparison, and the air valve time was open at 110 CAD bTDCF for maximum lift. The engine was tested at a nominal IMEPg of 10 bar with 40% EGR dilution with a speed range of 1500 to 2300 rpm. The engine compression ratio was 13.3:1, and the spark timing was fixed between 30-20 CAD bTDCF depending on the engine speed. During the test for all orifice diameters, the spark timing, the amount of main chamber fuel, the amount of pre-chamber fuel, and the respective injection timings were kept the same. The influence of nozzle orifice diameter was studied to determine how the orifice diameter affected engine operation concerning running stability and major combustion parameters across engine speed variation.

2.5.2 Determine Maximum Engine Efficiency

The engine operating conditions to determine maximum efficiency were similar to the previous (nozzle office analysis) setup. Main chamber fuel was injected at 360 CAD bTDCF using three split injection pulses and pre-chamber fuel was injected at 70 CAD bTDCF using two split injections. The intake and exhaust valve opened for maximum lift at 90 CAD aTDCGE and 90 CAD bTDCGE, respectively. The auxiliary air valve was open at 110 CAD bTDCF for maximum lift. The pre-chamber purge air upstream pressure was set between 30-70 psi (gauge) depending on the load and engine speed—the engine runs from 2.5 to 10bar IMEPg with a speed range of 1500 to 2300 rpm. The intake air was diluted with EGR up to the tolerance limit of the combustion stability allowed. The maximum EGR tolerance limit for each configuration was identified based on two criteria combustion stability limits set as 3% $\mathrm{COV_{IMEP}}$ and a knock limit set as more than 10% cycle crossing a 1.0 bar Pressure Oscillation Difference (POD).

2.5.3 Definitions and Terminology

Some important parameters used in the methodology are defined in this section:

- Air-fuel equivalence ratio lambda (λ) is defined as the actual air-fuel ratio to the stoichiometric air-fuel ratio of both chambers

$$\lambda = \frac{(A/F)_{actual}}{(A/F)_{Stoic.}} \qquad 2.1$$

Where $(A/F)_{actual}$ and $(AFR)_{stoic.}$ are the mass based actual and stoichiometric air fuel ratio, respectively[42].

- Gross indicated mean effective pressure is given by

$$IMEP_g = \int_{-180^o}^{180^o} \frac{(P.dv)_{main\ chamber}}{V_d} \qquad 2.2$$

Where, P, v, and V_d are the cylinder pressure, cylinder volume, and displacement volume, respectively [39].

- Coefficient of variation of $IMEP_g$ is given by

$$COV_{IMEPg} = \frac{\sigma_{IMEPg}}{\overline{(IMEPg)}} = \frac{\sqrt{\frac{\sum_{k=1}^{N}(IMEP_{g,k} - \overline{(IMEPg)})^2}{N}}}{\overline{(IMEPg)}} \qquad 2.3$$

Where, N is the number of cycles [39].

- EGR percentage *(v/v)* is determined in volume basis using the following equation

$$EGR_{volume} = \frac{(CO_2)_{intake}}{(CO_2)_{exhaust}} \qquad 2.4$$

Where $(CO_2)_{intake}$ and $(CO_2)_{exhaust}$ are concentrations of CO_2 sampled from engine intake, which is a mixture of fresh air and EGR and exhaust gas, respectively[58]. These values were measured using a Horiba MEXA-7100 DEGR automotive emission bench.

- The volumetric EGR rate was cross-verified with the intake O_2 percentage measured by the pressure compensated wideband. The EGR rate is mathematically represented as:

$$EGR_{volume} = \frac{(O_2)_{ambient} - (O_2)_{intakeair}}{(O_2)_{ambient} - (O_2)_{exhaust}} \qquad 2.5$$

Where $(O_2)_{ambient}$ = oxygen concentration in ambient air, $(O_2)_{intakeair}$ = oxygen concentration of EGR + air mixture and $(O_2)_{exhaust}$ = oxygen concentration of exhaust[59].

- The indicated efficiency was estimated using the following equation

$$Indicated\ Efficency = \frac{IMEPg * Swept\ Volume}{m_{fuel} *\ LHV} \qquad 2.6$$

Where, LHV is the lower heating value of the fuel, m_{fuel} is the mass flowrate of the fuel, *IMEPg* indicated mean effective pressure.

- The flame development angle is defined as the difference between crank angle degree (CAD) of spark timing and CAD of 10% of accumulated heat release.
- The combustion phasing (CA50) is defined as CAD of 50% of accumulated heat release.
- Combustion/Burn duration is defined as the difference between CAD of 10% and 90% of accumulated heat release.

2.6 Results and Discussion

2.6.1 Nozzle Orifice Diameter Analysis

The engine operates at a nominal IMEPg of 10 ± 0.5 bar with 40 ± 1% EGR dilution and lambda 1 for the orifice diameter comparison. The engine speed varied from 1500 rpm to 2300 rpm. The data analysis was carried out for 200 engine cycles for each test point. Figure 2.8 shows the result of the average values of the combustion parameters for the main chamber.

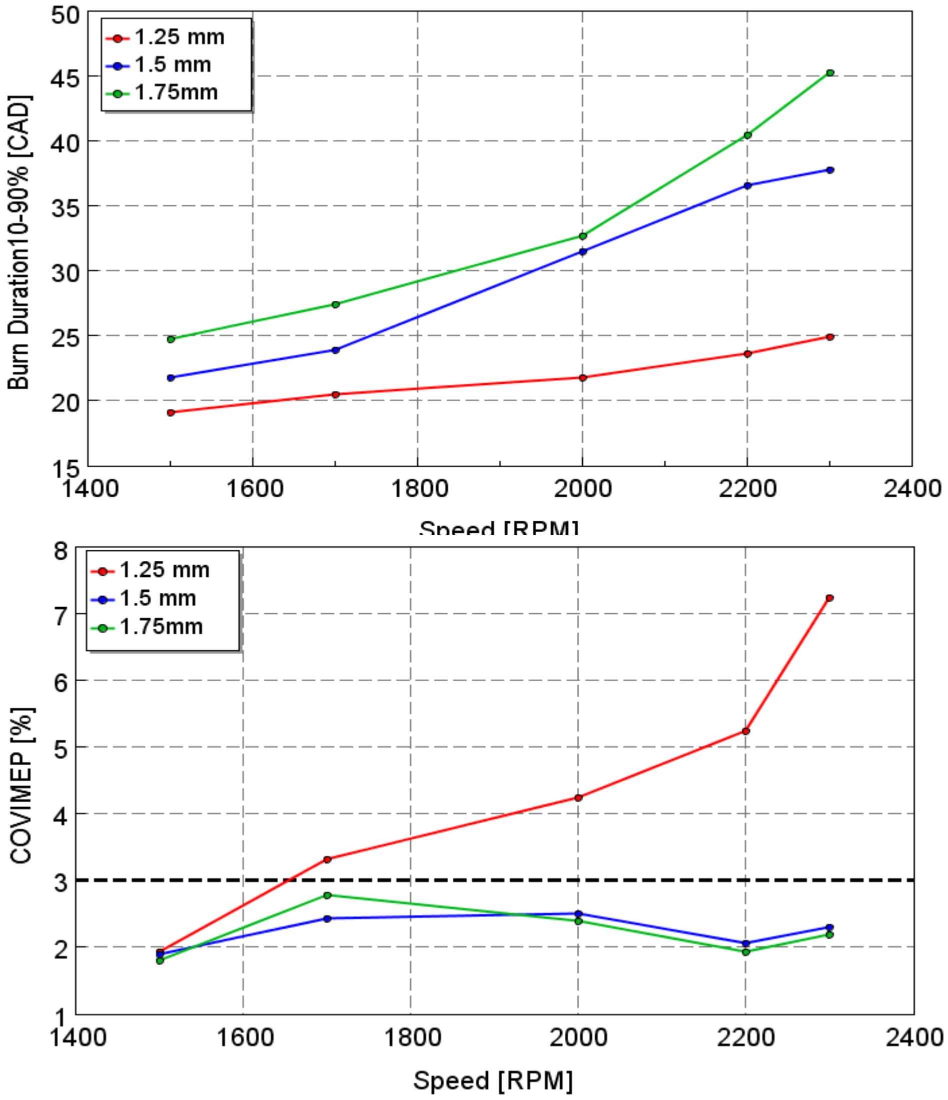

Figure 2.8 *Average combustion parameters of the main chamber 200 cycles of the three orifices diameter, average combustion stability COV_{IEMP} (Bottom), and burn duration Burn1090 (Tope)*

Considering the burning rate of each orifice diameter, as expected and reported in the previous study [25], orifice diameter of 1.25mm provides a short burn duration (fast combustion) compared to orifice diameters 1.5mm and 1.75mm. The fast combustion rate might be caused by longer flame penetration from the small orifice diameter. However, when the engine speed increases, the combustion stability of the 1.25mm orifice diameter starts to suffer, as shown in Figure 2.8. When the engine runs at 1500 rpm, the COV_{IMEP} of orifice diameter 1.25mm is below 2%. When the engine speed increases above 1700rpm, the COV_{IMEP} of orifice diameter 1.25mm increases above

3% (COV_{IMEP} limit). On the other hand, the COV_{IMEP} of orifice diameter 1.5mm and 1.75mm is below 3% through all speed variation. However, it exhibited the slowest combustion rate, which could be attributed to the unfavorable distribution of ignition sites due to decreased jet penetration. All orifice diameters have advantages and disadvantages, but it is challenging to consider the advantages of the 1.25mm orifice diameter fast burn rate and jet penetration without stable combustion.

An experimental engine motoring pressure trace was analyzed on the three orifice diameters to determine the cause of combustion instability at high engine speed for orifice diameter 1.25mm. The peak motoring pressure trace of the pre and main chamber are shown in Figure 2.9 for 1500, 2000, and 2500 rpm engine speeds. At 1500 rpm, the pre-chamber peak pressure was at TDC (CAD 0); when the engine speed increases to 2500 rpm, the flow exchange time between the two chambers gets lower, and the pre-chamber peak pressure moves to the right direction from TDC by 1.2CAD, but the main chamber peak pressure is at TDC for all three engine speeds. This implies that flow resistance through the small orifice diameter increased with engine speed, and the flow exchange between the two chambers lagged by 1.2CAD. However, the engine speed variation for orifice diameters 1.5 and 1.75mm did not cause significant peak pressure position change on the pre-chamber pressure trace.

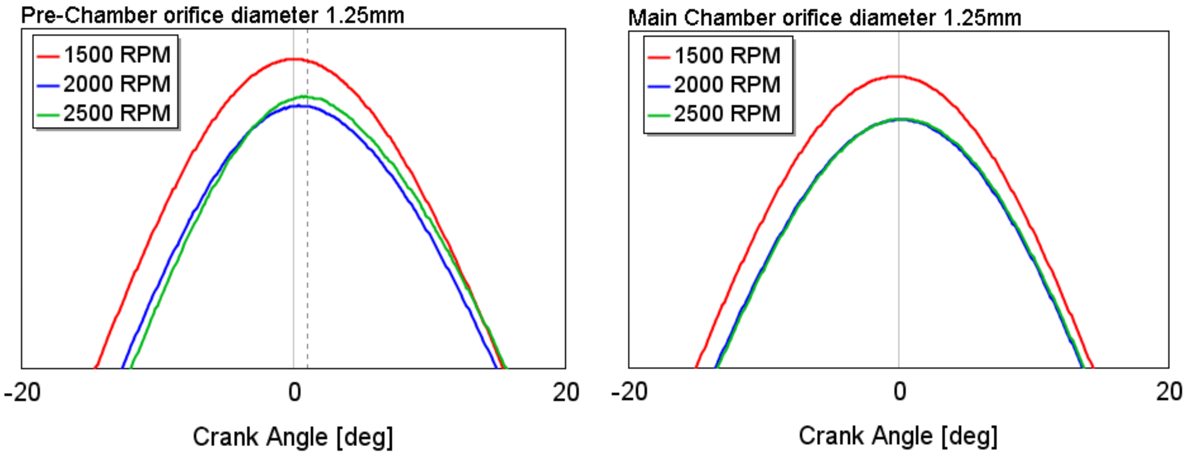

Figure 2.9 *Pre- and main chamber motoring pressure trace for orifice diameter 1.25mm*

2.6.2 1-D simulation: Engine pressure trace analysis

A numerical analysis was conducted to investigate the nozzle orifice diameter effect on the engine speed beyond 2500 rpm. The pressure traces and temperature data obtained during the experimental test were used for the three pressure analysis (TPA), which was carried out using GT- Power [60] software. Three different pressure measurements are required from the experimental test to calibrate the model. Two of these measurements are intake and exhaust port pressures, and the third measurement is cylinder pressure. High-speed intake and exhaust port pressure trace were imposed as boundary conditions on the TPA model; this reduced the number of offsetting boundary conditions that could be applied to match the experimental conditions. The pre and main chamber engine motoring data were used instead of the complicated combustion modeling. The measured and predicted pressure traces (red and blue, respectively) are shown in Figure 2.10. The model predicted result is very close to the measured motoring pressure trace with a maximum difference of 2 bar.

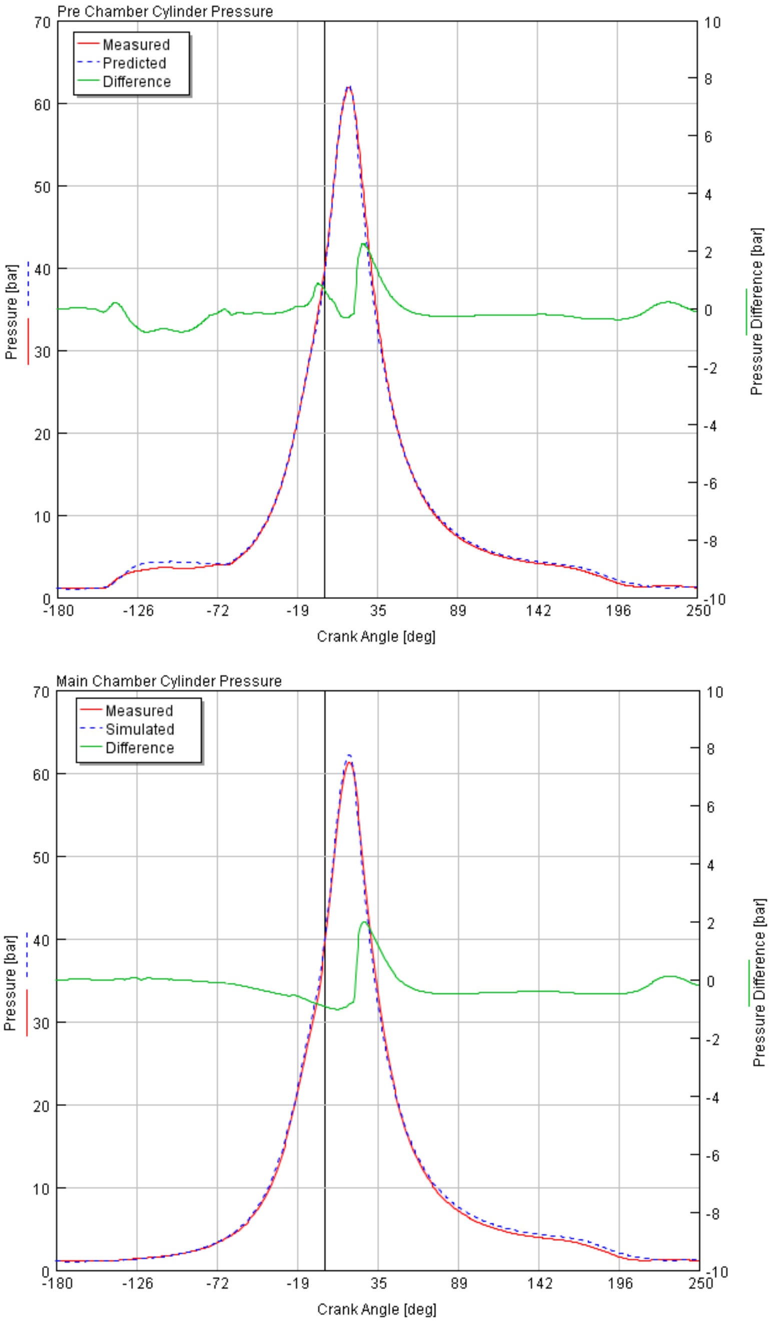

Figure 2.10 *Measured and predicted engine firing pressures trace at CR = 13.3:1*

The calibrated GT-power model fuel injection set zero to generate the engine motoring trace. A case setup is prepared to simulate a range of operating speeds from 1000 to 4000 rpm in increments of 1000 rpm. Figure 2.11 shows the pre-chamber motoring pressure trace for 1.25mm, 1.5mm, and

1.75mm orifice diameter at 1000 and 4000 rpm engine speeds. The model simulation shows that 1.25mm orifice diameter affected by airflow resistance between the two chambers at the highest engine speed. The peak pressure of 1.25mm orifice diameter further shifted for the engine speed of 4000 rpm by 7CAD from the TDC as shown in Figure 2.11 dotted vertical line. The lagging pressure trace indicates that the airflow resistance on the orifice increased for high engine speed, and the flow exchange between the two chambers lagged by 7CAD. There might not be enough time to purge the pre-chamber from the combustion residual and leading to engine misfire. The peak pressure change is negligible for the 1.5mm (0.2CAD) and 1.75mm (0CAD) orifice diameters at high engine speed. Based on the experimental and simulation results, 1.5 and 1.75mm orifice diameters are better candidates for a DM-TJI engine with a wide engine speed range.

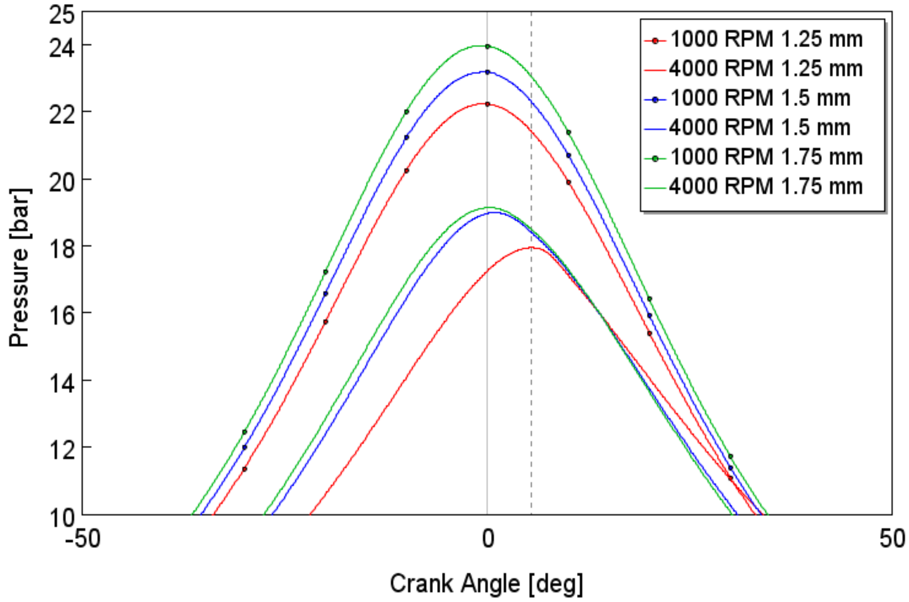

Figure 2.11 *Pre-Chamber motoring pressure trace for 1.25, 1.5 and 1.75mm orifice diameter at 1000 and 4000rpm engine speed.*

An additional advantage observed using 1.5 and 1.75mm orifice diameters. The engine can run with low pre-chamber upper stream pressure for low engine speed compared to the 1.25mm orifice diameter. For example, an engine running points which operates at a load of 8 bar at engine speed

1500 rpm (1.25mm orifice diameter, 75 psi upper stream pressure) can run with the same engine load and speed with 1.5 and 1.75mm orifice diameter using 55 psi upper stream pressure. This will reduce the work input to the auxiliary pre- chamber air supply and increase engine efficiency.

2.6.3 DM-TJI Engine Thermal Efficiency

The maximum efficiency of the single-cylinder DM-TJI engine was evaluated using 200 consecutive cycles collected for each selected operating point of orifice diameters 1.5 mm and 1.75mm. The considered operating points showed good stability with low COV_{IMEP} (less than 3%), high EGR dilution (45%), and below the assigned knock limit. The timings for main chamber injection were held constant throughout this study, and the start of injection signal of the main injector was fixed to 360 CAD bTDCF. The injection event takes place during the intake stroke, which ensures enough time for the mixture preparation. In pre-chamber, the start of injection timing was 65 CAD bTDCF. This timing has been identified as an adequate compromise between sufficient time for mixture formation inside the pre-chamber and sufficient cylinder backpressure to prevent fuel escaping from the pre-chamber before ignition timing. A preliminary spark advance sweep has shown that the commonly used combustion phasing of CA50 at 6-9 CAD aTDCF is the optimum engine efficiency for the EGR diluted operating conditions. If there were no knocking limitation on the spark advance set, the ignition time retarded to ensure maximum engine efficiency. The impact of the spark timing was analyzed by advancing or delaying it with 2 CAD steps from the maximum brake torque (MBT) point. The tests were carried out in a various driving cycles engine operating range, at engine speed between 1500 - 2300 rpm and a range of indicated mean effective pressure (IMEPg) between 2.5 - 10 bar. This speed and loads represent the majority of operating condition over driving cycles. The EGR dilution rate and the pre-chamber upstream pressure value vary based on the engine speed and load. Figure 2.12 presents the maximum DM-

TJI engine indicated thermal efficiency, number of knock cycles above 1 bar, and coefficient of variation of IMEPg obtained using orifice diameters 1.25mm, 1.5mm, and 1.75mm between the engine speed 1500 – 2300 rpm.

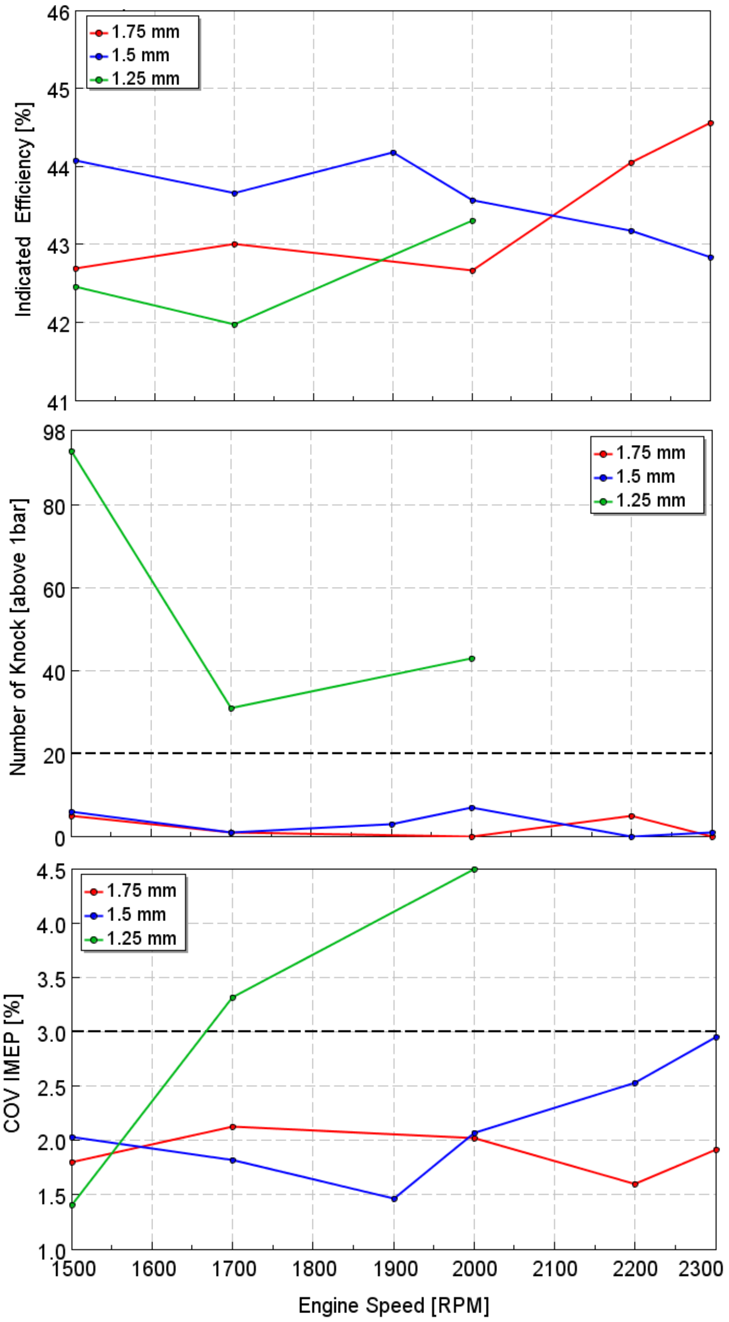

Figure 2.12 *DM-TJI engine gross indicated efficiency, number of knock cycles above 1 bar, and coefficient of variation of IMEP*$_g$ *with engine speed for orifice diameter 1.25mm, 1.5mm, and 1.75mm.*

The maximum indicated efficiency obtained using orifice diameter 1.25mm is 43.3 % at an engine speed of 2000 rpm. However, the COV_{IMEP} is above the 3% limit range, and the number of knock cycles is above the 20-limit range. Orifice diameter of 1.5mm has better efficiency in the speed range of 1500-2000 rpm than the other orifices. The maximum indicated efficiency is 44.18% at an engine speed of 1900 rpm with a COV_{IMEP} of 1.5%. On the other hand, 1.75mm orifice diameter performs better in the high engine speed ranges between 2100-2300 rpm. The maximum indicated efficiency is 44.56 % at an engine speed of 2300 rpm with a COV_{IMEP} of 1.9%. This indicates that 1.5mm is a better orifice diameter for low engine speed operation, and 1.75mm orifice diameter is better for high engine speed operation for the DM-TJI engine. However, for the majority LDV operating condition 1.5mm orifice diameter is better candidate.

The engine brake thermal efficiency calculation was conducted considering engine friction loss and additional work input for auxiliary pre-chamber air supply. The engine frictional loss were estimated using the empirical equation of Chen-Flynn friction correlation [61]. The equation implemented on GT-power model that represent the single cylinder DM-TJI metal engine to estimate the frictional loss. The additional work required for the auxiliary pre-chamber air supply was estimated using the Womack fluid power design data sheet [62], which calculates the power required to compress the purge air with an assumed 85% isentropic efficiency. The flow of auxiliary air supply in the experiment was measured by LFE flow measurement and used as input for work input calculation.

Figure 2.13 presents the DM-TJI engine estimated brake efficiency using orifice diameters of 1.5mm and 1.75mm between the engine speeds of 1500 – 2300 rpm. The maximum brake efficiency results were 39.2% and 39.5% for 1.5 and 1.75mm orifice diameters, respectively. A conventional engine with a similar compression ratio (MAZDA SkyActiv 2.0L 13:1 compression ratio) brake thermal efficiency was reported on [63] with a maximum value of 37%. Compared to the MAZDA conventional engine, the DM-TJI engine performs with 6.8% higher efficiency.

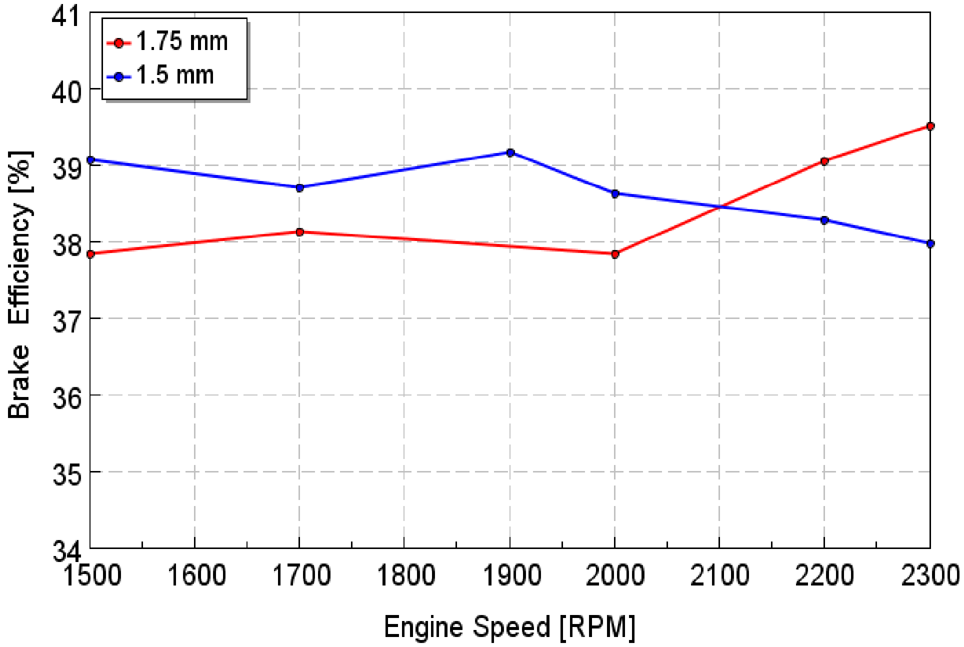

Figure 2.13 *DM-TJI engine brake efficiency using orifice diameter 1.5mm and 1.75mm variation with engine speed*

2.7 Summary and Conclusion

This chapter first discussed the pre-chamber ignition concept and the development progress with different arrangements and prototypes. Three pre-chamber nozzle orifice diameters were examined at different loads and speeds using the DM-TJI Prototype III metal engine installed at Michigan State University's Energy and Automotive Research Laboratory. The maximum engine efficiency was evaluated, and the following conclusions are drawn from the experiments performed.

- The DM-TJI engine with a compression ratio of 13.3:1 was able to maintain a stable run ($COV_{IMEP} < 3$) with 40 % and 45% external EGR dilution at stoichiometric conditions (λ~1).

- Three nozzle orifice diameters (1.25, 1.5, and 1.75mm) were tested at 40% EGR diluted stoichiometric operating conditions for the impact of engine speed variation. The 1.25mm orifice diameter provided fast combustion compared to the orifice diameter of 1.5 and 1.75mm. However, when the engine speed increased, the combustion stability of the smaller diameter suffered. The pre- chamber auxiliary air mass flow rate decreased when the engine speed increased, and could cause an engine misfire at higher engine speed.
- Numerical model analysis was conducted using GT-Power software. The analysis showed that the 1.25mm orifice diameter pressure trace was affected by airflow resistance. The peak pressure shifted by 7 CAD from the TDCF. This lagging pressure trace increased when engine speed increased, and there might not be enough time to purge the pre-chamber from the previous combustion residual and make it ready for the subsequent combustion mixture preparation. This effect could multiply for firing pressure trace and initiate engine misfire.
- The orifice diameter of 1.5mm displayed better efficiency in the 1500–2000 rpm speed range. It exhibited a maximum indicated efficiency of 44.18% at an engine speed of 1900rpm with a COVIMEP of 1.5%.
- In contrast, the 1.75mm orifice diameter performed better in the high engine speed ranges between 2100 and 2300 rpm. It showed a maximum indicated efficiency of 44.56% at an engine speed of 2300 rpm with a COVIMEP of 1.9%.
- After considering friction loss and additional pump work to the pre-chamber, the maximum brake efficiencies of 39.2% and 39.5% were estimated for 1.5 and 1.75mm orifice diameter, respectively.

This study has effectively demonstrated the capability of the DM-TJI system to work with a very high level of EGR dilution (up to 45%) and deliver a better efficiency than the conventional spark-ignition engine. Further numerical analysis and engine map development are discussed in the following chapters.

Chapter 3: Numerical Simulation of DM-TJI Engine

3.1 Introduction

In recent years, the engine development process has become a challenging task due to the increasing demands for performance, fuel efficiency, and emissions. The increasing demand has led to the development of more and more advanced design tools. Engine modeling has become a critical part of the internal combustion engine design process due to increased design parameters and existing alternative fuels. Hence, the development of advanced combustion engines is only possible with a combination of experimental and simulation methods. At present, many computer simulation tools are available to estimate the performance of internal combustion engines before their actual prototyping. The processes that occur through the engine cycles are complex because they include many physical phenomena such as fluid dynamics, heat transfer, thermodynamics, and chemical kinetics at various levels of complexity to predict combustion, emissions, and engine operating characteristics.

Engine modeling can be broadly divided into 0D/1D engine simulation tools and high-fidelity three-dimensional (3D) modeling platforms. The 0D/1D simulation tools are used for engine studies and optimizations when computationally expensive 3D simulations are impractical. Considering the computational costs of a 3D approach, an alternative solution is provided by 1D simulation. 1D models feature low computation costs/time and good accuracy in predicting engine performance with a maximum and average errors of 7% and 5%, respectively [64]. The reliability of the numerical results obtained from calibrated models allows the researcher to reduce the number of experiments carried out to obtain an optimized result.

3.2 Numerical Combustion Model

Engine models can be divided into two base thermodynamic and fluid dynamic-based model in which the governing equations, energy, and momentum, are solved in a flow domain. Thermodynamic energy conservation-based models split into two subcategories, multi-dimensional and zero-dimensional models [42]. Multi-dimensional models solve the equations numerically for mass, momentum, energy, and species conservation in three dimensions to predict the thermodynamic state at different positions. Zero-dimensional models are the simplest type since they do not require the combustion details and assume the same average state throughout the gas.

Zero-dimensional models are the most commonly used tools for parametric studies associated with engine development. Zero-dimensional models are further subdivided into single-zone, two-zone, and multi-zone combustion modeling. The working fluid is assumed a thermodynamic system in a single-zone mode, while the working fluid is divided into two thermodynamic systems consisting of burned and unburned zones in a two-zone model [65]. A single-zone model is often used if there is a need for a fast and preliminary engine performance analysis. In single-zone models, the cylinder charge is assumed to be uniform in both composition and temperature, and the first law of thermodynamics is used to calculate the mixture energy accounting for the enthalpy flux due to fuel injection. The fuel injected into the cylinder is assumed to mix instantaneously with the cylinder charge, which is assumed to behave as an ideal gas.

A widely used approach in engine models is the Wiebe function to determine the burned mass fraction. The Wiebe function is a zero-dimensional engine model widely used in engine development, particularly for SI applications. The Wiebe function given in Equation 3.1 has an Sshaped curve between zero indicating starting of combustion and one indicating the end of combustion [66].

$$x_b(\theta) = 1 - \exp\left[-a\left(\frac{\theta - \theta_0}{\Delta\theta}\right)^{m+1}\right] \tag{3.1}$$

where $x_b\ (\theta)$ is the mass fraction burned; θ is the crank angle; θ_0 is the crank angle at the start of combustion; $\Delta\theta$ is the combustion duration defined as the difference between θ_0 and the end of combustion; m is defined combustion characteristic exponent, determining the magnitude of the maximum burn rate and the time in which it is attained for a given burn duration, with effects on the shape of the S-curve (Figure 3.1), and a is the efficiency parameter because it controls the duration of the combustion process. With the assumption of mass fraction burned 99.9% at the end of the combustion, a has the value $a = -\ln(1 - x_b) = -ln\ 0.001 = 6.9$

The crank angle of any heat release fraction is found by solving equation 3.1 for θ. For example, the crank angle of 50% mass fraction burned is:

$$\theta_{50} = \theta_0 + \Delta\theta\left(\frac{\ln(1-0.5)}{\ln 0.001}\right)^{\frac{1}{m+1}} \tag{3.2}$$

Hence, the 10-90% burn duration is:

$$Burn_{1090} = \Delta\theta\left(\left(\frac{\ln(1-0.9)}{\ln 0.001}\right)^{\frac{1}{m+1}} - \left(\frac{\ln(1-0.1)}{\ln 0.001}\right)^{\frac{1}{m+1}}\right) \tag{3.3}$$

The mass burn fraction (MBF) curve versus CA can be obtained using in-cylinder pressure measurement during the engine cycle, based on energy balance and proper hypotheses and assumptions about heat exchange, combustion efficiency, blow-by rate, and piston crevices. Figure 3.1 compares the heat released during combustion; Q_{ch} is the sum of the net or apparent heat release

(Q_n) and the heat loss through the boundaries (Q_{ht}). The difference between the total Q_{ch} and the total fuel chemical energy $m_f Q_{LHV}$ is due to process inefficiency and blow-by effects. The apparent heat release rate is needed to determine the Wiebe function parameters.

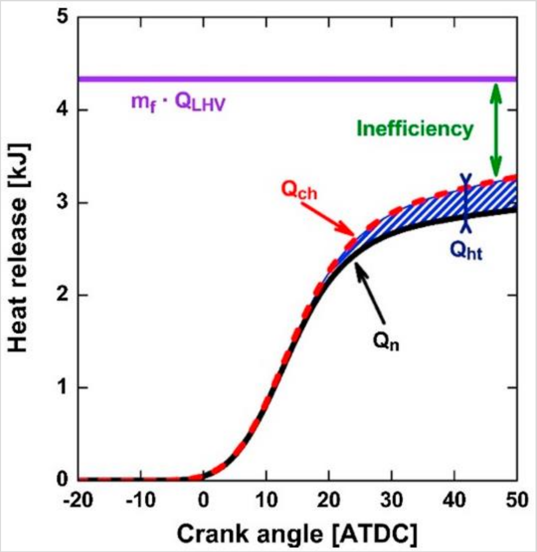

Figure 3.1 *In-cylinder heat release analysis* [66].

However, the standard Wiebe function was less accurate when large variations in the burning rate were present. To account for these variations, a second Wiebe function was introduced to describe the MBF. The second Wiebe function was associated with the slower combustion near the wall. With spark-ignition engines, Heywood et al [42] were among the first researchers to propose the use of a single Wiebe function to model the MBF. Up to present, this modeling approach is widely used both with single and double functions for engine modeling.

Various algorithms can be implemented to estimate the Wiebe parameters function from the MBF S-curve, mainly non-linear least-squares optimization methods resulting from experimental in-cylinder pressure data. After Wiebe parameters are estimated, the function can be used to reproduce the apparent heat release and reconstruct in-cylinder pressure during the engine cycle.

3.2.1 Predictive and Non-Predictive Combustion Model

Predictive combustion models attempt to model the essential physics in the combustion process to predict the combustion burn rate with varying engine parameters like engine speed, EGR rate, engine load, etc. In practical application, predictive combustion models include assumptions and simplifications of some of the test parameters; therefore, it will require some calibration of the physical constants to the best match of the specific combustion system. Zero-dimensional combustion models are recognized as predictive models capable of predicting engine performance in a reasonably wide operating range.

On the contrary, combustion models using a Wiebe function, representative of a specific engine working condition through a set of parameters experimentally identified, are intrinsically non-predictive since they are not based on physical models [67]. A non-predictive combustion model imposes a burn rate as a function of crank angle. This prescribed burn rate will be followed regardless of the conditions in the cylinder, assuming that there is sufficient fuel available in the cylinder to support the burn rate. In theory, predictive combustion models are an appropriate choice for all simulations. However, there are practical factors that make non-predictive combustion models preferable in certain situations. Predictive models typically require calibration data in order to provide accurate results.

Wiebe-based models can be an attractive choice in preliminary design studies when it is necessary to investigate variables which have a weak influence on burn rate. However, to give some predictive features to Wiebe-based models, it is necessary to find that Wiebe function parameters vary with the main variables characterizing engine operating conditions through properly identified functional relationships. A semi-predictive combustion model is sensitive to the significant variables that influence combustion rate and responds appropriately to changes in those variables but does not use any physical models to predict that response. Instead, these models utilize a non-predictive Wiebe-based methodology. The combustion burn rate imposed with lookups tables to calculate/predict the proper Wiebe parameters based on the significant input variables.

Similar works are found in the literature on predictive Wiebe-based models. Galino et al. [68] used the Wiebe function to predict the mean effective pressure. The function builds with multiple regression analysis, including significant engine parameters of charge density, residual gas fraction, spark timing, and mean piston speed. Maroteaux et al. [69] developed a Wiebe function system model to calibrate and simulate burn rate and validate against experimental operating conditions at low/medium engine speed. The model was created with five multiple regression correlation analysis as a functions of engine operating variables. Awad et al. [70] studied a single-zone thermodynamic model coupled with a triple-Wiebe function developed for a general form of equations useful for the prediction of engine performance on different types of fuel. The cylinder pressure was predicted and compared to experimental values. Sun et al. [71] developed a 1D simulation model of a diesel engine based on GT-Power software. A partial least square regression was imposed to relate the Wiebe parameters to the operating conditions such as speed, EGR rate, inlet temperature and pressure, exhaust temperature and pressure. Babajimopoulos et al. [72] discuss the development and application of a single-cylinder HCCI engine model within a 1-D engine simulation software framework. The paper proposes a heat release model using a first correlation defining the 0-50% burn interval as a function of ignition timing, engine speed, and equivalence ratio. A second correlation defines 0-90% burn interval as a function of the location of 50% heat release and equivalence ratio. Mishra et al. [73] worked on an optimized double Wiebe parameters matrix. It was formulated from experimental control variables such as premix ratio, engine load, and injection timing. The model predicted peak pressure, indicated mean effective pressure, and crank angle for 50% of fuel mass fraction burnt and maximum pressure rise rate. Hu et al. [74] studied the sensitivity of each Wiebe parameter, namely, the efficiency factor (a), form factor (m), crank angle of combustion start, and combustion crank angle duration. The sensitivity of each Wiebe parameter is positively associated with the heat release rate normalized by the total fuel energy but, the sensitivities of m and crank angle of combustion start are larger than the other parameters.

A literature survey indicates that the variable parameters of Wiebe function vary with engine operating conditions, fuels, and combustion systems. The current study deals with zero-dimensional, double zone modeling development using the Wiebe function for DM-TJI engine. In this work, a semi-predictive Wiebe-based combustion model is used for the combustion simulation performance of DM-TJI engine. Multiple regression correlation was identified to predict Wiebe parameters as a function of engine operating variables. The Wiebe function parameters are represented by: the angle at 50% of burned fuel, the combustion duration between 10% and 90% of burned fuel, and the form factor m. The regression correlations are developed from independent engine variables, including engine speed, the inlet manifold pressure, the inlet manifold temperature, spark timing, intake EGR percentage.

3.3 GT-Power Combustion Model

GT-Power is the leading engine and vehicle simulation tool used by engine makers and suppliers. It is suitable for the analyzing a wide range of subjects related to vehicle and engine performance. It uses a comprehensive partial differential equation-based 0D/1D engine modeling and simulation tool for engine development, performance simulation, and product calibration based on its high fidelity over different engine steady and transient conditions [75]. It can perform predictive cylinder combustion simulations, including numerical calculation of engine torque, power, specific fuel consumption, and volumetric efficiency [64]. The current study employs GT-Power as its modeling platform for the simulation of the Prototype III DM-TJI engine.

3.3.1 One-Dimensional DM-TJI Engine Model

A one-dimensional gas dynamics and thermodynamics code, GT-Power by Gamma Technologies, is established as a reliable and accurate simulation tool for combustion modeling. The experimental setup single-cylinder Prototype III DM-TJI metal engine was modeled with inlet and exhaust parts limited to the pipes where transient pressure is measured. In GT-Power, the apparent burn rate can be estimated using two methods, namely Cylinder Pressure Only Analysis (CPOA) and the Three Pressure Analysis (TPA) [60]. CPOA is a fast and stand-alone calculation that only requires one measured instantaneous pressure trace but has the downside of requiring measured values of exhaust gas residual fraction and cylinder trapping ratio, which are difficult to obtain.

The TPA method is used with the reverse run approach to determine the burn rate in this work. This approach requires three dynamic pressure measurements as input to the model: the cylinder pressure, the intake pressure, and the exhaust pressure. For this analysis, no estimation of the residual fraction and trapping ratio are needed as inputs, which would be the case with CPOA. The simulation runs for multiple cycles until the model has converged; as a result, the trapping ratio and residual fraction will be calculated. This method is referred as a "reverse run", because the inputs and outputs of the calculation are reversed from the typical combustion calculations in engine simulation. This approach requires accurate flow characteristics of the 1D model. It is pursued by isolating a single cylinder with its inlet and exhaust ports, whose corresponding measured pressures are imposed as boundary conditions in the model. The simulation first assumes an initial dummy burn rate used to estimate a first in-cylinder pressure profile and trapped conditions at inlet valve closing. These trapped conditions are used along with the measured pressure profile to calculate a subsequent burn rate for a forward run, and this is iterated cyclically, using the burn rate calculated in the previous step at each iteration until convergence is reached. The primary benefit of this approach is that in-cylinder trapped quantities are predicted by the simulation, including the trapping ratio and the residual fraction. The downsides of this approach are the additional measured data required and slower calculations due to the need to run the simulation cycles until convergence. In addition to the three pressures, the model uses the intake port temperature, EGR fraction, fuel injection, and spark timing as input. The pre-chamber model was prepared using GT-Power cylinder template. The cylinder is a constant volume by defining a non-moving piston with reference to bottom dead center over the entire engine cycle and defining the minimum value allowed (1.001) for compression ratio.

TPA analysis verifies the plausibility of experimental data by analyzing burn rate input data consistency checks. The critera used for this consistency check and selection were different and concurrent. This step gives the possibility of testing the accuracy level of the 1D model regarding the inlet/exhaust systems by comparing the simulated pressure profile with the experimental one. For example:

- There should be no fuel burning during the compression stroke until the designated start of combustion analysis. If the cumulative burn during compression is greater than 2% of the total fuel, it indicates an error in the input data, and the simulation is flagged as an error.

- The simulated fuel mass, fuel-air ratio, air mass at intake valve close, and low heating value multiplier are compared to the corresponding measured values of an experimental operating point. The simulation is flagged as an error where their difference is greater than 5%.
- Cylinder pressure shift of more than 0.5 bar results in the simulation being flagged as an error.

3.3.2 Flow Model

The Prototype III DM-TJI engine model includes the intake/exhaust runner, intake/exhaust valves, auxiliary pre-chamber valve, and compressed air supply. The engine models can be divided into two categories: thermodynamic and fluid dynamic-based, in which the governing equations, energy, and momentum, are solved in a flow domain. The flow model involves the solution of the Navier-Stokes equations, namely, the equations of continuity, conservation of energy and momentum are adapted and simplified for implementation in GT-Power [60,64].

$$\frac{dm}{dt} = \sum\nolimits_{boun.} \dot{m} \tag{3.4}$$

Where $\dot{m}$ is boundary mass flux into volume and m mass of the volume

$$\frac{d(me)}{dt} = -p\frac{dv}{dt} + \sum\nolimits_{bound.} (\dot{m}H) - hA_s(T_f - T_w) \tag{3.5}$$

Where e is total specific internal energy, p is pressure, V is volume, H is total specific enthalpy, h is heat transfer coefficient, A_s is heat transfer surface area, T_f fluid temperature, and T_w is wall temperature.

$$\frac{d\dot{m}}{dt} = \frac{dpA + \sum_{bound.}(\dot{m}u) - 4C_f \frac{\rho u^2}{2}\frac{dxA}{D} - K_p\left(\frac{\rho u^2}{2}\right)A}{dx} \tag{3.6}$$

Where dp is pressure differential acting across dx, A cross-sectional flow area, u velocity at the boundary, C_f fanning friction factor, ρ density, dx discretization length of the mass element in the flow direction, K_p pressure loss coefficient commonly due to bend, taper, or restriction.

The flow equations are solved by an explicit method: the right-hand side of the equations is calculated using values from the previous time step. This yields the derivative of the primary variables and allows the value at the new time to be calculated by integration of that derivative over the time step. At each time step, the pressure and temperature are calculated in the following order. First, the continuity and energy equations determine the mass and energy in the volume. Then, with the volume and mass known, the density is calculated yielding density and energy. Finally, the equations of state for each species define density and energy as a function of pressure and temperature. The solver will iterate on pressure and temperature until they satisfy the density and energy already calculated for this time step.

3.3.3 Two-zone Combustion Model

The thermodynamic energy conservation-based engine cylinder model can be split into two subcategories; quasi-dimensional and zero-dimensional models. The simplest type of these models is the zero-dimension model since it does not require the combustion details. Zero-dimension models are further subdivided into single-zone, two-zone and multi-zone combustion modeling. Two-zone combustion applies to all GT-Power combustion models except for HCCI and the predictive diesel engine models. At the start of combustion, the cylinder is divided into unburned and burned zones.

In GT-Power, all the contents of the cylinder start in the unburned zone, including fuel and internal or external exhaust gas recirculation. At each time step, the combustion rate of heat release is in charge of mass transfer from the unburned zone to the burned zone. The amount of fuel-air mixture that is transferred to the burned zone is defined by the burn rate and the burn rate is imposed directly to the cylinder object in GT-Power simulations through predictive, semi-predictive, and non-predictive combustion models. A chemical equilibrium calculation is carried out for the entire burned zone, when the unburned fuel and associated air are transferred from the unburned to burned zone in a given time step. This calculation takes into account all of the atoms of each species present in the burned zone at that time (C, H, O, N, S, and Ar), and obtains from these an equilibrium concentration of the 13 products of combustion species (N_2, O_2, H_2O, CO_2, CO, H_2, N, O, H, NO, OH, SO_2, and Ar). The equilibrium concentrations of the species depend strongly on the current burned zone temperature and pressure. After the burned zone new composition is obtained, the internal energy of each species is calculated and the energy of the whole burned zone is obtained by summation over all of the species. Finally the new unburned and burned zone temperature and cylinder pressure are obtained by applying the principle of energy conservation. The energy balance equation of the unburned and burned zone are shown in equation 3.7 and 3.8 respectively. The energy equations are solved in each time step [60]. The right hand of the unburned zone energy equation includes pressure work, heat transfer, combustion, the addition of enthalpy from injected fuel, and the instantaneous rate of fuel consumption or burn rate.

$$\frac{dm_u e_u}{dt} = -p\frac{dV_u}{dt} - Q_u - \left(\frac{dm_{f,b}}{dt}h_f + \frac{dm_{a,b}}{dt}h_a\right) + \frac{dm_{f,i}}{dt}h_{f,i} \qquad 3.7$$

Where, m_u = unburned zone mass, e_u unburned zone energy, p in-cylinder pressure, V_u unburned zone volume, Q_u unburned zone heat transfer, $m_{f,b}$ the fuel mass transferred to burned zone, h_f enthalpy of fuel mass, $m_{a,b}$ the air mass transferred to burned zone, h_a enthalpy of air mass, $m_{f,i}$ the injected fuel mass, $h_{f,i}$ the enthalpy of injected fuel mass.

$$\frac{dm_b e_b}{dt} = -p\frac{dV_b}{dt} - Q_b - \left(\frac{dm_{f,b}}{dt}h_f + \frac{dm_{a,b}}{dt}h_a\right) \qquad 3.8$$

Where, the subscript 'b' denotes burned zone.

The apparent heat release calculated by GT-Power is similar to the apparent gross heat release rate defined by Heywood [42]. The calculation of the gross heat release is more involved and requires calculating the heat transfer rate to the walls to isolate the energy released by the combustion of the fuel. On the other hand, the net heat release calculation is much simpler than that of the gross heat release. It requires only the cylinder pressure and volume. However, this method does not report the chemical energy release rate, but it calculates the difference between the chemical energy release and heat transfer rate to the walls. The apparent rate of heat release given by equation 3.9 is solved after each time step using the results from that time step as an input. In other words, the calculation of heat release is a post-processing result that uses the results of the forward-run combustion as inputs.

$$AHRR = -p\frac{dV}{dt} - \frac{dQ}{dt} - \frac{d(me_s)}{dt} + \sum_i \dot{m}_i h_{i,s} \qquad 3.9$$

3.3.4 Cylinder Heat Transfer Model

GT-Power simulates the heat transfer analysis in-cylinder using the WoschniGT heat transfer model calculated by a formula which closely emulates the classical Woschni correlation without swirl. The difference lies in the treatment of heat transfer coefficients during the period when the cylinder valves are open where the heat transfer is increased by inflow velocities through the intake valves and also by backflow through the exhaust valves. This option is recommended when measured swirl data is not available [60]. With the cylinder bore B taken as the characteristic length, with w as a local average gas velocity in the cylinder, the convective heat transfer coefficient for the Woschni models is calculated as follows.

$$h_{c(Woschni)} = \frac{K_1 p^{0.8} w^{0.8}}{B^{0.2} T^{K_2}} \qquad 3.10$$

where, $h_{c(Woschni)}$ is the convective heat transfer coefficient; K_1 and K_2 are given constants as 3.01 and 0.50, respectively; p is the cylinder pressure; B is the cylinder bore; T is the cylinder temperature; and w is the average cylinder gas velocity (calculated using equation 3.10).

$$w = C_1 \bar{S}_p + C_2 \frac{V_d T_r}{P_r V_r}(p - p_m) \qquad 3.11$$

where, C_1 and C_2 are constants given in equation below; $\bar{S}_p$ is the mean piston speed; $V_d$engine is the displacement volume; $T_r$is the working fluid temperature prior to combustion; P_r is the working fluid pressure prior to combustion; V_r is the working fluid volume prior to combustion; p instantaneous fluid pressure; p_m is the motoring in-cylinder pressure at the same angle as p.

For WoschniGT, C_1 and C_2 are defined as follows:

$$C_1 = 2.28 + 3.9\, Min\left(\frac{\dot{m}_{in}}{m_{cyl} * f}, 1\right) \qquad 3.12$$

Where, $\dot{m}_{in}$ is instantaneous mass flow rate, summed over valves and orifices through which flow is currently entering cylinder; m_{cyl} instantaneous cylinder mass; f is engine frequency. C_2 is 0 during cylinder gas exchange and compression and it is 3.24e-3 during combustion and expansion.

3.4 Experimental Setup

The engine used in this study is a single-cylinder Prototype III DM-TJI metal engine. The engine stroke was 95 mm, and the bore was 86 mm with a connecting rod length of 170 mm. Table 3.1

shows the experimental engine specifications and intake manifold with pockets for port fuel injectors designed and installed for injection of main-chamber fuel. The recirculating exhaust gas cools down before it reaches the EGR valve assembly using the EGR cooler. Upstream throttles, a blow-off valve, and an EGR valve are used to control intake conditions for boosted operation. A large intake plenum was implemented to ensure proper mixing of EGR before it entered the combustion chamber. The intake air-EGR mixture temperature was maintained at 45°C for all the tests.

Table 3.1 *Engine specification used for engine map model*

Parameter	**Description**
Bore, Stroke, and Connecting rod length	86 mm, 95 mm and 170 mm, respectively
Main chamber swept volume	0.55 L
Number of cylinder	1
Engine strokes	4
Compression ratio	13.3:1
Fuel injection pressure	100 bar
Pre-chamber volume	2900 mm^3 (~6 % of clearance volume)
Number of Nozzle orifice, diameter and configuration	6 holes, 1.5 mm, and Symmetric
Pre-chamber air supply pressure	30-75 psi (gauge)
Number of Valves	2-intake, 2-exhaust and 1-pre-chamber
Valve timing for max lift	Intake timing - 90 CAD aTDCGE, Air valve timing - 110 CAD bTDCF Exhaust timing - 90 CAD bTDCGE
Fuel injection pressure	100 bar

The pre-chamber ignition system used in this study is a redesigned prototype III Jetfire® cartridge. The Jetfire® cartridge design packages contain the conventional spark plug, fuel injector, and auxiliary air valve. The engine head has a pent roof head modified to incorporate the pre-chamber

Jetfire® cartridge and air-valve driving assembly. Details and a figure of pre-chamber cartridge presented in Chapter 5, Section 2.4.2 and Figure 2.7, respectively.

The engine was tested in a fully instrumented engine test cell with all the standard temperature, pressure, humidity and engine specific measurements including airflow, fuel flow, dynamometer and emission test bench as shown in Figure 2.5. An in-house control system containing NI-PXI chassis and Mototron ECM-5554 controllers managed within an NI Veristand environment was used to control the main engine control parameters such as spark timing, pre- and main chamber fuel injection timings and durations, intake runner throttle and EGR valve positions. Details of engine test instrumentation are discussed in Chapter 5, Section 2.4.3. All tests were performed with the Environmental Protection Agency (EPA) Tier 3 emission certification fuel general testing regular gasoline.

3.5 Result and Discussion

3.5.1 0D/1D DM-TJI Engine TPA Model Development and Validation

Various driving cycles engine operating range experimental data was acquired for the engine model calibration and validation. A summary of engine experimental operating matrix shown in Table 3.2 and Figure 3.2. The data points vary based on engine speed, engine load, EGR inlet percentage, spark timing, and pre-chamber auxiliary inlet air pressure. More than one data points was taken on each engine operating point by varying spark timing and EGR dilution rate. The engine system model developed was calibrated based on experimental data. The model was validated by experiments with different operating conditions upon GT-Power model calibration, as shown in Figure 3.2.

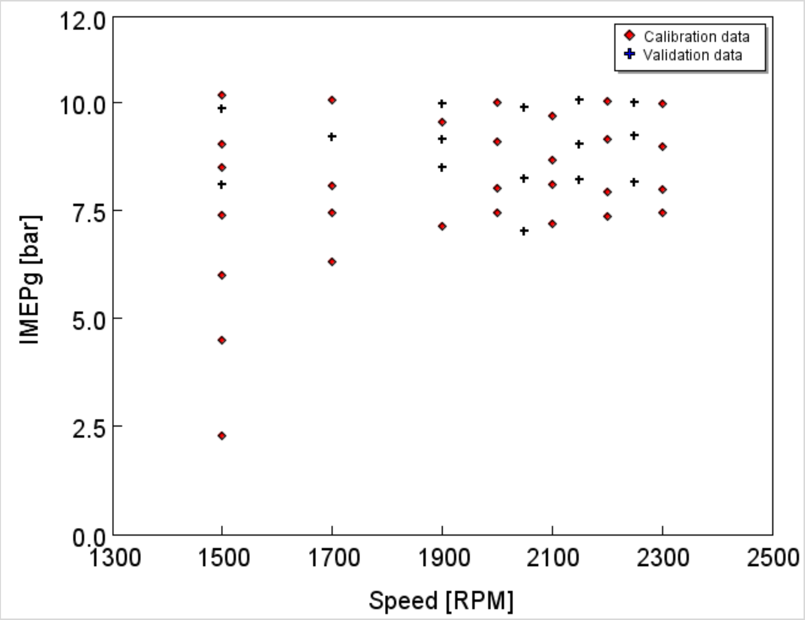

Figure 3.2 *Engine operating points for calibration and validation*

The EGR intake percentage and pre-chamber auxiliary air upstream pressure mainly depend on the engine load. Lower load demands a lower EGR percentage and low pre-chamber auxiliary air upstream pressure. Higher load demands a higher amount of EGR percentage and pre-chamber auxiliary air upstream pressure.

Table 3.2 *Engine operating variations and range*

Engine operating parameter	**Variation Range**
Engine Speed [RPM]	1500 – 2300
Engine Load [bar]	2.5 – 10
EGR [%]	18 – 49
Pre-chamber auxiliary air upstream pressure [psi]	30 – 75

From the experimental matrix points, engine operating points were selected after the test points passed TPA burn rate data consistency checks. These running points were used to create the experimental database to develop a 1D model of the engine in GT-Power. Figure 3.3 and Figure 3.4 show the comparison of experimental and 0D/1D model simulation accuracy of in-cylinder pressure trace and inlet/exhaust phasing.

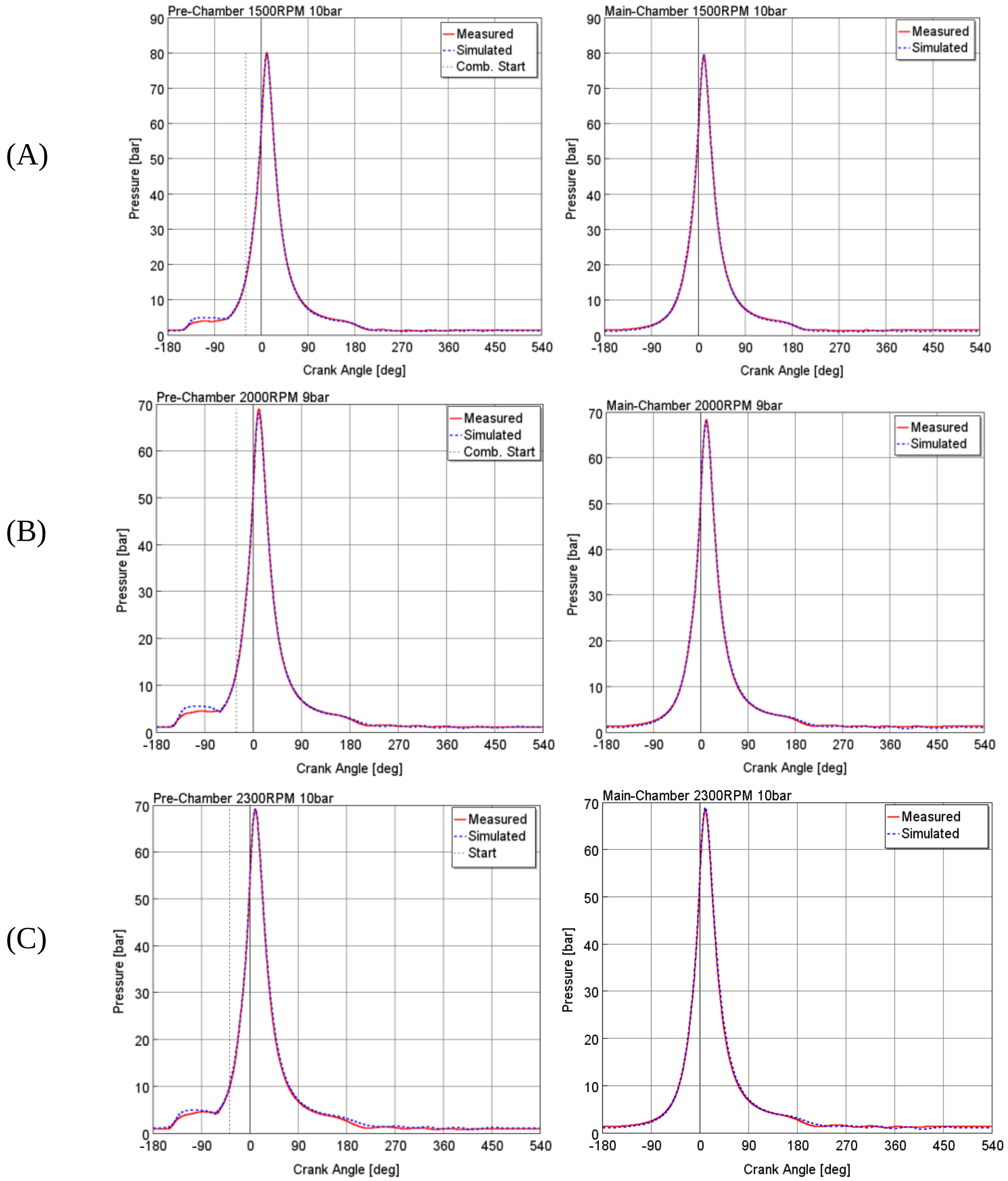

Figure 3.3 *Comparison of experimental and 0D/1D TPA model simulation in-cylinder pressure trace for pre- and main chamber (A) 1500rpm and 10bar IMEP (B) 2000rpm and 9bar IMEP (C) 2300rpm and 10bar IMEP*

The experimental result and the 0D/1D TPA model simulations result are in good agreement, as shown in the Figure 3.3. The simulation result achieved a reasonable degree of accuracy of peak cylinder pressure within a percentage of error of 0.42 – 1.2 % for both pre- and main chamber pressure. This shows that the model was able to simulate the peak pressure at all engine speeds and loads that the experiment undertook.

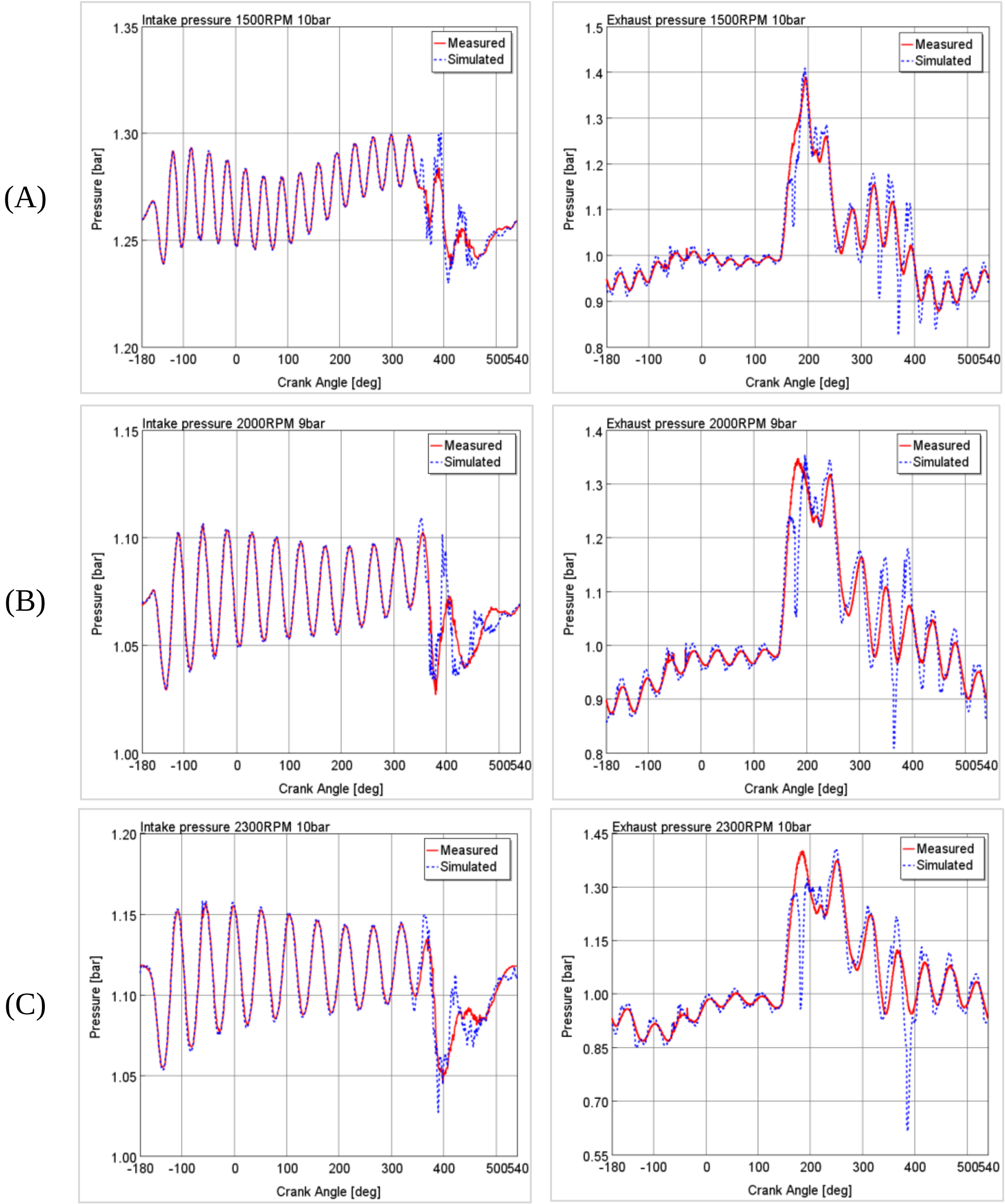

Figure 3.4 *Comparison of experimental and 0D/1D TPA model simulation intake/exhaust instantaneous pressure trace (A) 1500rpm and 10bar IMEP (B) 2000rpm and 9bar IMEP (C) 2300rpm and 10bar IMEP*

The intake/exhaust experimental runner pressure traces were also in a good agreement with the simulation except at the valve opening, which shown a pressure fluctuation. However, the average inlet/exhaust pressure values achieved a good degree of accuracy within percentage error of 0.09 – 0.57 %.

The selected experimental running points were used on the TPA model calibration. The calibration quality was checked at the end of each model simulation using the fuel flow, the lambda values and the IMEPg prediction. Fuel flow and lambda values were checked and kept the same as the experimental values. The simulated IMPEg value was compared with the experimental measured value. Figure 3.5 shows the percentage error of each running point, and these errors are in the range of between -1.48% and 3.33%. This shows that the 0D/1D model of the DM-TJI engine is well-calibrated, and the prediction percentage error validates the calibration.

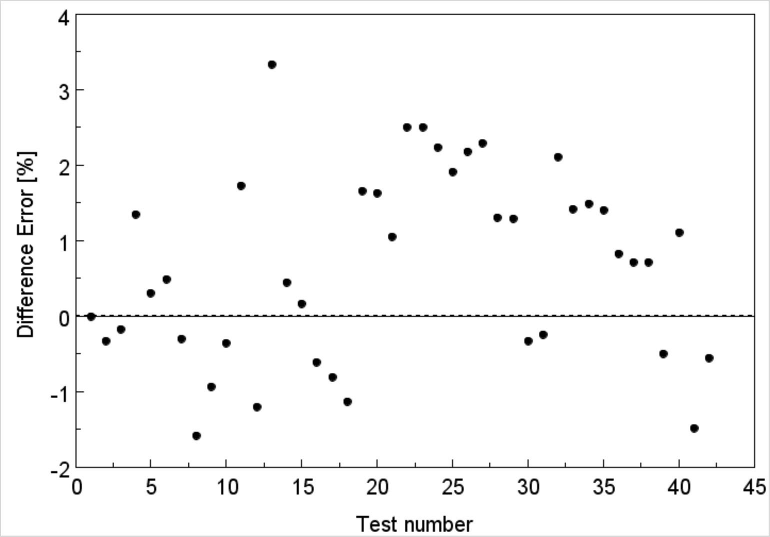

***Figure 3.5** Experimental and predicted IMEPg difference percent error*

3.5.2 Wiebe-based Combustion Model Correlated with Operating Variables

The TPA cylinder pressure analysis calculates the burn percentage at 2%, 5%, 10%, 20%, 50%, 75%, 90%, and 99%. It also calculates burn duration of crank angle degrees from the start of combustion 10% burned point to the 75% burned point and from the 10% burned point to the 90% burned point. Using the 50% burn point (CA50) and the 10-90% burn duration (Burn1090), the Wiebe exponent (m) was determined by the least square method that best fits the burning curve predicted by the cylinder pressure analysis. Thus, only the two burning rate parameters (CA50, Burn1090) and Wiebe exponent (m) are required for the Wiebe-based combustion model.

A database of burning parameter and Wiebe exponent was created for both pre- and main chamber using the selected experimental running points from the in-cylinder pressure. Assuming the CA50, Burn1090, and m as dependent variables, the rest of the multiple engine-operating variables (manifold pressure, manifold temperature, spark timing, the laminar flame speed at the start of combustion, engine speed, and EGR dilution rate) and dependence relationship were evaluated with scatterplots and correlation tables. The key variables in the experimental database were examined using the various tools provided by Statgraphics Centurion XVI software, which is widely used for statistical analysis and the development of regression functions. Three different correlations that predict the value of CA50, Burn1090 and, m were found from the selected engine-operating variables using linear regressions. The dependent engine-operating variable was selected based on the best performance parameters measured using statistical tools of adjusted R-squared, Standard Error of the Estimate, and Mean Absolute Error. Among multiple engine-operating variable the manifold pressure, manifold temperature, spark timing, engine speed, and EGR dilution were selected as input for the regression function based on the results of statistical tools. Figure 3.6 shows CA50 predicted versus experimentally observed comparison and standardized residual versus predicted. The output of the CA50 regression correlation shows the results of fitting a multiple linear regression model to describe the relationship between CA 50 and 5 independent variables. The adjusted R-Squared statistic indicates that the model as fitted explains 93.2% of the variability in CA50. The standard error of the estimate shows the standard deviation of the residuals to be 1.3. The mean absolute error of 0.97 is the average value of the residuals.

Figure 3.7 shows Burn1090 predicted versus experimentally observed comparison and residual versus predicted. The adjusted R-Squared statistic indicates that the model as fitted explains 93.4% of the variability in Burn 1090. The standard error of the estimate shows the standard deviation of the residuals to be 1.08. The mean absolute error of 0.83 is the average value of the residuals.

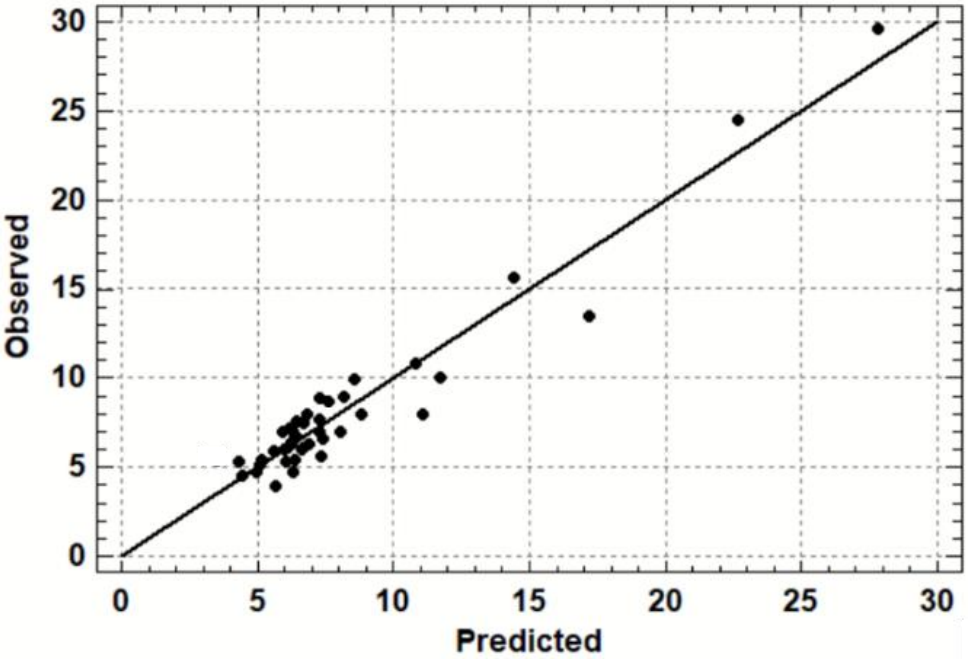

Figure 3.6 *CA50 predicted and experimentally observed correlation*

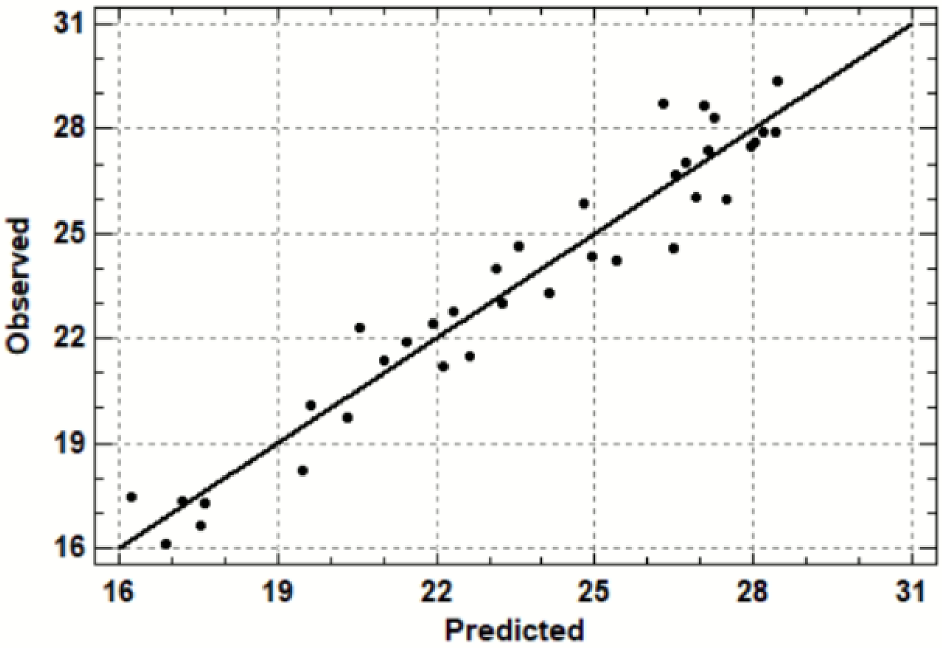

Figure 3.7 *Burn1090 predicted and experimentally observed correlation*

Figure 3.8 shows the last regression correlation of Wiebe exponent m predicted versus experimentally observed comparison and residual versus predicted. For this correlation, CA50 and Burn1090 were used as input. The adjusted R-Squared statistic indicates that the model as fitted explains 86.3% of the variability. The standard error of the estimate shows the standard deviation of the residuals to be 0.36. The mean absolute error of 0.25 is the average value of the residuals.

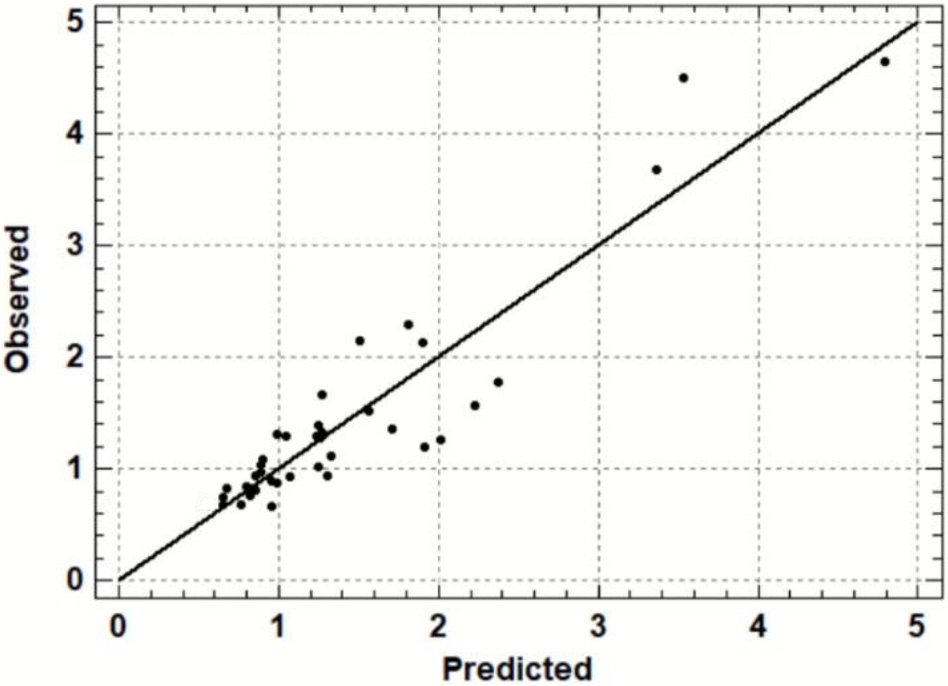

__Figure 3.8__ Wiebe exponent predicted and experimentally observed correlation

3.5.3 Validation of the Wiebe-based Combustion Model

The developed regression correlation was embedded in the 1D DM-TJI engine GT-Power model with 0D combustion model approach. Validation and calibration engine testing parameters were used as input to determine the Wiebe functions of CA50, Burn1090 and m. These parameters were used to develop the GT-Power combustion objective and the corresponding MBF curve. Figure 3.9 shows the correlation plots of IMEPg for the proposed Wiebe-based combustion model and experimental result. In general, the numerical simulations were able to capture the experimental trends. The model's validity in the prediction of experiments was observed based on the standard metric of the coefficient of determination, R^2 as shown in the figure. The two dash-dot lines on each side of the data points show the ± 5% error boundaries with respect to the continuous line representing 0% difference. Most of the numerical predictions for IMEPg are in the ± 5% limits range of experimental data, with the coefficient of determination $R^2 = 0.987$ except at a low load below 6 bar which is at the limit of ± 6%.

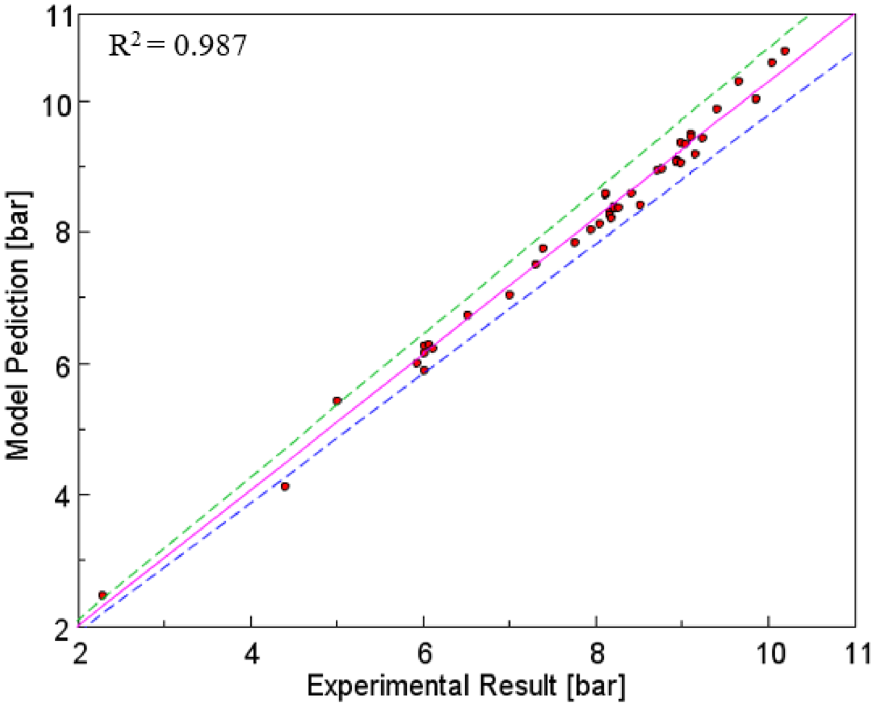

Figure 3.9 *Correlation of IMEPg for proposed Wiebe-based combustion model and experimental result.*

The numerical predictions' main chamber in-cylinder peak pressure was compared with the experimental result to validate the model further. Figure 3.10 compares the main chamber peak pressure, the Wiebe-based combustion model, with the experimental result. All the numerical predictions were within the ± 5% limits, with the mean of the Coefficient of determination $R^2 =$ 0.992.

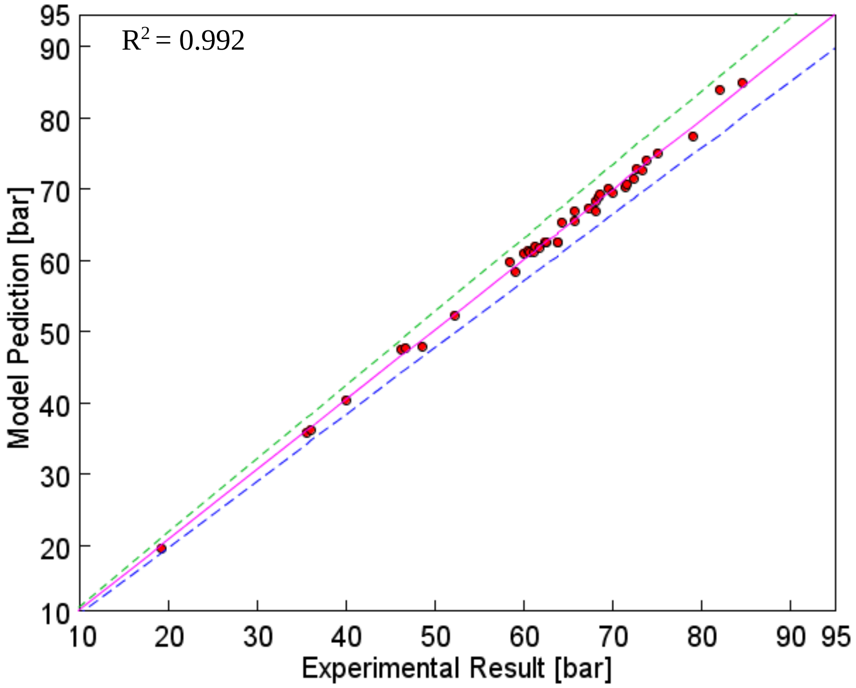

Figure 3.10 *Comparison of main chamber peak pressure Wiebe-based combustion model and experimental result.*

The numerical predicted in-cylinder main chamber pressure was compared with the experimental result at each crank angle. Figure 3.11 shows the in-cylinder pressure trace comparison of main chamber that contains experimental measured, model prediction simulation and the difference of the two residual (error) for the selected validation running points. The model prediction can capture the measured in-cylinder pressure at each crank angle within a maximum residual of ± 3 bar. The residual absolute root mean square (RMS) was below 0.61.

.

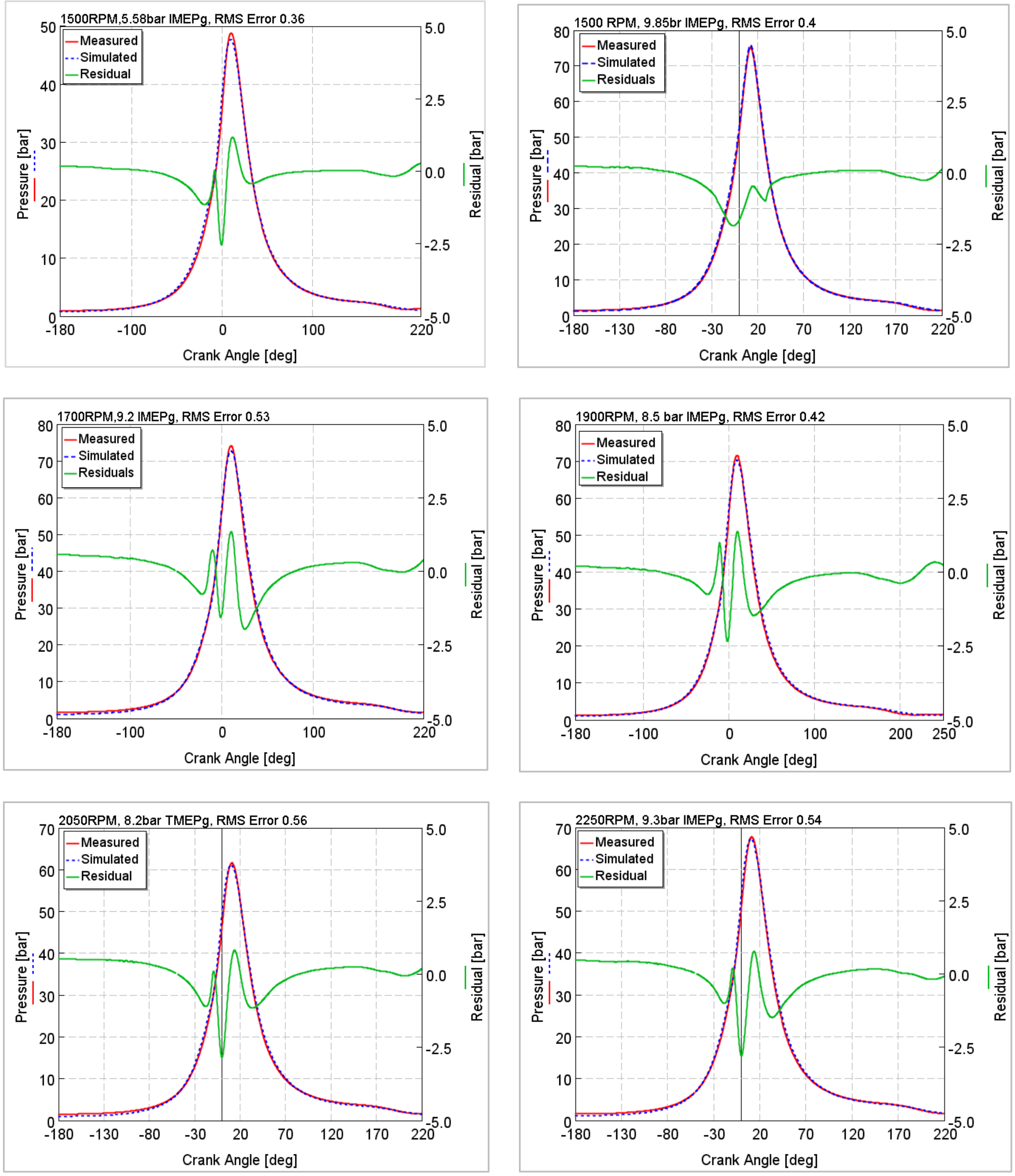

Figure 3.11 *In-cylinder pressure trace comparison of main chamber; experimental measured, model-predicted simulation and the residual.*

From the validation point of consistency and reliability, it was seen that the DM-TJI engine model was able to reproduce the experimental result. Such a model is essential to project the behavior of an engine equipped with the DM-TJI combustion technology over the entire engine map, especially the points which are difficult to cover from the experiment. The flowchart in Figure 3.12 summarizes the engine modeling calibration, validation, and predictive model creation.

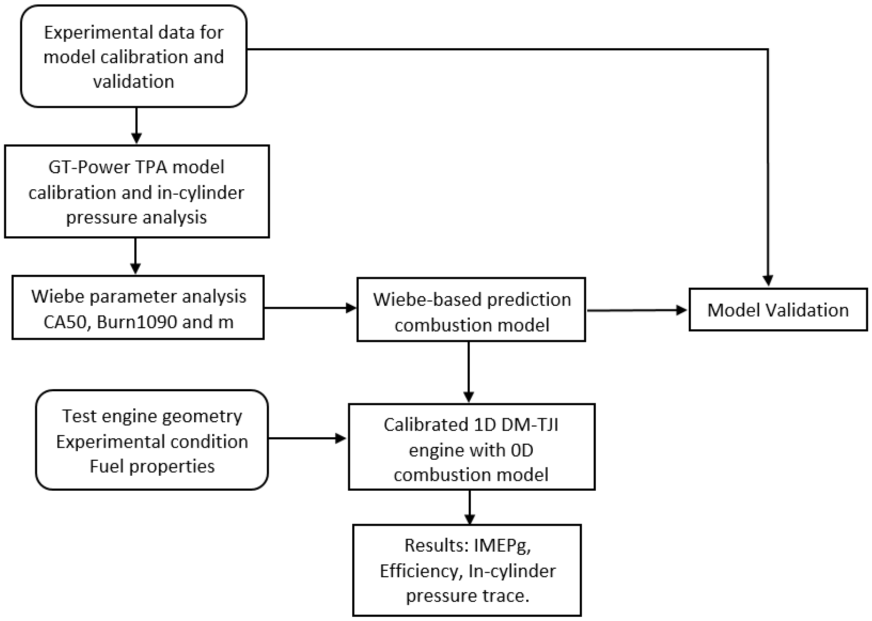

Figure 3.12 *Flowchart outlining the calibration, validation, and Wiebe-based predictive combustion model process for 0D/1D GT-Power simulation model.*

3.5.4 DM-TJI Engine Maps Under a High-EGR Dilution Rate

The DM-TJI four-cylinder engine map was created using the experimental test and GT-Power calibrated prediction model. The experimental result was chosen based on the best efficiency points after applying spark swept and EGR dilution variation on specific running points. The rest of the engine map points were covered by the calibrated GT-Power model. The engine's mean effective pressure and thermal brake efficiency are calculated after considering additional work input for auxiliary pre-chamber air supply and engine friction loss. The additional work required for the auxiliary pre-chamber air supply was estimated using the Womack fluid power design data sheet [62], which calculates the power required to compress the purge air with an assumed 85% isentropic efficiency of the compressor. The flow of auxiliary air supply in the experiment was measured by LFE flow measurement used as input for work input calculation.

The lost mechanical work is the sum of pumping losses, actual friction or mechanical rubbing losses, and auxiliary device losses. It is represented by a single term of friction mean effective pressure (FMEP). In order to obtain the brake mean effective pressure (BMEP), which is the actual engine output, a sub-model for FMEP evaluation must be employed. A model as proposed in the literature [76–78] was employed. One of the most encountered models in literature and employed in commercial software is the Chen-Flynn model [61]. The single cylinder engine friction modeled on GT-Power also uses the empirical equation of Chen-Flynn friction correlation. This correlation is used to calculate the FMEP of an engine (equation 3.11 and 3.12). According to this model, the FMEP [bar] is function of the cylinder maximum pressure P_{max} [bar] and an engine speed factor S_f [rad·m/s].

$$FMEP = A + B \cdot P_{max} + C \cdot S_f + D \cdot S_f^2 \qquad 3.11$$

$$S_f = \frac{\omega \cdot S}{2} \qquad 3.12$$

Where, A [bar] is constant which accounts for the auxiliary losses and other invariable factors; B is constant which accounts for the load effect of the engine (in-cylinder pressure); C [bar · s/m] and D [bar · s^2/m^2] constants which accounts for the effect of the engine speed; ω [rad/s] is engine speed; S [m] is piston stroke.

The maximum pressure and engine speed determined form the calibrated GT-Power model with the constant values taken from the GT-Power recommended value ranges after tuned to motoring data (A= 0.3bar, B=0.004, C=0.08bar s/m and D should be set to 0.0 when the rest values are within the recommended ranges),

Figure 3.13 shows the EGR dilution rate of the DM-TJI engine map. The maximum dilution rate for the map was 45% between 6 and 14 BMEP, and the lowest dilution rate was at a low load of 2.5 bar with 15%. Figure 3.14 and Figure 3.15 show the brake thermal efficiency map and the BSFC map of the DM-TJI engine in a four-cylinder boosted configuration under highly diluted conditions up to 45% EGR after considering engine friction and pre-chamber auxiliary air supply power input.

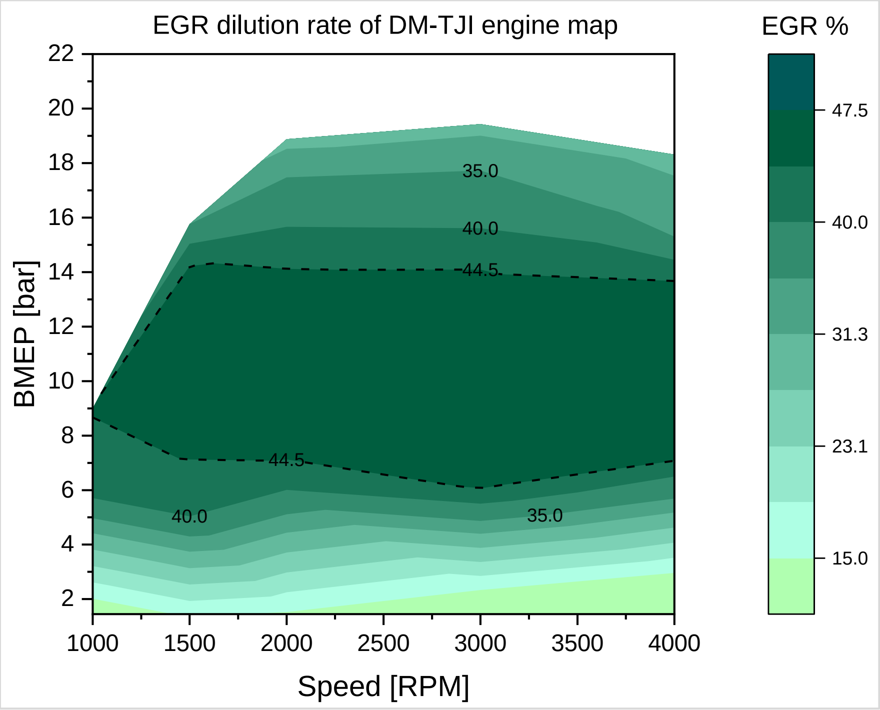

Figure 3.13 *EGR dilution rate of the DM-TJI engine map*

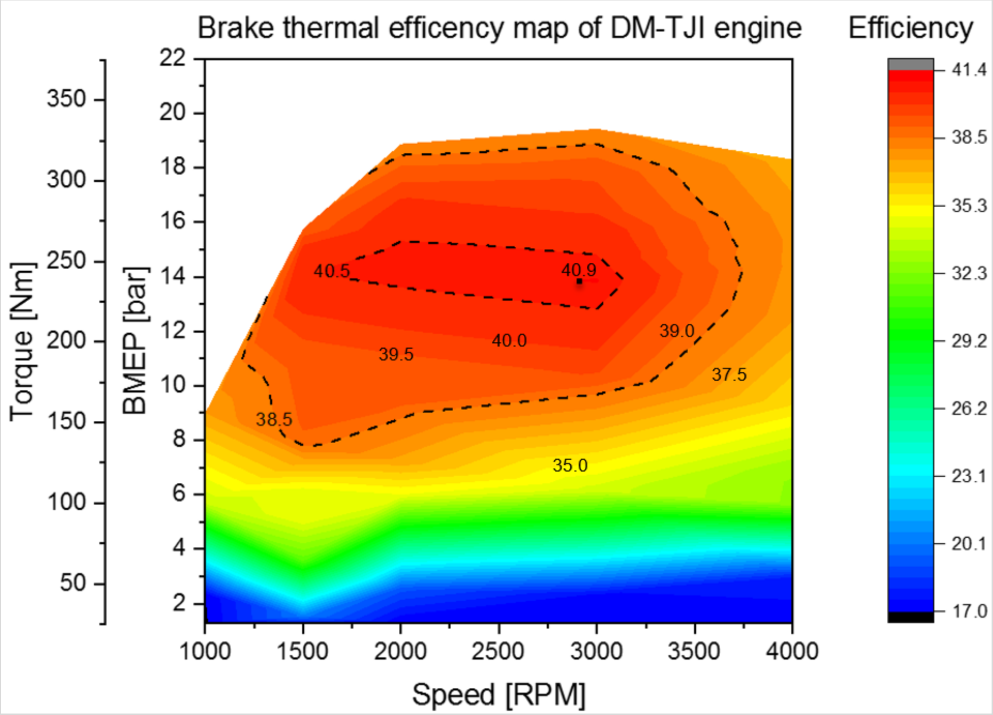

Figure 3.14 *Brake thermal efficiency map of DM-TJI engine with high EGR dilution*

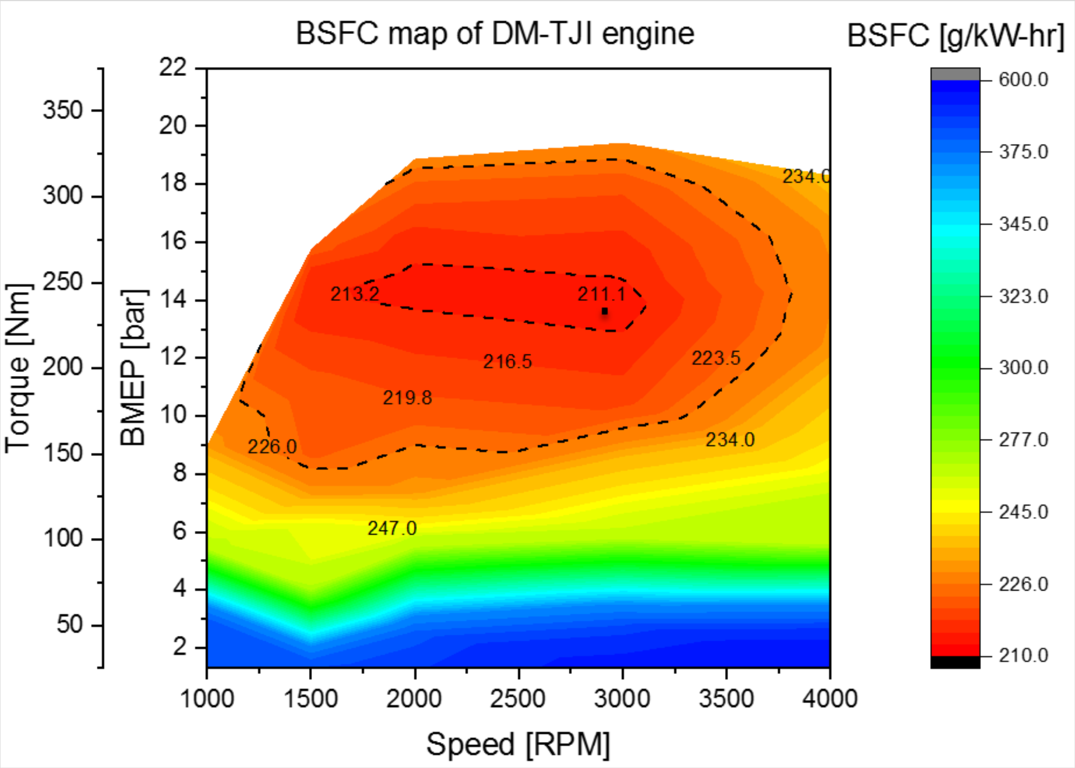

Figure 3.15 *BSFC map of DM-TJI engine with high EGR dilution*

The DM-TJI engine map was generated with a compression ratio of 13.3:1. The DM-TJI engine can deliver a peak BMEP of above 18 bar from 2000 rpm to 4000 rpm with a maximum of 19.4 bar at 3000 rpm. A maximum brake thermal efficiency (BTE) of 40.9 % was found at 3000 rpm, and a load of 13.8 bar, as shown in Figure 3.14. The engine could run above 38.5% BTE for a wide engine operating load of 8 – 18 bar. A minimum BSFC of 211.1 g/kW-hr was achieved at 3000 rpm, and 13.8 bar load as shown in Figure 3.15. A wide engine operating where less than 226 g/kW-hr with the engine operating load from 8 – 18 bar. A similar result was reported on 1.5L DI3 passive MAHILE Jet ignition system [45] with a maximum 39.6% BTE and minimum BSFC value of 211 g/kW-hr. The summarized engine map data are shown in the Appendix A.

3.6 Summary and Conclusion

This chapter covers the numerical combustion model development of the DM-TJI engine using GT-Power tools. The model included the intake/exhaust runner, intake/exhaust valves, auxiliary pre-chamber valve with compressed air line, pre-chamber, connecting nozzle, and main chamber. The flow model involves the solution of the Navier-Stokes equations: namely, the equations of continuity, conservation of energy, and momentum are adapted and simplified for implementation in GT-Power. In addition, the model employed a two-zone analysis in the combustion chambers, while the GT-Power WoschniGT heat transfer model was used to simulate heat transfer. A wide range of experimental data was acquired for engine model calibration and validation using a single-cylinder Prototype III DM-TJI metal engine. The data points vary based on engine speed, engine load, EGR inlet percentage, spark timing, and pre-chamber auxiliary inlet air pressure. A TPA model was created that used Wiebe-based predictive combustion. The model was initially tuned to match the engine motoring trace and engine firing trace.

From a range of experimental running points, engine operating points were selected after the test point passed TPA burn rate data consistency checks. These running points were used to create the experimental database to develop a 1D model of the engine in GT-Power. The Wiebe function parameters were estimated experimentally for each of the selected operating conditions, and three different correlations that predict the Wiebe function (CA50, Burn1090, and m) were found from the selected engine operating variables using linear regressions.

Based on the simulation and experimental study carried out, the results demonstrated that:

- The experimental result and the TPA model simulations result are in good agreement; the simulation result achieved a reasonable degree of accuracy of peak cylinder pressure within a percentage of error of 0.42 – 1.2 % for both pre- and main chamber pressure.
- The intake/exhaust experimental runner pressure trace also agrees with the simulation except at the opening of the valve, which shows a pressure fluctuation. However, the average inlet/exhaust pressure values achieved a good degree of accuracy within a percentage error of 0.09 – 0.57 %.
- The effectiveness of the proposed Wiebe-based combustion model was validated by comparing simulated IMEPg values to experimental results. The percent differences were in the range of ±5% for most test ranges except at low load below 6 bar, which is at the limit of ± 6%.
- The in-cylinder main chamber pressure was compared with the experimental result at each crank angle. The model prediction was able to capture the measured in-cylinder pressure within a maximum residual of ± 3 bar.
- The DM-TJI engine in a four-cylinder configuration efficiency and fuel map was employed with boosted and highly diluted conditions. A maximum brake thermal efficiency (BTE)

of 40.9 % and a minimum BSFC of 211.1 g/kW-hr were achieved at 3000 rpm and a load of 13.8 bar.

A drive cycle analysis is employed to explore further fuel consumption in the coming chapters. In order to improve the current powertrains, hybrid architectures combining electrical components and high-efficient internal combustion engines (DM-TJI engine) were demonstrated for better fuel consumption and CO2 reduction.

Chapter 4: Vehicle Powertrain and Drive Cycle Analysis

4.1 Introduction

A vehicle's power output (from Engine/Motor) are controlled by a transmission system and a driveline to deliver the tractive effort to the wheels with the help of additional accessories. The powertrain architecture is classified into conventional (traditional), mild hybrid, full hybrid, and electric vehicles based on the power source. All these components are referred to as the powertrain system and are controlled by the driver.

The selection, design, and optimization of the powertrain architecture for vehicle development is critical. Identifying the best architecture and the required components in the development stage is challenging. It involves and depends on multiple factors. The number of parameters in hybrid electric vehicles increases compared to the traditional powertrains due to the addition of electric motors, battery packages, and control systems, apart from the conventional hardware such as the internal combustion engine, transmission, and differential. Hybrid electric vehicles interact with several energy management strategies and further complicate selecting an appropriate architecture. The availability of different energy management options and parameters suggests that advanced investigation needs to be performed before choosing the powertrain.

Driving cycle analysis is an essential component for determining the outcome of different powertrain technologies. It plays a fundamental role in vehicle design since the driving cycle outcome affects the fuel consumption, engine emission, and total vehicle performance. The analysis can highlight the benefits obtained from the examined powertrain, as it translates fuel map data into fuel consumption in miles per gallon and overall thermal efficiencies.

4.2 Vehicle Simulation Model

The commercial software GT-Suite of Gamma Technologies® was used for the powertrain and drive cycle analysis. GT-Suite, which includes the GT-Power Engine Library, is the leading engine and vehicle simulation tool used by engine makers and suppliers. It is suitable for analyzing a wide range of vehicle and engine performance [79]. The GT-Suite package allows the entire vehicle model to simulate standard driveline components to construct the various driveline layouts. The models include a gearbox, tires, axles, and couplings.

GT-Suite driveline models are built by combinations of 1-D inertias (modeled in components) connected with either rigid/kinematic connections or slipping/compliant connections. In addition, the GT-Suite also has the necessary devices to build the hybrid powertrain, such as different electric motors, battery modules, and controllers. Moreover, the software allows the incorporation of driving cycles with their respective load, acceleration profile, and performance in different environmental conditions. In this way, the experimental engine maps are used as inputs for the simulation.

4.2.1 Engine to Drive Cycle Framework

The comprehensive engine to drive-cycle framework developed comprises three key components.

- Full engine system models and procedures for the generation of engine performance and fuel consumption maps.
- Experimental heat release analysis tool, which was created by coupling an in-house heat release analysis program to an engine cycle simulation, and which can be used for model calibration and validation when experimental data are available.
- Integrated vehicle modelling and drive cycle simulation for fuel economy assessment.

The overall drive cycle framework is illustrated in the flow chart outline shown in Figure 4.1. Up to the steady-state engine maps stage covered in the previous chapters. This chapter covers the rest of the frameworks.

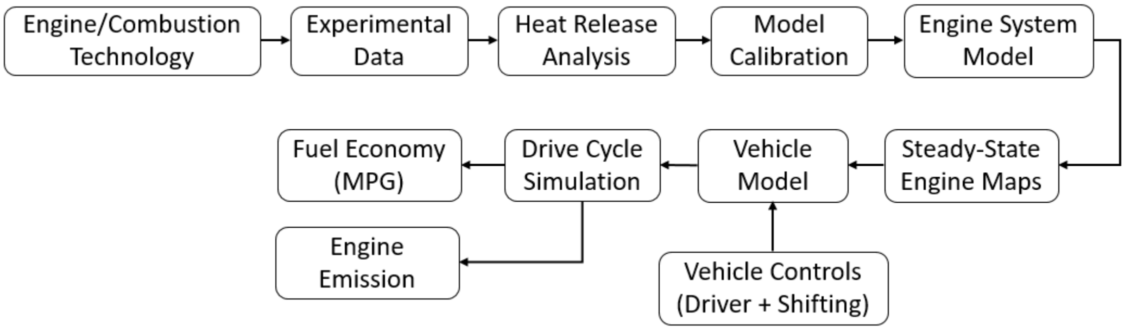

Figure 4.1 *Flow chart outline of drive cycle analysis frame work*

4.2.2 Data Needed to Build a Vehicle Model

The following modeling template and list of information are needed to build a basic vehicle model on GT-Suite.

Engine: used to characterize an internal combustion engine through a map-based engine model that describes engine performance (power output and friction), fuel consumption, heat rejection, emissions, and other characteristics. The engine model is based around a steady-state fuel map and load map covering all engine speed and load conditions. The data required are:

- Engine geometrical data and displacement.
- Effective rotational inertia.
- Idle speed.
- Mechanical performance map (map of brake power, torque, or MEP as a function of engine RPM and normalized load).
- Fuel consumption map.

Clutch: used to model the action of a dry (friction) clutch between two 1-D rotational mechanical assemblies. The required data is maximum static clutch torque (which can be approximated by engine torque).

Torque Converter: used to represent the action of an automotive torque converter in a vehicle/driveline model. The data required is the coefficient of performance table and torque ratio table.

Transmission: used to model the torque amplification and speed reduction effect of discrete transmissions in vehicle models. This model shows the two sides (input and output) of transmission as lumped inertias kinematically linked by a transmission (gear) ratio. The gear ratio and input/output side inertias, and the transmission efficiency and friction torque are specified individually for each discrete gear. The data required is transmission gear ratio, gear efficiency, and friction torque.

Vehicle: used to calculate the longitudinal motion of a vehicle and the expected loads on each axle. The vehicle's acceleration is calculated from the longitudinal force balance: acceleration is integrated to calculate vehicle speed and displacement. The longitudinal force balance includes, on an instantaneous basis, the effect of tractive forces applied to the tires, tire rolling resistance, aerodynamic drag, road grade, and curvature, as well as wind velocity and direction. The data required is vehicle mass (including drivetrain), frontal area, and drag coefficient.

Furthermore, additional templates are required to model the electrical components on HEVs powertrain, including the above template. Battery template and motor characteristics, and control strategy operating points, are included in the model.

4.2.3 Basic Driveline Model Equations of Motion

In Dynamic Analysis, the differential equations of motion for the driveline components are integrated in time to calculate transient speeds and torques in the system. The engine torque is a function of the engine operating condition and is applied at the flywheel. It is computed by a lookup in the map-based engine model as previously defined. The model allows the engine mechanical (brake) output specified as a constant or transient brake mean effective pressure (BMEP) or accelerator position. The vehicle environment characteristics and resistance to motion (i.e., the aerodynamic, rolling resistance, and gravity road load) are a function of the vehicle speed and driveline applied as a linear retarding force on the vehicle [80].

Equations of engine motion in the dynamic analysis are written as follows:

$$\tau_{eng} = (I_{eng})\frac{d\omega_{eng}}{dt} \tag{4.1}$$

Where: τ_{eng}= Engine (brake) Torque

I_{eng} = Engine Moment of Inertia

ω_{eng}= Engine Speed

The total required torque to move the vehicle defined by Equation 4.2. Driveline Equation for speed of vehicle side of clutch or torque converter is given by:

$$\begin{aligned}\tau_{drv,v} = {} & \left[I_{trans1} + \frac{I_{trans2}}{R_t^2} + \frac{I_{dsh}}{R_t^2} + \frac{I_{axl}}{R_t^2 R_d^2} + \frac{M_{veh} r_{whl}^2}{R_t^2 R_d^2}\right]\frac{d\omega_{drv}}{dt} \\ & - \left[\frac{I_{trans2}}{R_t^3} + \frac{I_{dsh}}{R_t^3} + \frac{I_{axl}}{R_t^3 R_d^2} + \frac{M_{veh} r_{whl}^2}{R_t^3 R_d^2}\right]\omega_{drv}\frac{dR_t}{dt} \\ & + \left[\frac{F_{aer} + F_{rol} + F_{grd}}{R_d R_t}\right] r_{whl}\end{aligned} \tag{4.2}$$

Where: $\tau_{drv,v}$= Vehicle side (output) torque of clutch or torque converter

I_{trans1}= Input side Transmission Moment of Inertia

I_{trans2}= Output side Transmission Moment of Inertia

R_t= Transmission Ratio

I_{dsh}= Driveshaft Inertia

I_{axl}= Axle Moment of Inertia including wheels

R_d= Final Drive Ratio

M_{veh}= Vehicle Mass

r_{whl}= Wheel Radius

ω_{drv}= Driveline speed on vehicle side of clutch or torque converter

F_{aer}= Aerodynamic Force on Vehicle

F_{rol}= Rolling Resistance Force on Vehicle

F_{grd}= Grade (Gravity) Force on Vehicle

The first term in the bracket of equation 4.2, represents the torque required to accelerate the effective inertia, evaluated at the clutch or torque converter output, of the entire drivetrain. The second term of the equation represents the load induced by a transient gear ratio. The third term of the equation represents the external forces of the vehicle ambient and the road. These forces are converted to torque by the tire radius and reduced through the gear ratios for evaluation at the clutch/torque converter output.

The mild-hybrid powertrain system is mathematically described in the following equation:

$$P_{eng\_on} = T_{coupler}.\omega_{eng}\ , \qquad P_{regen} = (P_{tractive}.\beta + T_{rest}.\omega_{eng}).\epsilon \qquad 4.3$$

$$T_{coupler} = T_{eng} + T_{motor}.r.\varepsilon\ , \qquad T_{rest} = T_f + T_{inertia},\ \ T_{inertia} = I\,\frac{d\omega_{eng}}{dt} \qquad 4.4$$

Where, P_{eng_on} the power during engine on state, $T_{coupler}$ torque delivered to the transmission, ω_{eng} engine speed, P_{regen} the regenerative power during deceleration and engine-off state, $P_{tractive}$ the negative portion of vehicle tractive power, β regenerative brake energy recuperation efficiency, T_{rest} engine resistance torque, ϵ electric generator efficiency, T_{eng} engine torque, T_{motor} electrical motor torque, r belt-pulley ratios, ε belt torque transmission efficiency, and T_f engine friction torque. However, for a parallel hybrid powertrain system, the torque delivered to the transmission (equation 4.4) is modified. The belt-pulley connection was replaced with a clutch shaft connection. The clutch allows independent operation of the electric motor by allowing completely decouple from the engine and transmission.

$$T_{coupler} = T_{eng} + T_{motor} \tag{4.5}$$

4.3 Conventional, Mild and Parallel Hybrid Powertrain Models

4.3.1 Conventional Powertrain Model

The basic GT-Suite powertrain model consists of three layers; systems, components, and functions. The system (e.g., engine) consists of components (e.g., fuel consumption), representing individual physical entities that make up the entire system when combined. Functions are mathematical equations that describe or correlate the systems and components of the model. A basic conventional powertrain model is expected to have Engine, Transmission, Driver, Engine control, and Shift control. The power line starts from ICE, the transmission is coupled with the engine through a clutch, and the transmission's output is connected to the differential that propels the wheels. The vehicle model incorporates a sub-model of the brakes, tires, and axles behavior. Figure 4.2 show a scheme of conventional powertrain model developed in GT-Suite.

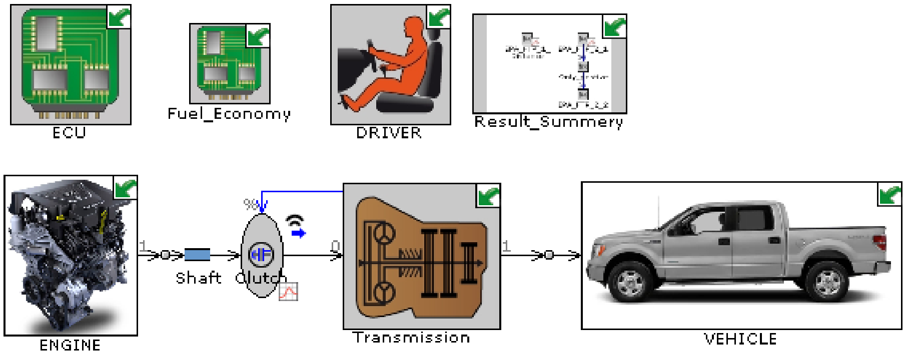

Figure 4.2 *Conventional powertrain model developed in GT-Suite*

4.3.2 Hybrid Powertrain Models

A fundamental element in hybrid powertrains is the control system. This starts from battery power limits and battery state of charge and define the operating condition of the driving cycle. On the hybrid powertrain, three primary drive states are involved; pure electric mode (only electrical motor), conventional powertrain (only engine), and dual propulsion mode (combined electrical motor and engine). The control system determines which powertrain can propel the vehicle in different modes by changing the states of the coupling devices. The hybrid control system is mainly divided into two levels: Vehicle supervisor control (VSC) and local level or component controller. The VSC primarily manages all the vehicle signals to calculate and control the engine demand torque, the required torque from the motor, and the electrical motor activation timing. It also contains and gives commands to low-level controllers, which include the engine controller unit (ECU), the battery management system (BMS), the transmission controller unit (TCU), and the regenerative brake controller.

A set of algorithms defines the power management of VSC to achieve a predefined objective that will enable the vehicle to operate in a manner that will improve the state of charge, fuel economy, engine performance, and vehicle emissions. In general, the VSC control algorithm is divided into rule-based controllers and optimization-based controllers [81]. Rule-based methods are formulated using human expertise, operation boundaries, and safety considerations. The control law is defined as a set of "if-then" rules to determine the control action. The main goal of the rule-based control strategy is to operate the vehicle at its highest efficiency point by running the engine and the electric motor at their most efficient points while satisfying the demanded vehicle tractive power requirements. The main advantage of these methods is the low computational requirements; therefore, they are widely used in several commercial vehicles [82]. Optimization-based advanced controllers were seen to hold high potential; the system optimization takes place as a result of system learning and adapting to the condition within a framework of rules or constraints. However, the impact of this method so far has been mainly within academic circles [83]. Therefore rule-based methods are still more prevalent due to their effectiveness in commercial cars. These are adapted for modeling the power management of VSC. Figure 4.3 shows the scheme of hybrid powertrain models developed in GT-Suite.

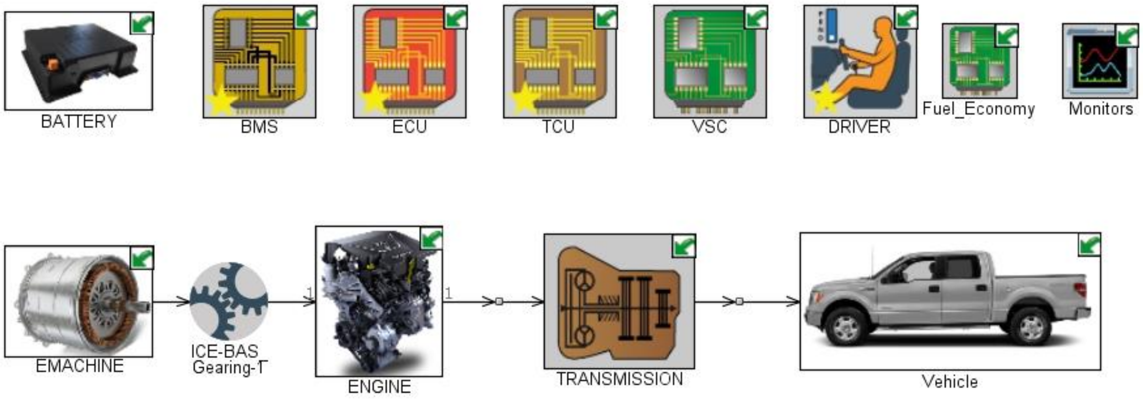

Figure 4.3 *Hybrid powertrain models developed in GT-Suite*

4.3.3 Hybrid Powertrain Rule-Based Control

The rule-based program is prepared to provide the primary function of the hybrid powertrain. The functions include vehicle start-stop, regenerative brake, battery charging, and power assist. The main decision factors in determining the hybrid powertrain function are battery state of charge and drive torque demand. The driving state of a vehicle is grouped into three phases: vehicle start from the stop (vehicle speed zero and engine off), vehicle on driving state, and vehicle decelerating or braking.

Initially, when the vehicle is at a stop state, depending on the battery state of charge (SOC), one of the following states is possible:

- If the engine is off, the electric motor provides torque to start the engine.
- If the driver pedal is position at on state, the electric motor provides the initial driving torque.
- If the engine is in an idle state, the battery charges.

When the vehicle is moving, and the drive torque request is positive, one of the following states is possible:

- The electrical motor provides the initial driving torque up to the engine speed to reach a high-efficiency state.
- The engine provides driving torque and electric motor power assist in which the demand drive torque is more than that the engine can provide.
- The driving torque provided by the engine, and the battery stays charging.
- The engine provides the drive torque without charging the battery.

When the vehicle is in decelerating or braking state (the vehicle speed is greater than zero, but the vehicle driving demand is negative), one of the following states is possible:

- Conventional braking, in which the friction brakes are activated because energy recovery is not required.
- In regenerative braking mode, the electric motor is operated to produce a braking torque, and part of the kinetic energy of the vehicle mass is converted into electric power and stored in the batteries.
- In mixed braking, when the electrical motor is not capable of braking the vehicle, both the electric motor and the conventional friction brakes work together to deliver braking power to decrease the vehicle speed.

Rule-based VSC collaborates with low-level controls and the internal feedback information (main signals of the components) to change the powertrain state according to the primary programming. Some of the functions of low-level controls are:

Battery Management System (BMS): Based on the difference between the current state of charge and the state of charge target, it calculates the power available in the system and the maximum discharge and charge rates. Suppose enough energy is available on the battery. In that case, power is discharged from the battery to provide the demanded electric motor torque when the pedal acceleration is greater than a defined pedal acceleration or engine load and the vehicle tractive power is greater than zero. When the battery state of charge is less than the target, the battery starts to recharge until it reaches the state of charge target. A two-dimensional lookup tables as a functions of state of charge and engine speed stored as a charging threshold values.

Engine Control Unit (ECU): The objective is to simulate engine control functions such as idling and fuel cut for various conditions. Engine speed and accelerator pedal position are used as input signals, and the controller decides the engine accelerator position and engine fueling based on the vehicle traction demand.

Transmission controller (TCU): It represents an automatic transmission control logic for gear selection. Speed, accelerator position, initial gear number, and shift indicator are used to determine the desired transmission gear number.

4.4 Battery Pack Model

Battery running time and Voltage-current performance can be predicted by the battery model used to design energy-aware circuits and systems. Many battery models have been put forward for vehicle power management control and BMS development. With many different models being used, the most common models are electrochemical, behavioral, and equivalent circuit models [84].

Behavioral models are empirical and utilize various functions to model battery dynamics, where inputs are passed through a network of previously trained weights to simulate an output. It can be applied to a nonlinear system to estimate an accurate output depending on the quality of the training data. However, it is not very robust between different cell chemistries or boundary conditions, as retraining is required [85,86]. Hence this model is not applicable in EV application due to the real-time demands of BMS.

Behavioral models are empirical and utilize various functions to model battery dynamics, where inputs pass through a network of previously trained weights to simulate an output. This means that it can be applied to a nonlinear system and estimate an accurate output, depending on the quality of the training data, however, it is not very robust between different cell chemistries or different boundary conditions, as retraining is then required [84,85]

The most common battery modeling method is the Equivalent Circuit Models (ECM), which uses RC circuit elements such as resistors, capacitors, and an ideal voltage source to form a circuit network and simulate the battery behavior. Compared to electrochemical models, the simulation time and computational power needed to simulate different battery steady or transient performances are lower. The model outputs can show the main vital battery characteristics and information of internal resistance, voltage performance, state of charge, and battery temperature [87]. The ECM method is helpful for BMS development, which serves as a part of vehicle level simulation studies for battery pack sizing and range estimation calculations. This aspect of the ECM model makes it preferable for battery modeling.

The developed ECM model should consider the appropriate parameters of different battery components. The parameters presented on the model are in the form of lookup tables, which would be in function of current, SOC, and temperature. A preliminary simulation can be performed with the validation profile to verify the model. Figure 4.4 shows a schematic representation of theoretical steps taken to achieve a complete development of a model, simulation, and validation.

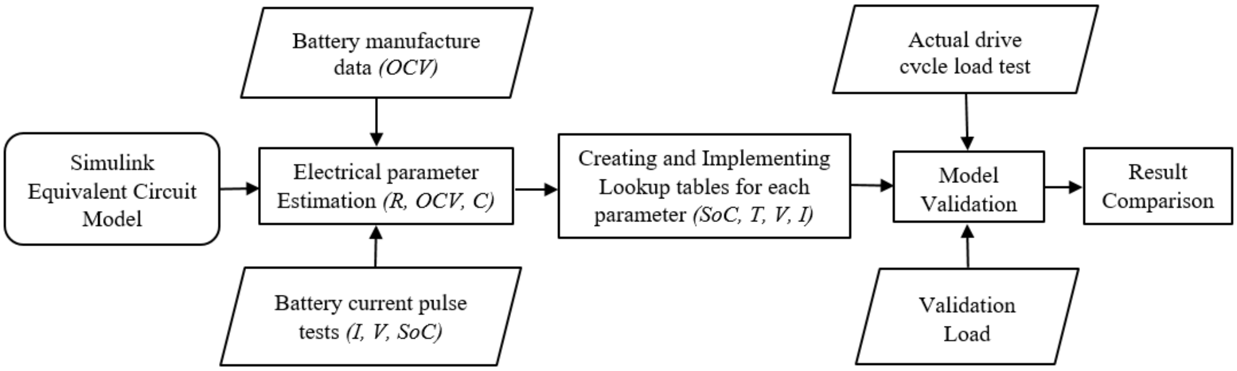

***Figure 4.4** Schematic representation of equivalent circuit battery modeling*

4.4.1 Equivalent Circuit battery model

Various equivalent circuit battery models were studied. Some of the models are Rint, RC, Thevenin, and Dual polarization [87,88].

4.4.1.1 Rint Model

The Rint model comprises an ideal voltage source Voc to represent the battery cell's open-circuit voltage (OCV) and a resistor in series Rint to describe the internal ohmic losses. The basic Rint model describes a linear behavior of a battery without knowing any information regarding the inner composition and processes taking place in the battery. However, this method does not capture the dynamics during transient states, and the current can fluctuate dramatically. This model would not be suitable for HEV applications [84,87].

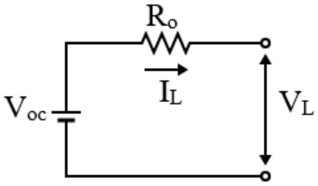

Figure 4.5 *Schematic diagram of the Rint battery model*

4.4.1.2 The RC Model

The RC model consists of two capacitors (C_c, C_b) and three resistors (R_t, R_e, R_c). The capacitor represents the surface effects of a battery and the capability of a battery's store charge (state of charge). Combining a capacitor (C_c) with a resistor (R_c) creates the RC circuit and calculates the amount of current the battery can deliver. The RC model is classified as a semi-empirical model [87], considers common physical aspects of a battery, and at the same time, considers the battery as a black box.

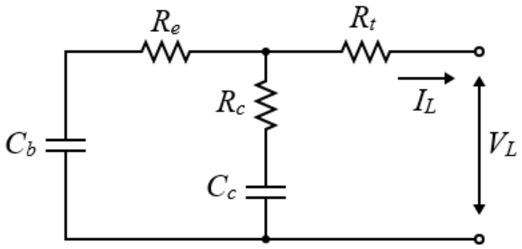

Figure 4.6 *Schematic diagram of the RC battery model*

4.4.1.3 The Thevenin Model

The Thevenin model (referred to as the first order battery model) is the expansion of the Rint model consisting of a parallel RC circuit in series with resistance or Rint model, describing the dynamic characteristics of the battery [87]. The model is composed of internal resistances including the ohmic resistance R_o and the polarization resistance R_{Th}. The equivalent capacitance C_{Th} connected with R_{Th} in parallel describes the transient response during charging and discharging. The Thevenin model assumes that the OCV has a constant relationship with the state of charge, and the ohmic resistance does not change during charging and discharging [88].

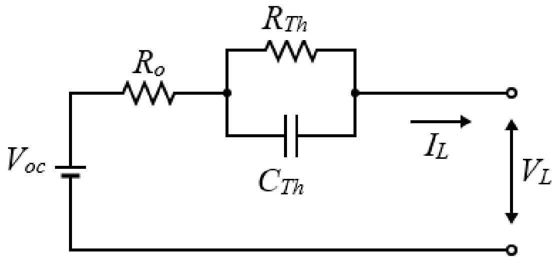

Figure 4.7 *Schematic diagram of the Thevenin battery model*

4.4.1.4 Dual-polarization model

The dual-polarization (referred as a second-order equivalent circuit) model is similar to the Thevenin model, with an additional RC circuit attached in series with the first RC circuit. The dual-polarization model contains the ohmic polarization, concentration polarization (chemical behavior), and the activation polarization related to the electrochemical reactions at the electrode surface of a battery. The model comprises six components as shown in Figure 4.8: open-circuit battery voltage V_{oc}, internal resistance contains the ohmic resistance and the polarization resistance (polarization resistance has two components, effective resistance characterizing activation and effective resistance characterizing concentration), and two effective capacitances parameters (which are used to characterize the transient response during the transfer of power to or from the battery and to describe the electrochemical polarization and the concentration polarization separately) [89,90].

Comparing the above three modeling methods, the dual polarization model has the best simulation accuracy [87]; using two RC time constants (instead of one or three) is the best tradeoff between accuracy and complexity because two RC time constants keep errors to within one mV [91]. This study modeled a lithium-ion battery cell using a dual-polarization equivalent circuit cell model, as shown in Figure 4.8. The model results validate with published battery experimental test results [18,92–94].

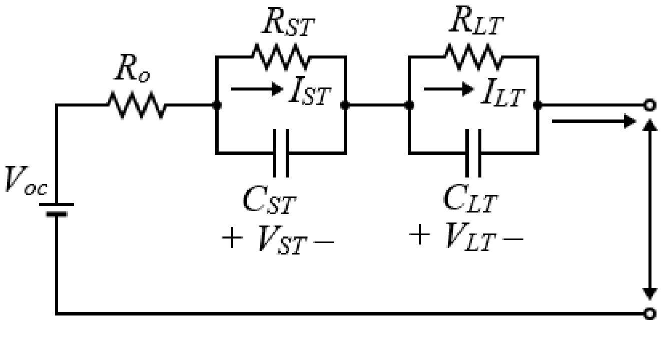

***Figure 4.8** Schematic diagram of the dual-polarization model*

4.4.2 Equivalent Circuit Cell Numerical Model

The electrical equivalent circuit cell model consists of a series resistor R_o and two RC parallel networks composed of R_{ST}, C_{ST}, R_{LT}, and C_{LT}, as shown in Figure 4.8. Series resistor R_o is responsible for the instantaneous voltage drop of the step response. R_{ST} and C_{ST} are resistances and capacitances of the electro-magnetic short-time double layer effects, respectively. R_{LT} and C_{LT} are resistances and capacitances of the electro-chemical and long-time mass transport effects, respectively. V_{oc} is the open-circuit voltage of a battery cell, and I_L is the cell load current. I_{ST} and I_{LT} are the outflow current of the two RC circuits, V_{ST} and V_{LT} are the voltage across the two RC circuits.

The electrical behavior of the battery cell terminal voltage, V_L calculated using a typical RC circuit as shown in equation 4.6.

$$V_L = V_{oc} - I_L R_o - V_{ST} - V_{LT} \tag{4.6}$$

$$\dot{V}_{ST} = \left(\frac{I_L}{C_{ST}}\right) - \left(\frac{V_{ST}}{R_{ST}C_{ST}}\right) \quad , \quad \dot{V}_{LT} = \left(\frac{I_L}{C_{LT}}\right) - \left(\frac{V_{LT}}{R_{LT}C_{LT}}\right) \tag{4.7}$$

$$I_{ST} = V_{ST} / R_{ST} \quad , \quad I_{LT} = V_{LT} / R_{LT} \tag{4.8}$$

From equations 4.7 and 4.8, we can write

$$V_{ST} = \int ((I_L - I_{ST}) / C_{ST}) dt \ , \quad V_{LT} = \int ((I_L - I_{LT}) / C_{LT}) dt \tag{4.9}$$

After substituting equation 4.9 into equation 4.6, battery cell terminal voltage, V_L is

$$V_L = V_{oc} - I_L R_o - \int ((I_L - I_{ST}) / C_{ST}) dt - \int ((I_L - I_{LT}) / C_{LT}) dt \tag{4.10}$$

Total battery pack voltage, V_{Batt}, calculated by

$$V_{Batt} = V_L (N_{series} / N_{parallel}) \qquad 4.11$$

Where:

V_{Batt} = voltage across the terminals of the battery (V)
V_L = battery cell terminal voltage (V)
N_{series} = number of cells in series connection
$N_{parallel}$ = number of cells in parallel connection
V_{oc} = open circuit voltage (V)
I_L = battery cell load current (A)
R_o = the ohmic resistance of a cell (Ω)
I_{ST} = current across the first RC circuit (A)
I_{LT} = current across the second RC circuit (A)
C_{ST} = short-time capacitances (F)
C_{ST} = long-time capacitances (F)
R_{ST} = short-time resistance (Ω)
R_{LT} = long-time resistance (Ω)

Matlab/Simulink blocks are used to create an integrated model with easily changeable parameters for estimating the battery parameters based on equations 4.10 and 4.11. In addition, the Simulink method is valid for any similar battery model, which makes Simulink a great tool in parameter estimation and model modification.

The values of current, resistance, and capacitances are included in the model using two-dimensional look-up tables.

4.4.3 Battery Thermal Model

Battery cell internal ohmic resistance and charge transfer resistance can generate heat during the charge or discharge cycle of operation. The performance of batteries is greatly affected by the operating temperature. Overheating the battery cells may undesirably affect the operation, efficiency, life, and life cycle cost of the battery. A simple but efficient lumped capacitance thermal model is implemented in the hybrid model to estimate the battery pack temperature [93].

The battery pack temperature was calculated by using the energy balance between battery heat generation (Q_{gen}) in the core of the battery (due to electrochemical reactions and resistive heating) and heat loss (battery cooling) from the battery by conduction and convection (Q_{loss}).

The battery heat generation calculated by (Q_{gen}):

$$Q_{gen} = I_L^2 R_{Batt} + (1-\eta_C) I_L V_{Batt} \tag{4.12}$$

Where:

R_{Batt} = battery pack resistance (Ω)
η_C = Charge efficiency

The battery pack resistance obtained by

$$R_{Batt} = [R_o + (R_{ST} \frac{I_{ST}}{I_L}) + (R_{LT} \frac{I_{LT}}{I_L})](\frac{N_{series}}{N_{parall}}) \tag{4.13}$$

The battery heat loss is calculated by (battery cooling)

$$Q_{loss} = (T_{Batt} - T_{coolant})(hA + kt) \tag{4.14}$$

Where:

T_{Batt} = battery temperature (C^o)

$T_{coolant}$ = inlet coolant temperature of the battery pack (C^o)

h = convection coefficient ($W / \left(m^2 K\right)$)

A = convection heat transfer surface area of the battery (m^2)

k = battery conduction coefficient ($W/\left(mK\right)$)

t = conduction heat transfer thickness of the battery (m)

The battery pack temperature during the battery use, T_{Batt}, is calculated by using the thermal mass of the battery pack and the method of cooling as follow.

$$T_{Batt} = \int_0^t \frac{(Q_{gen} - Q_{cooling})}{m_{Batt} C_{p,Batt}} dt + T_o \tag{4.15}$$

Where:

m_{Batt} = mass of the battery pack (kg)

$C_{p,Batt}$ = battery specific heat capacity ($J/(kg.C^o)$)

T_o = initial pack temperature (C^o)

Equations 4.15 is solved in the Matlab/Simulink incorporated with battery pack voltage.

4.5 Battery Pack Model Validation

Two different battery pack size models were simulated on a co-simulation of GT-Suite via Mathworks (Natick, MA) MATLAB Simulink to validate the test data result. Co-simulation enabled the combined advantages of GT-Power controllers and Simulink capability to offer a flexible and robust control architecture. The complete Simulink model is illustrated in Figure 4.9. The code was compiled as a dynamic link library file (.dll extension) and input in the GT-Power model via the SimulinkHarness, as shown in Figure 4.10. The first battery pack simulated on the model is the MHEV battery pack of 0.4 kWh, 48V, 8 Ah with 14 series connections using the data published on [92] ; the data contain detailed test results of the EPA National Vehicle and Fuel Emissions Laboratory (NVFEL). The second battery pack simulated on the model is 0.5 kWh, 115

V, 4.4 Ah with 32 series connections. The data was extracted from Argonne National Laboratory (ANL) Downloadable Dynamometer Database [95].

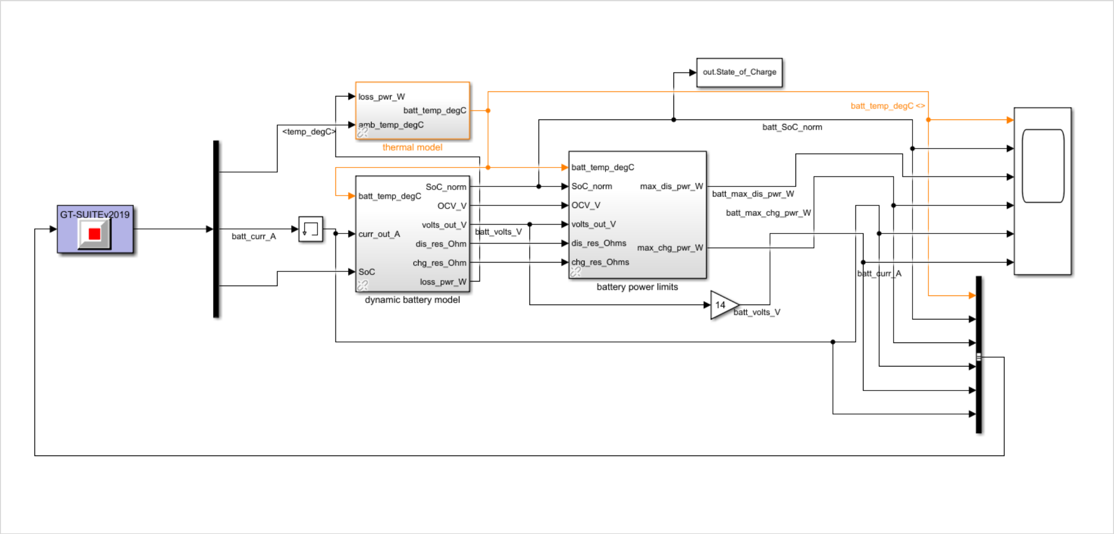

__Figure 4.9__ Co-simulation of GT-Suite and MATLAB/Simulink for battery pack model

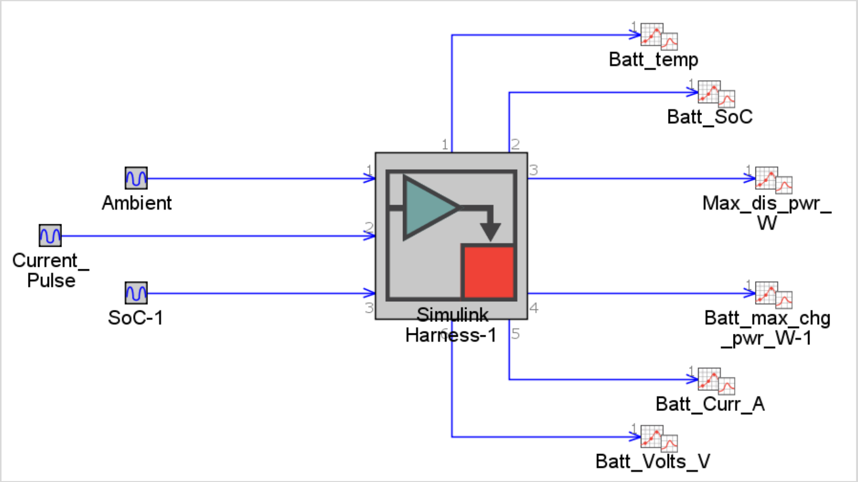

__Figure 4.10__ SimulinkHarness object in GT-Power.

For both battery packs, a look-up table that includes a power limits map, open circuit voltage map, resistance map, capacitance map, short-term and long-term resistance map was prepared based on the charge and discharge of the battery. The maps were tabulated as function of SOC, battery current, and cell temperature on the model. The look-up table data were obtained from public information of the cell manufacturers and published battery test data.

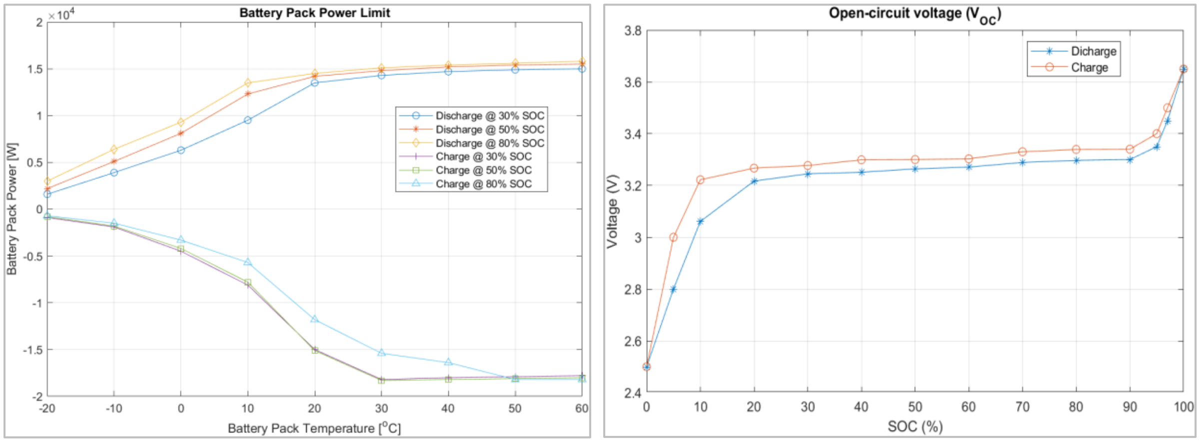

Figure 4.11 *Power limits map and open-circuit voltage (V_{OC}) of lithium-ion battery [92].*

The ohmic resistance of the model battery at the specified SOC and temperature was simulated and compared with the experimental result, as shown in Figure 4.12 for the 48V battery pack. The comparison was made using 10 second discharging and charging pulse currents of 200 A. The root-mean-squared (RMS) charging voltage values of the tested and simulated battery are 46.93 V and 47.25 V, respectively, and the RMS discharging voltage values of the tested and simulated battery are 45.05 V and 44.81 V, respectively. The difference between tested and simulated RMS is within 0.7% for both charging and discharging cases.

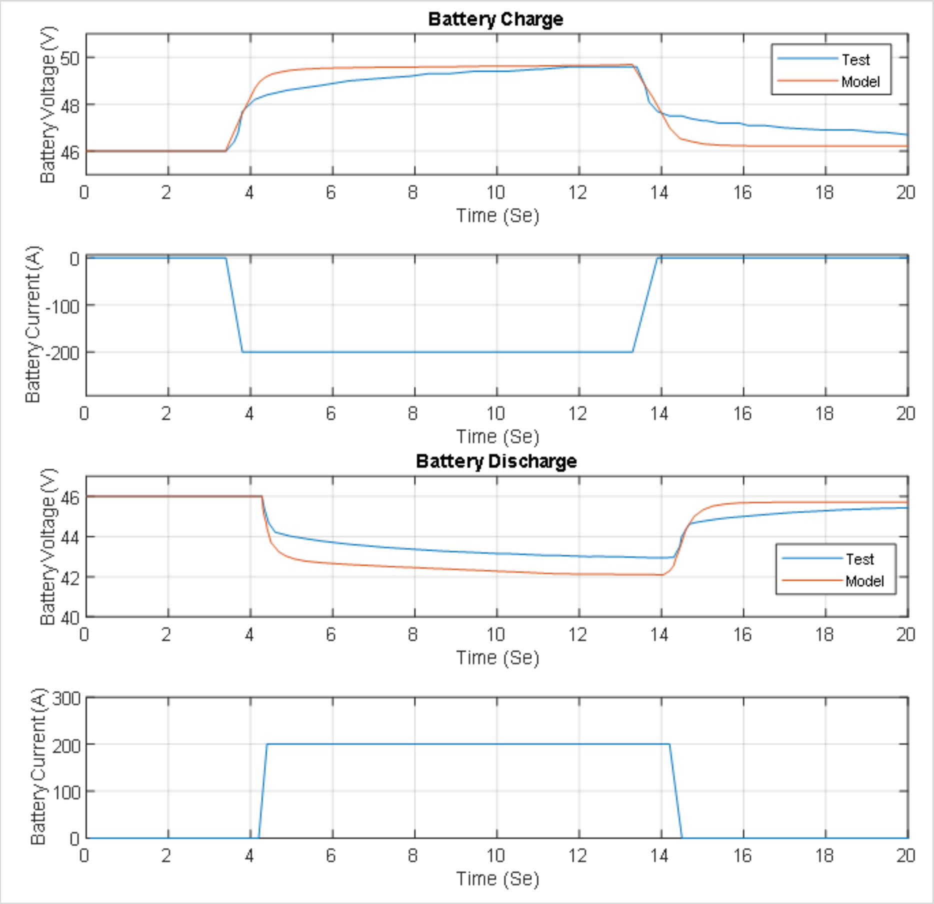

***Figure 4.12** Battery pack charging and discharging pulse test and simulation*

Hardware-in-the-loop (HIL) measured battery demand on the Urban dynamometer driving schedule (UDDS) drive cycle was compared with the modeled battery pack result, as shown in Figure 4.13 for the 48 V battery pack. The measured battery current RMS value over the UDDS drive cycle was 47.44A, and the simulated value was 47.53A. The voltage RMS for the measured and simulated model were 46.01 V and 46.28 V respectively, the difference is within 0.58%. The measured battery current RMS value over the UDDS drive cycle was 47.44A, and the simulated value was 47.53A.

The voltage RMS for the measured and simulated model was 46.01 V and 46.28 V respectively, the difference is within 0.58%. The battery terminal power RMS for measured was 2.18 kW, and the simulated model was 2.2 kW, the difference within 1.06%. The maximum SOC difference between measured and simulated values was 0.01. The summary of the comparison result is shown in Table 4.1.

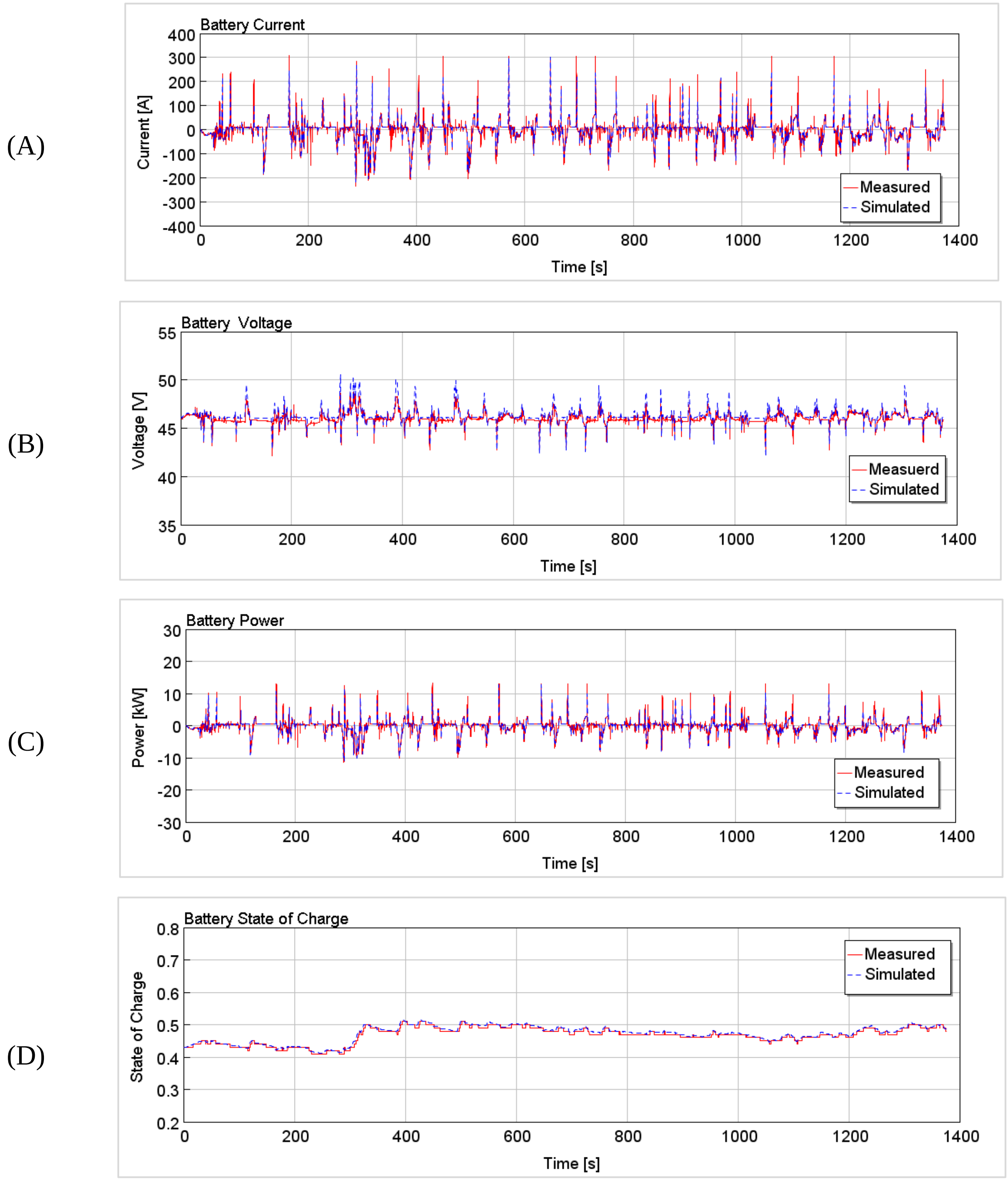

Figure 4.13 *48 V battery pack measured and simulated result comparison (a) Battery current (b) Battery Voltage (c) Battery terminal power (d) Battery state of charge*

Table 4.1 *48 V battery pack measured and simulated result comparison*

Battery Demand	Measured RMS	Simulated RMS	RMS Difference	Percentage Difference
Battery Voltage (V)	46.01	46.28	0.27	0.58
Current (A)	47.44	47.53	0.09	0.17
Battery terminal power (kW)	2.18	2.2	0.02	1.06

The same comparison is made for the 115 V battery pack, the data was collected from Malibu Eco MHEV chassis dynamometer test [95]. The test report contains the battery pack SOC, temperature, current, and voltage. The OCV of the battery is extracted from the cell voltage at various SOCs. The design optimizer was implemented on the commercial software GT-Suite of Gamma Technologies® battery modeling template to generate the missing data points. Using the 48 V data as the initial point and the measured 115V battery voltage as a target value, the design optimizer runs on the selected battery SOC to generate the missing data points. Measured battery demand over Highway fuel economy test procedure (HWFET) and UDDS drive cycle applied on the battery model to simulate the model's response. The result is compared with the chassis dynamometer test as shown in Figure 4.14 (for HWFET drive cycle), and the summary of the comparison for both drive cycles is presented in Table 4.2.

The modeled 115 V battery pack power was in good agreement with the measured chassis dynamometer test result: measured battery voltage RMS 110.05 V and simulated model 109.6 V over the HWFET cycle (Figure 4.14 B). The maximum SOC difference between the measured and simulated model was within 0.012.

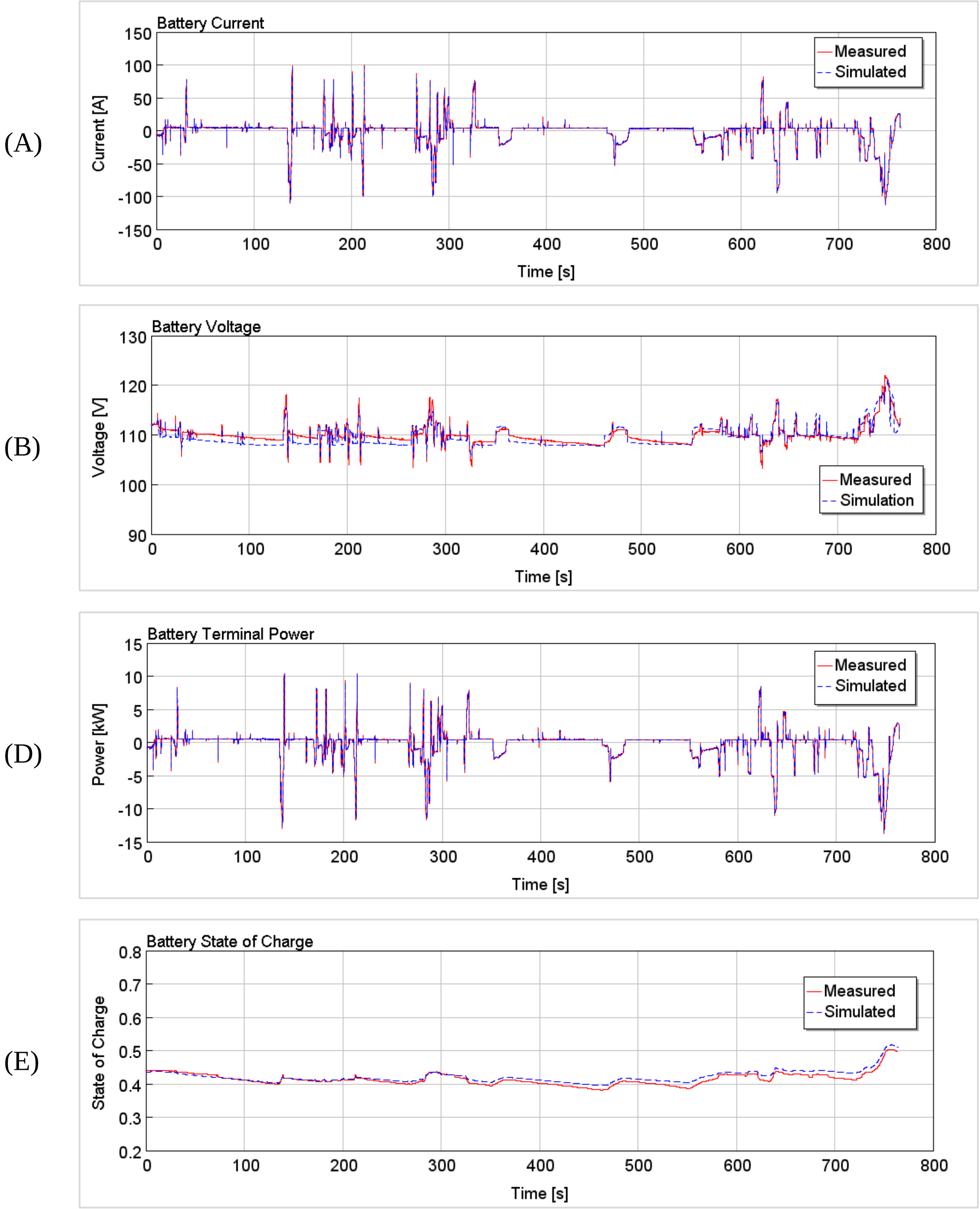

Figure 4.14 *115 V battery pack measured and simulated result over the HIL HWEFT drive cycle (A) Battery Current (B) Battery Voltage (C) Battery terminal power (D) Battery state of charge*

The summary of the measured and test result shown in Table 4.2. It also includes UDDS drive cycle comparison.

Table 4.2 *115 V battery pack measured and simulated result comparison*

Drive Cycle	**Battery Demand**	**Measured RMS**	**Simulated RMS**	**RMS Difference**	**Percentage Difference**
UDDS	Battery Voltage (V)	110.25	112	1.75	1.59
	Current (A)	20.25	20.03	0.22	1.1
	Battery terminal power (kW)	2.22	2.25	0.028	1.26
HWFET	Battery Voltage (V)	110.05	109.62	0.43	0.39
	Current (A)	19.43	19.43	0	0
	Battery terminal power (kW)	2.209	2.203	0.006	0.27

4.6 Powertrain Model Validation

The GT-Suite vehicle model was prepared according to the above explanation for the conventional and mild-hybrid powertrain. The model validates using tested vehicle drive cycle results before using it for the new analysis.

4.6.1 Conventional Powertrain

The conventional powertrain model contains an engine (engine fuel and load map), transition (gear ratio, gear number, and gear change strategy), vehicle body (vehicle mass, passenger and cargo mass, vehicle drag coefficient, axles, and differential geometry), engine control and driver control. The dyno test data and results from EPA’s Advanced Light-Duty Powertrain and Hybrid Analysis (ALPHA) tool were used to calibrate and validate the conventional powertrain GT-Suite model. ALPHA was developed in MATLAB/Simulink and is a physics-based, forward-looking, full vehicle computer simulation capable of analyzing various vehicle types with different powertrain technologies, showing realistic vehicle behavior, and auditing of all internal energy flows in the model. The ALPHA model is built to regenerate the test data produced by chassis dynamometer certification tests [63].

Ford F-150 EcoBoost® 2.7-Liter dyno test data and modeling results from the ALPHA model were used to calibrate and validate the GT-Suite model. The 2.7-Liter EcoBoost® is a turbocharged six-cylinder, direct-injection gasoline engine, dual overhead cam design with variable intake/exhaust cam timing, and twin intercooler turbochargers for on-demand power [96]. The vehicle chassis dynamometer and engine dynamometer benchmark testing were performed at the NVFEL in Ann Arbor, Michigan [97]. Detail vehicle specifications are presented in Table 4.3.

Table 4.3 *2015 Ford F-150 EcoBoost® V6 technical specification*

Engine	2.7L EcoBoost® V6
Compression ratio	10.3:1
Displacement	2.7 L
Bore, Stroke	83.06 mm, 83.06 mm
Aspiration	Twin turbo
Transmission	6R80 Automatic
Gear ratios	4.17, 2.34, 1.52, 1.14, 0.86, 0.69, reverse 3.4, axle ratio 3.73
Max power @ RPM	335 hp @ 5,000 rpm
Max torque @ RPM	400 lb-ft @ 2,750 rpm
Transmission type	SelectShift® 6-speed auto w/progressive range select & tow haul mode
Fuel	Regular unleaded
Vehicle mass	2381.4 kg

Chassis dynamometer testing was conducted at NVFEL over the EPA city and highway drive cycles. Figure 4.15 shows the combined city federal test procedure (FTP-75) and HWFET drive cycles.

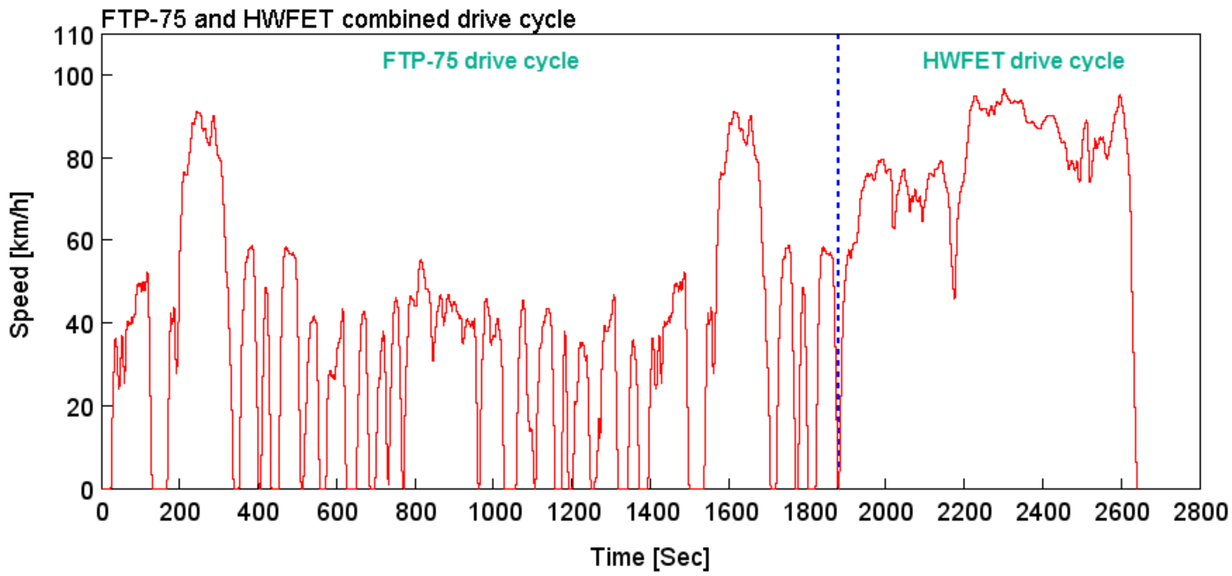

Figure 4.15 *EPA FTP-75 and HWFET combined drive cycle*

The simulated GT-Suite model and the measured chassis dynamometer test result for the engine speed, transmission gear selection, and average gas mileage over the combined drive cycles are shown in Figure 4.16. The model engine speed follows the same data points as the test data through the combined drive cycle; however, unexpected engine speed drops for a fraction second are shown in some data points. The model gear number selection follows the same gear number as the test data. The tested gear number starts from zero, but the model starts from gear number one, which is the only difference shown in drive cycle gear number plot. The calibrated GT-Suite model predicts a similar average gas mileage to the test data. The model results are within two percent of the test result. Test and model result are shown in Table 4.4.

Table 4.4 *Experimental test and model simulation fuel economy result*

Test	**Average Test MPG**	**Average Model MPG**	**Error %**
City	21.28	21.65	1.73
Highway	29.67	29.98	1.04
Combined	24.38	24.76	1.55

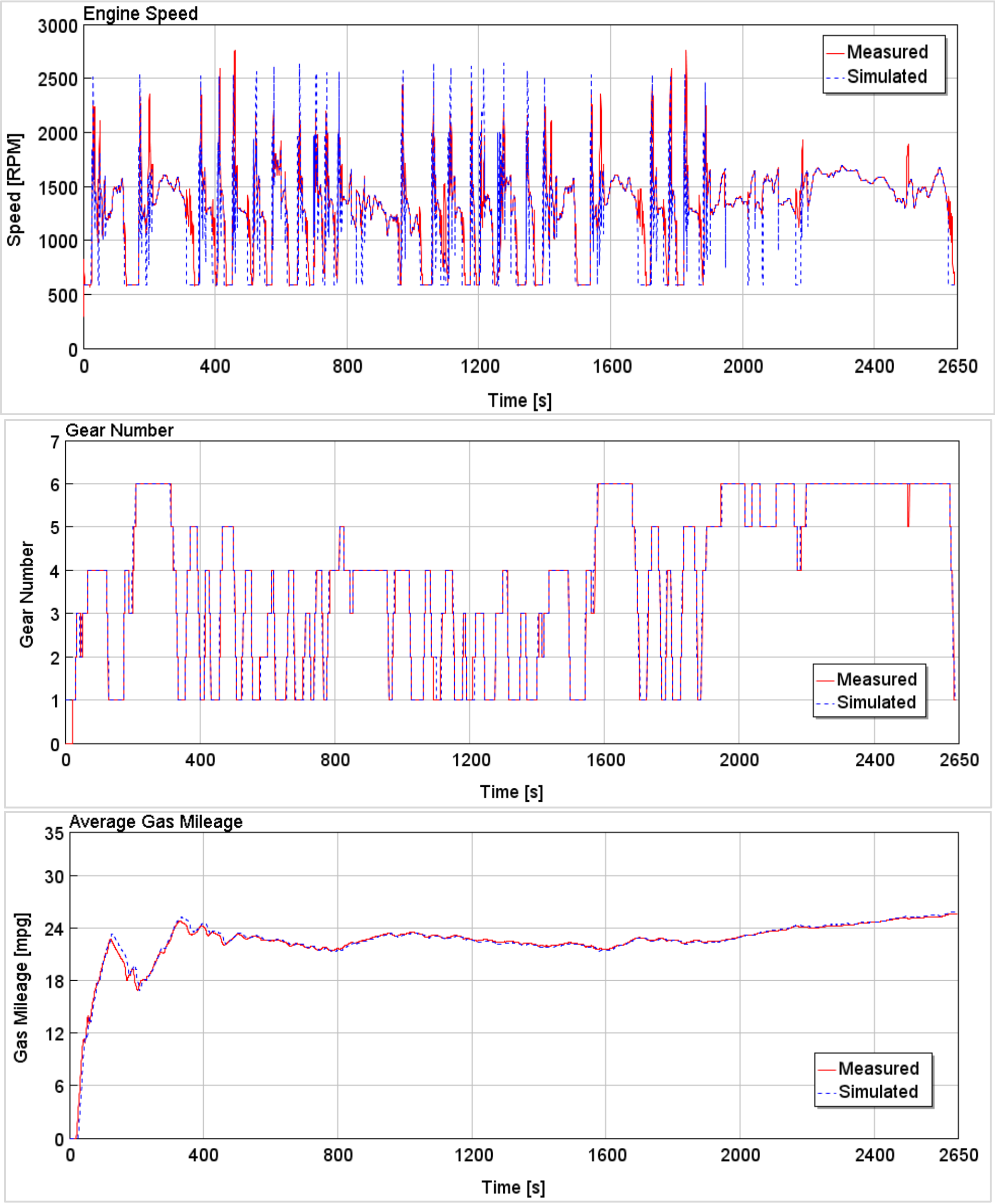

Figure 4.16 *Comparison of NVFEL chassis dynamometer measured data and GT-Suite simulated result on engine speed, transmission gear selection, and average gas mileage over the combined EPA FTP-75 and HWFET drive cycle.*

4.6.2 Mild-hybrid Powertrain

The mild-hybrid powertrain model contains a 12/15 KW electrical motor connected directly to the engine by a belt pulley. The electrical motor data extracted from published paper [18,98]. The available free energy tractive power is harvested by the electric motor and charged to the battery during deceleration. When the vehicle demand for tractive power is less than the battery available discharge power, the battery pack may enable limited electric-only vehicle driving capability at a very low vehicle speed. The belt-pulley connection, inverter, engine friction, and inertia generate energy losses in the system. The model considers the energy loss while powering the vehicle and energy recovering during regenerative braking.

The engine map, fuel map, and drive cycle test result availability of the 2013 GM Chevrolet Malibu Eco makes it preferable to validate the hybrid powertrain model before using it for the new engine and powertrain. The model used a brake thermal efficiency engine map [99], surrogate fuel map [18], and GM 6 T40 6-speed automatic transmission [100] to create the power coupling. The EPA drive cycle test result conducted at ANL was used as a reference for model result comparison [101]. A detail vehicle description presented in Table 4.5.

Table 4.5 *2013 GM Chevrolet Malibu Eco Vehicle Description*

Engine	Ecotec 2.4L I-4 DI w/ eAssist
Gear ratios	4.58, 2.96, 1.91, 1.45, 1.0, 0.75, reverse 2.84, final drive ratio 2.64
Maximum electric generating power	15 kW @ 1570-3180 rpm
Maximum electric motor torque (cranking)	150 Nm
Maximum electric motor torque (electric assist)	107 Nm @ 1,000 rpm
Maximum electric motor power (electric assist)	11.2 kW @ 1,000-2,200 rpm
Lithium-ion battery	115V, 0.5-kWh, 15 kW peak power
Wheels / Tires	17 x 8.5-in. aluminum/P225/55R17

The GT-Suite model was tested in a drive cycles and compared with ANL chassis dynamometer test data for validation. Figure 4.17 compares transmission gear selection, engine speed, engine torque, the GT-Suite model simulation, and the actual test result over the UDDS drive cycle.

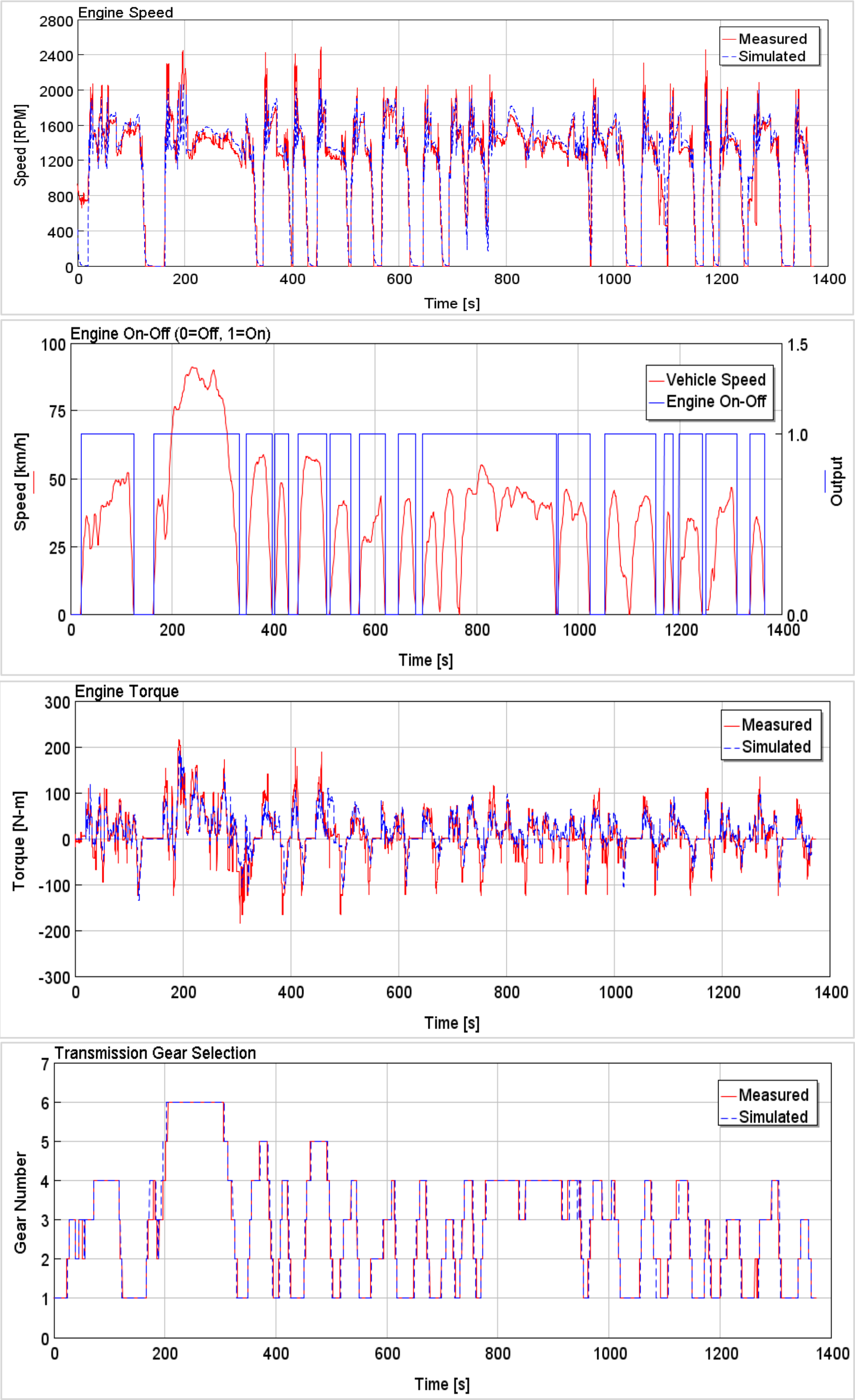

Figure 4.17 *Comparison of ANL chassis dynamometer measured data and GT-Suite simulated result on engine speed, engine on off, engine torque and transmission gear selection over the UDDS drive cycle.*

4.7 Result and Discussion of Drive Cycle Analysis

4.7.1 Conventional Powertrain

The calibrated GT-Suite model was used to analyze the drive cycle of the DM-TJI engine. The GT-Suite model F-150 engine map was replaced with the DM-TJI engine map, and the rest of the powertrain components remained the same for comparing the engine performance with that of the Ford F-150 EcoBoost®. The well-known EPA dynamometer driving schedules FTP drive cycles were employed for city fuel economy evaluation. The HWFET represents highway driving conditions under 100km/h. The supplemental US06 test was also incorporated to evaluate more aggressive and possibly realistic mixed driving conditions.

The general approach for drive cycle simulations involves the use of engine load and fuel consumption maps based on experimental and simulation steady-state results. This type of model cannot reproduce transient phenomena, and thus fuel consumption penalties due to transient effects are not accounted. Also, the multi-cylinder map-based engine model is assumed to have the same behavior as the detailed single-cylinder engine model from which the engine maps were derived.

The engine has a four-cylinder boosted configuration under high dilute conditions (45% EGR). The engine operating point over brake specific fuel consumption (BSFC g/kW-h) map is presented in the figure below for different drive cycles. It can be clearly seen that the FTP city cycle requires a much broader range of operation, owing to its frequent stop/start events, as shown in Figure 4.18. These also result in significant points at low speeds and loads, where the engine runs most inefficiently. This might be improved by adding an electrical motor with a battery to assist at the low speed and load operating points. The vehicle fuel economy is improved from 21.65 mpg using the F-150 engine to 25.15 mpg using the DM-TJI engine on the FTP city drive cycle. The operating points from the highway driving cycle are much more concentrated in a region of moderate speed, load, and engine efficiency, as shown in Figure 4.19. Engine downsizing would move the best efficiency region to the highway operating points. Compared to the F-150 engine fuel economy, the DM-TJI engine improved from 29.98 mpg to 33.13 mpg on the EPA highway drive cycle. The combined EPA city and highway drive cycle is shown in Figure 4.20, and the fuel economy improved from 24.76 mpg to 28.69 mpg. A similar behavior can also be observed in the supplemental US06 drive cycle, shown in Figure 4.21. However, a significant portion of the operating points are found at higher loads owing to the higher vehicle speeds and more aggressive acceleration events. These impact operating conditions under the best efficiency engine map region.

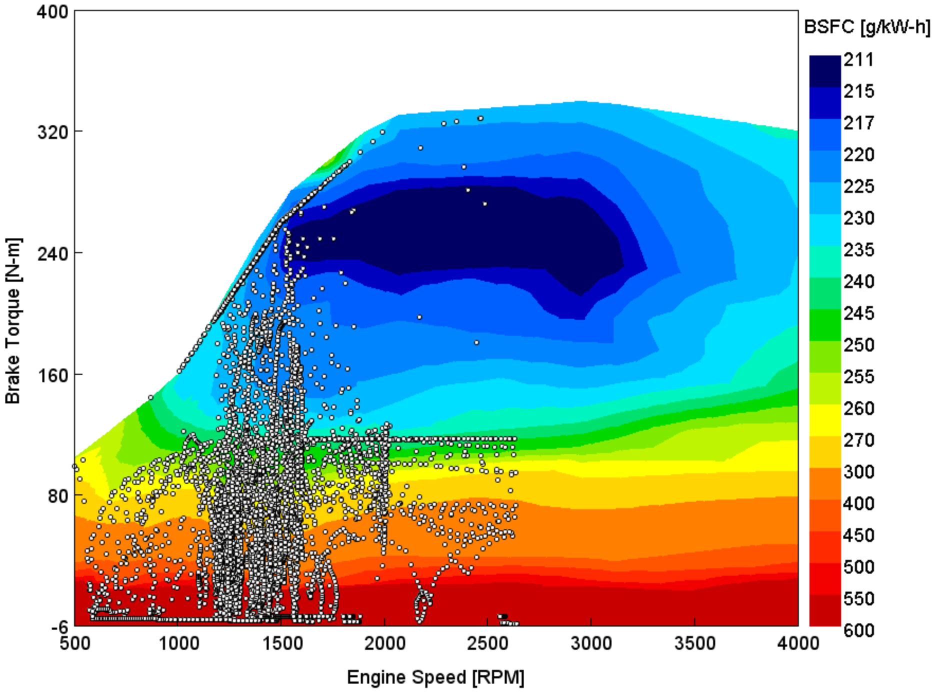

Figure 4.18 *Operating points over the DM-TJI engine brake specific fuel consumption (BSFC g/kW-hr) map in the EPA city drive cycle.*

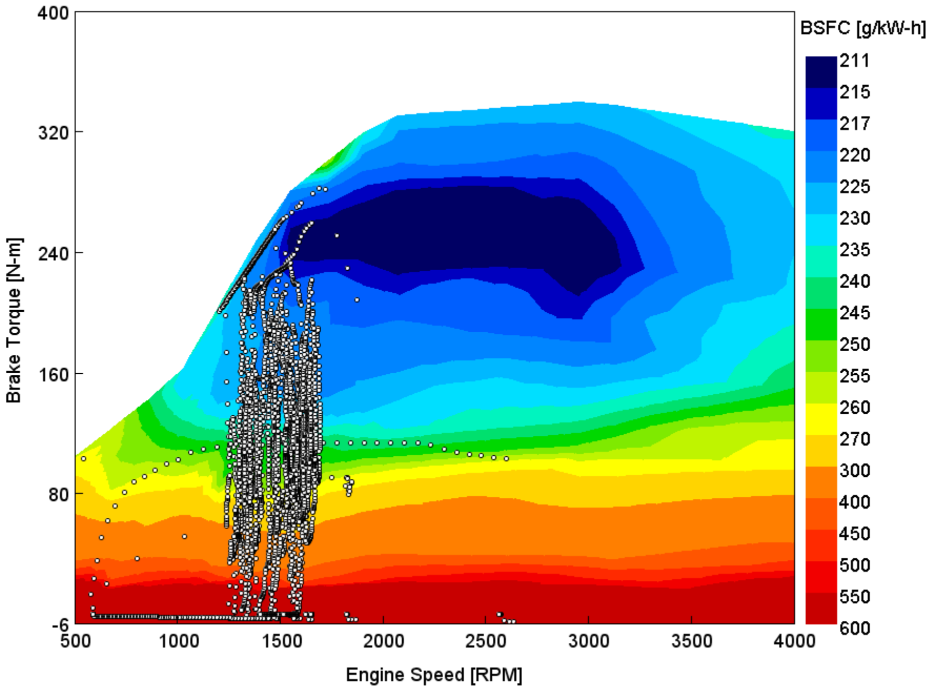

Figure 4.19 *Operating points over the DM-TJI engine brake specific fuel consumption (BSFC g/kW-hr) map in the EPA highway drive cycle.*

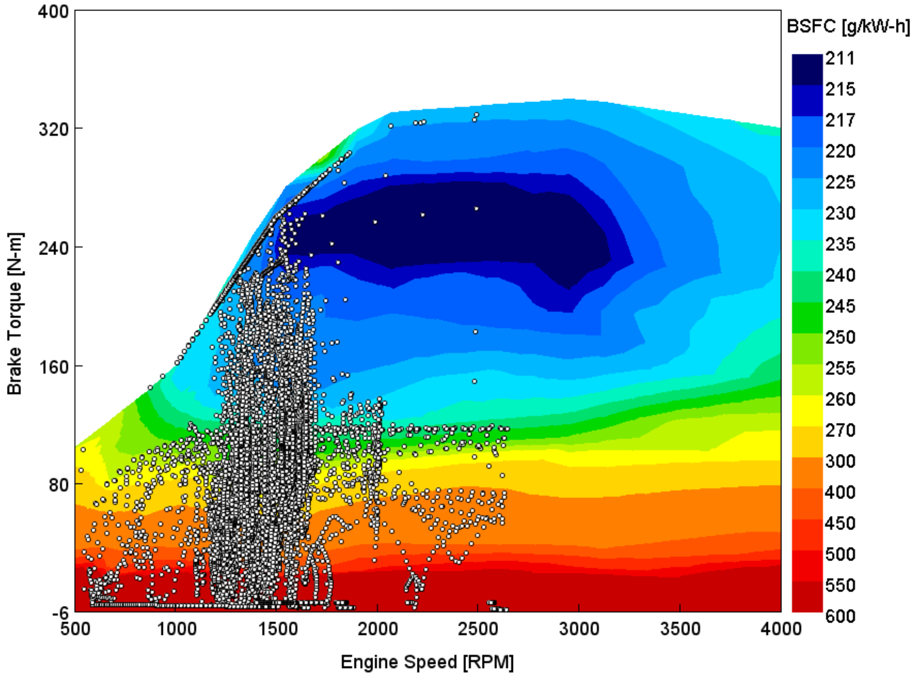

Figure 4.20 *Operating points over the DM-TJI engine brake specific fuel consumption (BSFC g/kW-hr) map in the combined (city and highway) drive cycle.*

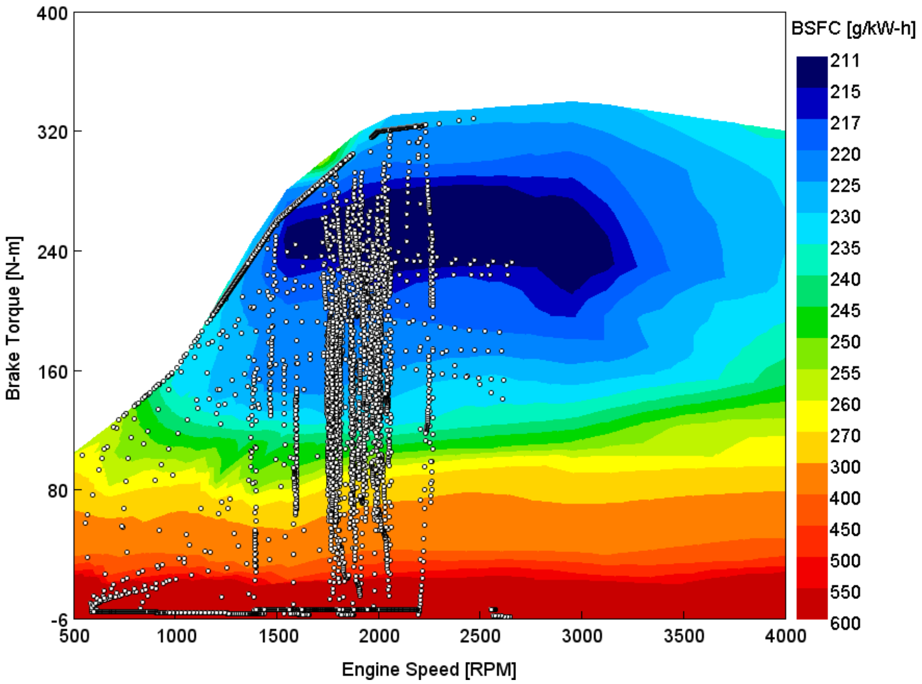

Figure 4.21 *Operating points over the DM-TJI engine brake specific fuel consumption (BSFC g/kW-hr) map in the EPA US06 high acceleration aggressive driving cycle*

The fuel economy improvement of the DM-TJI engine compared with the Ford F-150 EcoBoost® vehicle is presented in the Figure 4.22. Among the tested drive cycles, the US06 drive cycle has a higher improvement of 17.3%, and the highway drive cycle has a lower improvement of 10.5%. Overall, the combined drive cycle shows a 15.9% fuel economy improvement.

Improved fuel economy significantly reduces the release of CO2 emission. The amount of CO2 created from burning one gallon of fuel depends on the amount of carbon in the fuel. The EPA uses 8,887 grams of CO2 / gallon for gasoline fuel to estimate CO2 emissions [102]. The drive cycle fuel economy, changed into average grams of CO2 per mile and is presented in Figure 4.23. The DM-TJI engine shows between 9.5-14.8% CO2 emissions reductions on the tested drive cycles. This would be good progress toward achieving the long-term fleet target of 50 g CO2/km for future automotive powertrains [103].

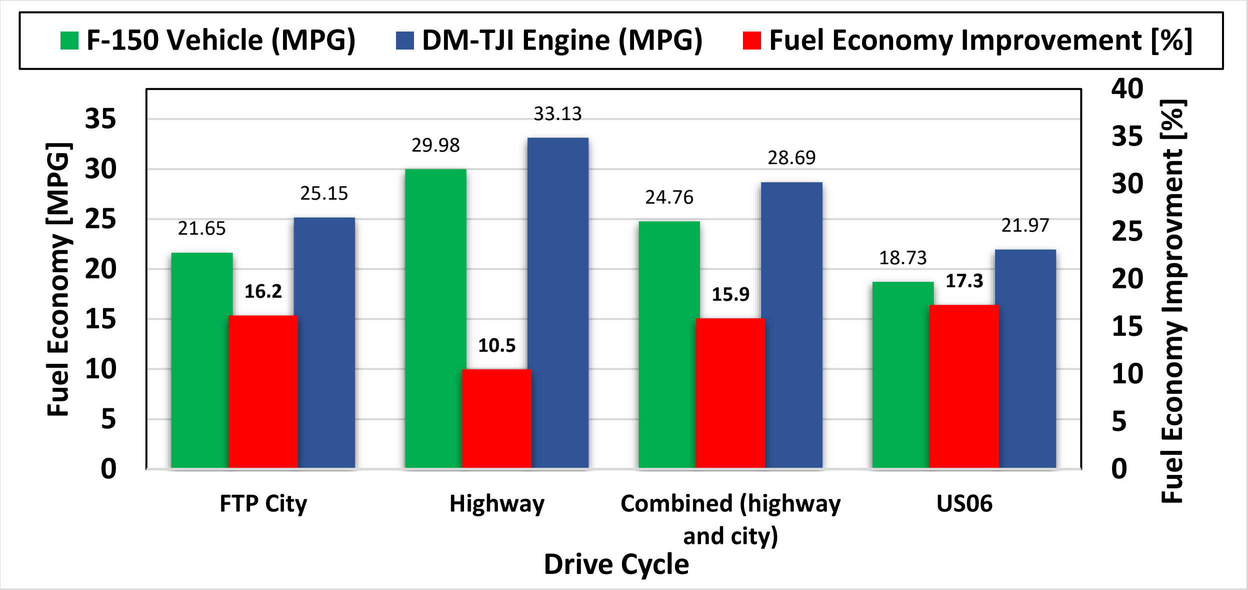

Figure 4.22 *Drive cycle average gas mileage for Ford F-150 vehicle, DM-TJI engine and fuel economy improvement.*

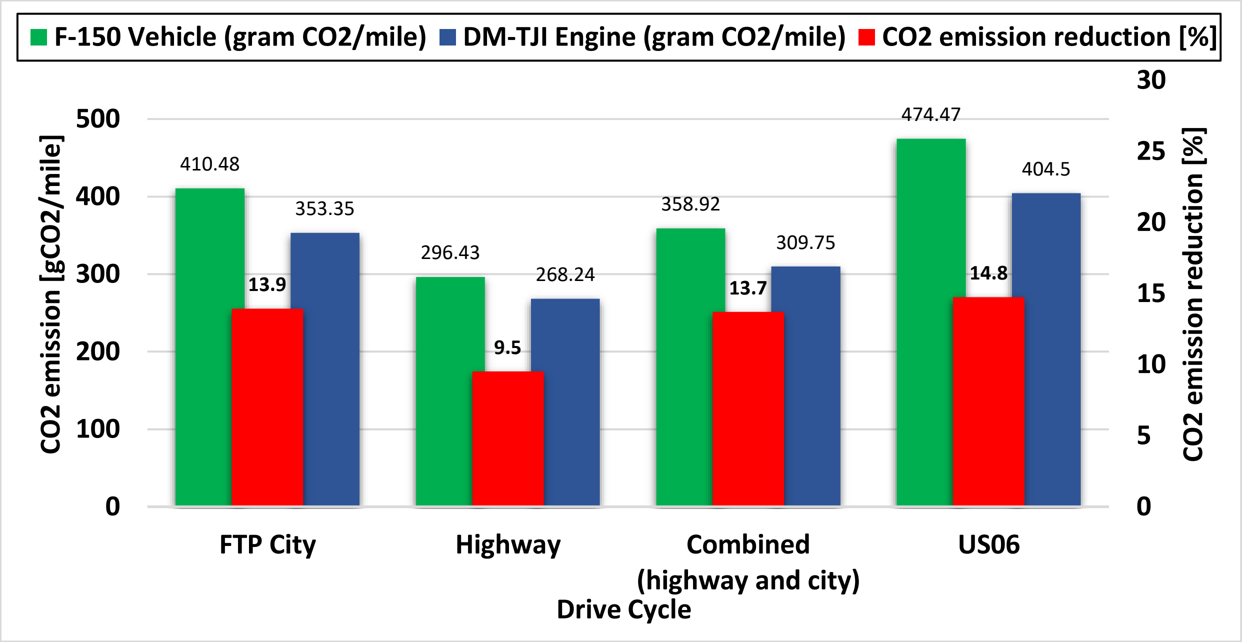

Figure 4.23 *Drive cycle average CO2 emission for F-150 vehicle, DM-TJI engine and CO2 emission reduction improvement.*

The fuel consumption equivalent CO2 emission rate (g/kwh) of the DM-TJI engine was determined and plotted on an engine map with drive cycle operating points. Figure 4.24 shows the DM-TJI engine operating points over the BSCO2 emission map for the combined drive cycle. The average fuel consumption equivalent CO2 emission for the combined drive cycle is 857.4 g/kWh. The rest of the drive cycle operating points over the BSCO2 map are added in Appendix B.

Apart from less CO2 emission, the DM-TJI engine reduce NOx emission. An indicated specific nitrogen oxides (ISNOx) emission map was created. Figure 4.25 shows the DM-TJI engine operating points over the ISNOx emission map for the combined drive cycle. The broad operating points are below 2.5 g/kWh ISNOx emissions with low emission of 0.21 g/kWh. The rest of the drive cycle operating points over the ISNOx emission map is added in Appendix B.

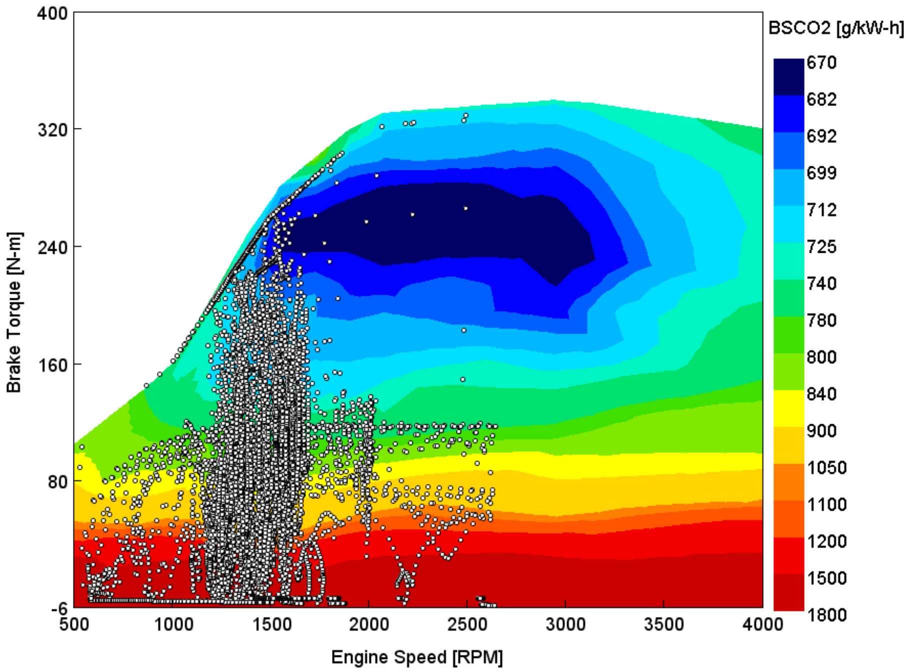

Figure 4.24 *Operating points over the DM-TJI engine brake specific CO2 emission (BSCO2 g/kW-hr) map in the combined driving cycle*

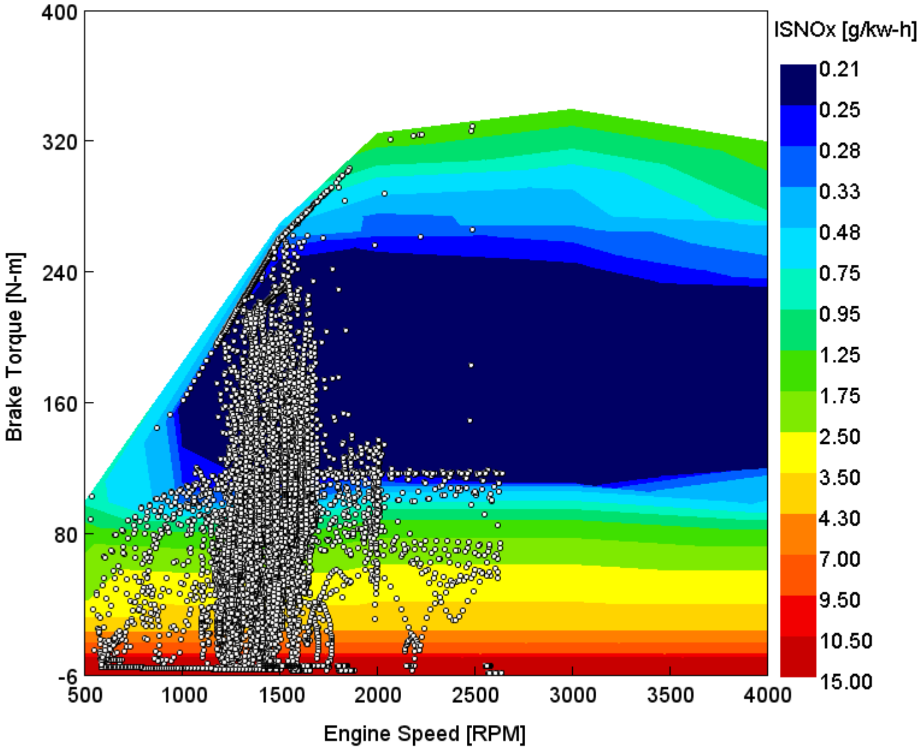

Figure 4.25 *DM-TJI engine operating point over the ISNOx emission map for the combined drive cycle.*

4.7.2 Mild and Parallel Hybrid Powertrain

Upgrade of the powertrain system is necessary to maximize DM-TJI engine benefit and to reach future CO2 emission targets. Hybrid architectures, combining electrical components and high-efficient internal combustion engines, were demonstrated to be a reliable solution that can be applied to improve the current powertrain. The DM-TJI engine is different from any SI engine by adding the pre-chamber and the pre-chamber purge air components, which demand additional work input from the engine. The mild-hybrid powertrain is a good alternative to provide the work input for the pre-chamber purge air.

Figure 4.26 compares the fuel economy results of a conventional DM-TJI engine with an electrical-powered pre-chamber air supply powertrain over the four driving cycles. An A123 Systems battery pack with 14 serious and 1 parallel connection, 0.4kWh, 48 V lithium-ion battery, and 12/15 KW (15 kW peak power in generator mode and 12 kW in motoring mode) electrical motor were added to the powertrain for the pre-chamber purge air power source. The fuel economy was improved in the range of 2.05-2.9 % on the tested drive cycles, the lower range on the US06 drive cycle and the upper range on the FTP city drive cycle.

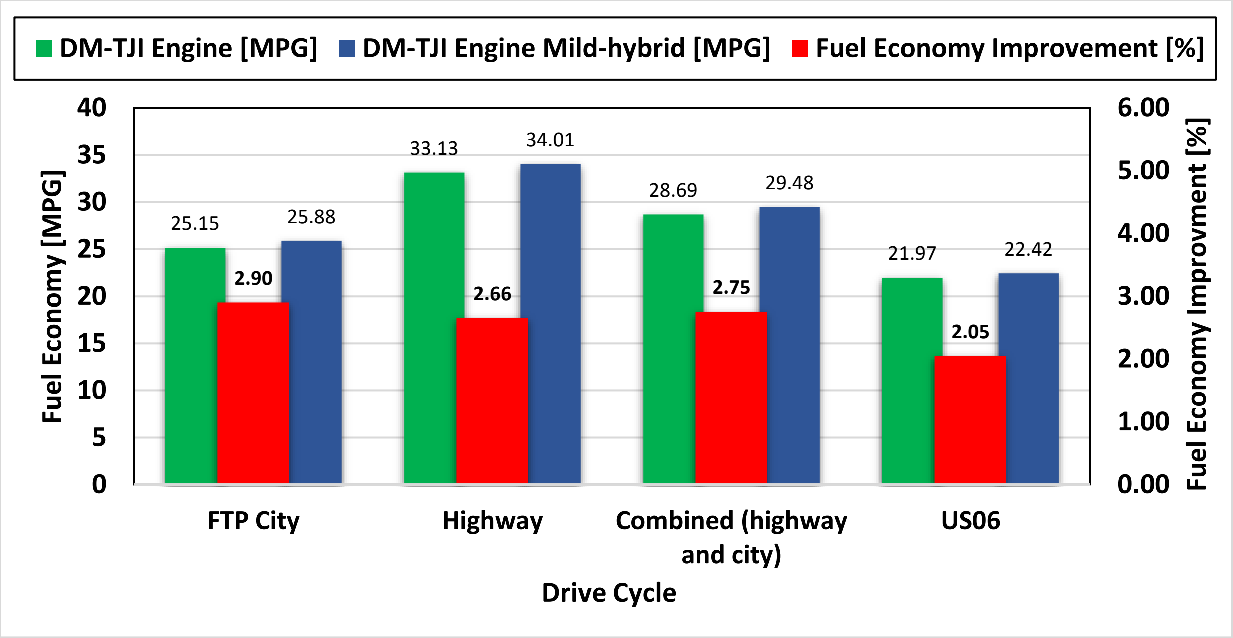

Figure 4.26 *Conventional DM-TJI engine powertrain and pre-chamber powered by electrical source powertrain fuel economy over the four different driving cycle and fuel economy improvement.*

The mild-hybrid was further analyzed by changing the powertrain to P0 system. Engine start/stop occurs when the vehicle is in an ideal state, and the electrical motor assists in starting the engine. At the peak power demand, the electrical motor assists the engine based on the battery state of charge. The battery state of charge is set between 65% - 40% (initial state of charge 65% and the minimum state of charge 40%). When the vehicle is braking, regenerative braking charges the battery. The P0 mild-hybrid powertrain simulated in the Worldwide Harmonized Light Vehicles Cycle (WLTC). The WLTC is a chassis dynamometer test cycle for the determination of emissions and fuel consumption from light-duty vehicles and shown in Figure 4.27. The WLTC drive cycle contain the low, medium, high and extra high vehicle speed, which represent all driving conditions. The DM-TJI engine vehicle conventional powertrain model drive cycle compared with the P0 mild-hybrid powertrain. The fuel economy improved from 25.8 mpg to 28.2 mpg, which shows 9.23 % and 8.45% CO2 emission reduction. A similar powertrain comparison studies with the same drive cycle report a similar results [10,83].

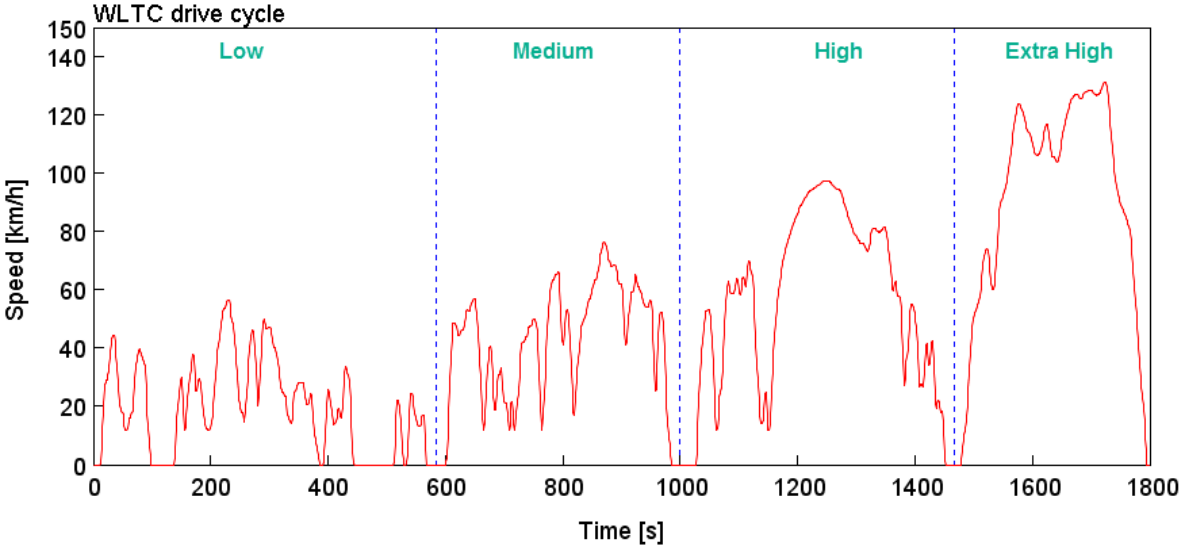

Figure 4.27 *Time Vs vehicle speed profiles of the WLTC drive cycle*

The parallel hybrid powertrain has a higher battery and electric motor capacity. The battery capacity changed to 115V and the electrical motor capacity changed to 20kW maximum power. The P2 parallel hybrid powertrain has the same feature as the mild hybrid with an additional electrical drive at a low vehicle speed and better regenerative brake efficiency. Compare to the conventional DM-TJI vehicle, the P2 parallel hybrid powertrain improve the fuel economy from 25.8 mpg to 33.6 mpg and reduce the CO2 by 23%. A similar powertrain comparison studies with the same drive cycle report a 25% CO2 reduction [10]. The rule-based hybrid control system need further improvement to get the maximum benefit of the P2 parallel hybrid powertrain. Table 4.6

summarizes the results obtained over the three different powertrains and compares the results with the conventional powertrain. The parallel hybrid powertrain improves the fuel economy by ∼30% and reduces the CO2 emission by 23%.

Table 4.6 *Fuel economy and CO2 emission simulation result of DM-TJI engine over WLTC drive cycle in three different vehicle powertrain layout*

DM-TJI Engine powertrain	**Fuel Economy [mpg]**	**CO2 emission [g/km]**	**Fuel Economy Improvement [%]**	**CO2 emission reduction [%]**
Conventional	25.84	343.92	-	-
Mild hybrid	28.23	314.85	9.23	8.45
Parallel hybrid	33.56	264.81	29.88	23.00

A similar drive cycle analysis was conducted for the Ford F-150 2.7-Liter EcoBoost®. The conventional, the P0 mild hybrid and the P2 parallel hybrid powertrain with F-150 2.7-Liter engine map analyzed over WLTC drive cycle. The results obtained over the three different powertrains and compares the results with the conventional powertrain is presented in Table 4.7.

Table 4.7 *Fuel economy and CO2 emission simulation result of Ford F-150 2.7-Liter EcoBoost® vehicle over WLTC drive cycle in three different vehicle powertrain layout*

Ford F-150 Engine powertrain	**Fuel Economy [mpg]**	**CO2 emission [g/km]**	**Fuel Economy Improvement [%]**	**CO2 emission reduction [%]**
Conventional	21.99	404.14	-	-
Mild hybrid	23.95	371.06	8.91	8.19
Parallel hybrid	27.7	320.83	25.97	20.61

The fuel economy improvement of the DM-TJI engine compared with the Ford F-150 EcoBoost® vehicle over the different powertrain and WLTC drive cycle is presented in the Figure 4.22.

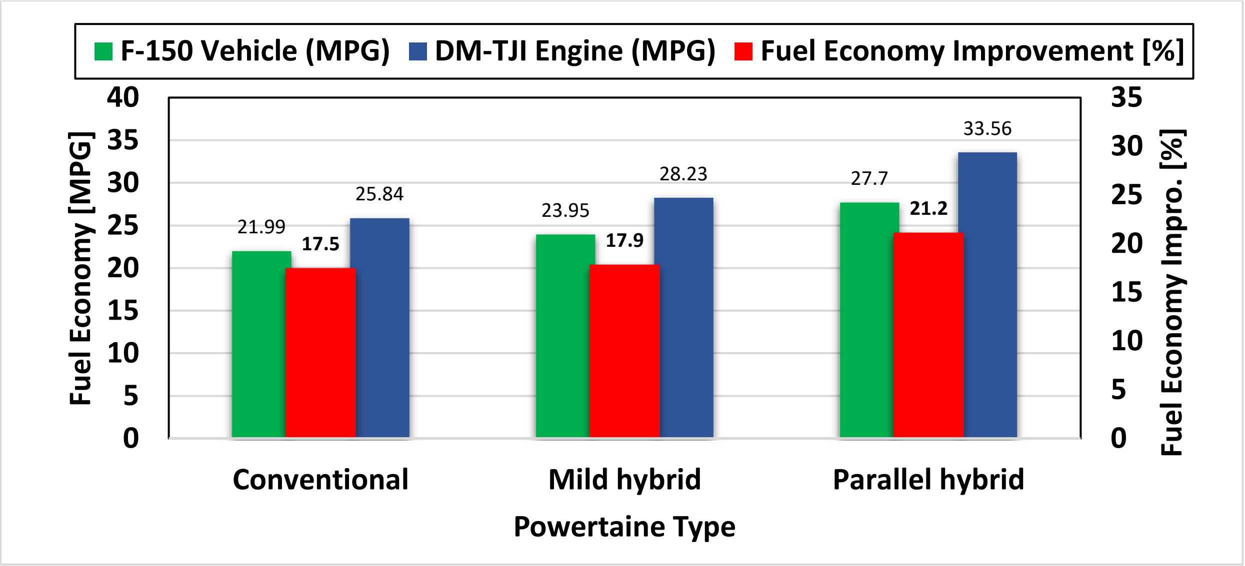

Figure 4.28 *Fuel economy comparison between Ford F-150 EcoBoost® vehicle and DM-TJI engine in different powertrain arrangement*

4.8 Summary and Conclusion

This chapter studies the powertrain model with different layouts and drive cycle analysis of a vehicle equipped with a DM-TJI engine. The commercial software GT-Suite of Gamma Technologies® was used for the powertrain and drive cycle analysis. The basic GT-Suite powertrain model consists of systems, components, and functions to execute the drive cycle analysis. The conventional powertrain model contains Engine, Transmission, Driver, Engine control, Shift control, and vehicle body properties. In addition to the conventional powertrain components, a hybrid powertrain model contains a battery, electrical motor and component-level control system. A rule-based program is prepared to provide the primary function of the hybrid powertrain. The vehicle model was validated and calibrated using tested vehicle drive cycle results.

The calibrated GT-Suite vehicle model compared the Ford F-150 2.7 Liter engine with the DM-TJI engine by replacing the engine map. The EPA dynamometer driving schedules were: FTP for the city, HWFET for highway, US06 for more aggressive drive cycle, and WLTC for hybrid drive cycle used for fuel economy and CO2 emission evaluation. The model simulation results were analyzed and summarized as follows.

- In all the tested driving cycles, the DM-TJI engine performs better than the Ford F-150 2.7 Liter engine in fuel economy and CO2 emission.
- The DM-TJI engine demonstrates 17.29% fuel economy improvement over the US06 drive cycle, 10.5% fuel economy improvement over the highway drive cycle, and 16.16% fuel economy improvement over the FTP city drive cycle. Overall, the combined city and highway drive cycle shows a 15.87% fuel economy improvement. The comparison was made with the same vehicle components of the Ford F-150 2.7-Liter except for changing the engine map.
- The engine significant operating points were at low to moderate speeds and loads, where the engine runs most inefficiently. This might be improved by adding an electrical motor with a battery to assist low speeds and load operating points.
- Engine downsizing would move the best efficiency region of the engine map to the most engine operating points.
- The DM-TJI engine shows between 9.5-14.8% CO2 emissions reductions on the tested drive cycles.
- The DM-TJI engine reduces NOx emission; the broad operating points are below 2.5 g/kWh ISNOx emissions with low emission of 0.21 g/kWh.
- The hybrid powertrain was demonstrated to be a reliable solution that can be applied to improve the current powertrain. Replacing the power source of the auxiliary pre-chamber air supply with electrical power further improved the fuel economy in the range of 2.05-2.9 % over the tested drive cycle.

- Mild and parallel hybrid powertrain further improve the fuel economy of the DM-TJI engine by 9.23% and 29.88%, respectively, compared to the conventional powertrain of the DM-TJI engine. The CO2 emission was reduced by 23%. Further optimizing the hybrid powertrain control algorithm could maximize the drive cycle fuel economy.

Chapter 5: Combustion Characteristics and Emission Trends in the DM-TJI (Jetfire®) Engine with Alternative Fuels

5.1 Introduction

Both academia and industry have been continuously studying to attain maximal benefit from SI engines working on gasoline and alternative fuels to improve the emissions, combustion, and performance parameters. Many renewable fuels and abundant reserve gases have been studied and widely used as alternative fuels for ICEs, including biofuels such as methanol, ethanol, butanol, and gaseous fuels such as hydrogen, natural gas, and petroleum gas. Ethanol and natural gas (NG) are the most widely employed fuels among these fuels [104].

Ethanol constitutes about 75% of renewable fuel production, with additional biomass-based production methods potentially scaling up yield in the future [105]; it is widely used as engine fuel in several countries. Ethanol can be obtained from renewable sources such as biomass and agricultural feedstock (sugarcane or corn). The self-ignition temperature of ethanol is higher than that of gasoline. Therefore, an ethanol-fueled engine is less likely to knock than a gasoline-fueled engine at the same compression ratio. This allows for higher knock-free compression ratios for SI engines, which leads to the higher overall efficiency and shaft power [106]. The flame speed of ethanol is higher than that of gasoline, and it permits fast combustion. In addition, ethanol fuel has high vaporization heat; it reduces the maximum temperature inside the cylinder and hence reduces the NOx emission and increases the engine power [107].

The use of ethanol in SI engines is still limited by its high latent heat of vaporization and low energy density. The high latent heat of ethanol leads to an increase in the volumetric efficiency.

Ethanol has low diffusivity and shows ignition difficulty at low temperature, causing incomplete combustion and adversely affecting engine economic and emissions performance [108].

NG is one of the most abundant and promising alternative fuels. It is promising for partially substituting the traditional fossil fuels and reducing global warming effects by reducing the carbon dioxide (CO2) emission due to its primary component of methane (99.99 %), which has the highest hydrogen/carbon ratio among all fuel hydrocarbons [109]. It can be mixed thoroughly with air to form a homogenous fuel/air mixture for combustion in the cylinder, and NG significantly reduces the engine exhaust emissions.

Generally, natural gas is stored in special high-pressure gas cylinders and is typically divided into compressed natural gas (CNG) and liquefied natural gas (LNG). CNG is suitable for short-distance passenger cars, while LNG is suitable for the fuel supply of the long-haul transport sector because the energy density of LNG is higher than that of CNG [104]. By shifting the gasoline and diesel engines to NG engines, the HC and CO emissions can be reduced by 30–35% and 20–30%, respectively [110].

NG can be used in a high compression ratio engine due to its high octane number, which provides superior anti-knock resistance. The octane level enables NG to be used directly in the SI engines at a relatively higher compression ratio (CR) than gasoline engines, which brings about higher thermal efficiency and higher cost-effectiveness. In recent years, energy shortage and environmental pollution have drawn increasing attention from governments worldwide towards NG as the alternative fuel for heavy-duty diesel engines and stationary engines [111].

However, the NG composition has a unique tetrahedral molecular structure with larger C–H bond energies. Demonstrating unique combustion characteristics such as high ignition temperature and low flame propagation speed will counteract the superiority of emissions due to significant cycle-to-cycle variations, particularly under lean mixture operating conditions, in cold start, and under idle and low load conditions [112]. Consequently, the NG engine is usually equipped with a high-energy ignition system and operated at the stoichiometric air/fuel ratio over a wide range of load and speed [109].

Stoichiometric operation combined with a three-way catalyst (TWC) has been recognized as the most effective way for SI engine operation to meet stringent emission legislation. However, significantly higher combustion temperature with stoichiometric operation leads to higher heat transfer loss, higher thermal stress on the engine, and higher knock tendency. At low-to medium-loads operation, more throttling is also needed, which leads to more pumping loss. All these factors would result in a decrease in the engine's thermal efficiency. Burning high diluted mixtures (exhaust gas recirculation) has improved engine efficiency in several ways. The heat losses through the combustion chamber walls are significantly reduced, and the pumping losses are reduced when the engine operates at medium-to-low loads. High diluted mixtures offer the potential to mitigate SI knock at high engine load [39]. On the other hand, introducing an EGR diluted mixture in the combustion chamber will inevitably lower the combustion reaction rate, which also has an adverse effect on thermal efficiency. Concerning this issue, the combustion chamber structure should be further modified to optimize in-cylinder flows, increase the turbulence intensity, and accelerate the flame propagation process. Pre-chambers combustion presents a promising method to reduce the ignition difficulties of EGR diluted mixtures outlined above. In such configurations, a mixture of air and fuel is ignited in the pre-chamber, and burning jets are discharged into the main chamber [103].

An active pre-chamber ignition system characterized by an additional fuel injection system provides another degree of freedom for controlling the mixture in both chambers. A different fuel can be injected into the pre-chamber for a better mixture and fast burn. Gaseous fuels like methane, hydrogen, and propane are usually adopted to get better mixture formation in an active pre-chamber because of the reduced momentum of the liquid. The amount of fuel injected into the pre-chamber is another key operating parameter since it determines the pressure rise and the combustion duration in the pre-chamber. This parameter is determined by the pre-chamber volume and the pre-set air/fuel ratio to maintain combustion stability.

Many researchers investigated the effects of alternative fuels and dual-fuel combustion in regular SI and TJI engines with and without EGR dilution. Toulson et al. [113] studied the effect of alternative fuels in the pre-chamber (H2, CNG, LPG, and CO) and gasoline fuel in the main chamber. They concluded that the main chamber lean limit was affected by the fuel choice in the pre-chamber. However, the emissions do not vary significantly between pre-chamber fuels. Sementa et al. [114] analyze the combustion process of an optically accessible small SI engine fueled with methane and equipped with a pre-chamber. Sementa forward fueled pre-chambers offer the possibility to enhance the lean operating limit of methane engines while ensuring stable operation at high excess air ratios. Costa et al. [115] used hydrous ethanol as the fuel in a single-cylinder optical engine equipped with a homogeneous charge pre-chamber. Their study reported that the pre-chamber torch ignition engine improved indicated specific fuel consumption by 4.5%, and engine fuel conversion efficiency improved 5.4% compared to the baseline engine at $\lambda = 1.4$. The NOx pollutant emission level for the pre-chamber torch ignition system was reduced with leaner mixtures by 52% compared to the stoichiometric baseline engine. Zardoya et al. [116] investigated optimal combustion and design needs for low methane number fuels in a pre-chamber injected engine. A 15% efficiency drop was obtained, and different engine design modifications were proposed. Liu et al. [117] investigated the combustion characteristics of premixed CH4-air and H2-air mixtures with different excess air coefficients ignited by jet flame with different pre-chamber orifice diameters. The results show that the variation of orifice has diverse influences on the turbulent jet ignitions of methane and hydrogen. Smaller orifices will reduce the temperature of the jet due to the stronger stretch and throttling effect, including change of lean flammability limit, ignition delay, and re-ignition location. Costaet al. [118] analyzed a homogeneous charge pre-chamber torch ignition system in an SI engine fueled with a gasoline-bioethanol blend. BSFC was improved up to 8.4%, 12.1%, and 10.2% for engine speeds of 2500, 3500, and 4500 rpm, respectively. Alvarez et al. [119] operated a multi-cylinder engine using ethanol as the main chamber fuel with three combustion modes: standard spark ignition, passive pre-chamber, and active pre-chamber at specific engine speed and load. They showed a reduction in specific fuel consumption and the combustion duration with the use of pre-chamber ignition system. Almatrafi et al. [39] studied the effects of using two different fuels in the main chamber and assessed the lean limit, the combustion efficiency, and the emissions of a single-cylinder heavy-duty engine equipped with a narrow-throat active pre-chamber. The results showed an increase in the lean limit using ethanol in the main chamber compared to using only methane in both chambers.

Hence, this chapter aims to study the effect of alternative fuels on high compression ratio pre-chamber ignition systems. The combustion parameters, engine stability, EGR dilution tolerance, and exhaust emission were compared with gasoline and between the fuels. The experimental activity was carried out on a single-cylinder DM-TJI metal engine. Furthermore, the engine response is studied using two different fuels in the engine pre- and main chamber cylinders.

5.2 Experimental Setup and Procedure

A single-cylinder Prototype III DM-TJI metal engine coupled to a dynamometer was used for all experiments. A schematic of the experimental setup is shown in Figure 5.1. Significant engine specifications are given in Table 5.1. The engine setup used in this study is the same as the engine explained in chapter 2; except for alternative fuel, a different fuel delivery system and injector implemented, and pre-chamber orifice diameter of 1.5mm used for the alternative fuel analysis.

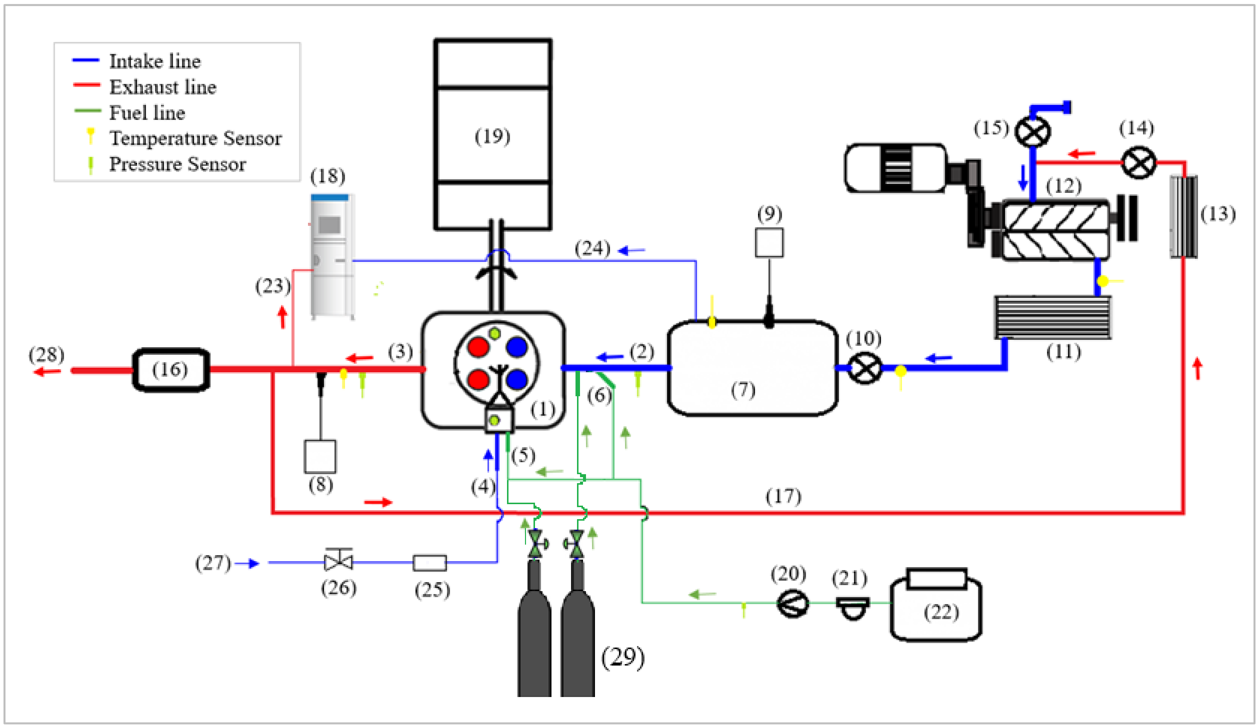

***Figure 5.1** The schematic diagram of the experimental setup*

(1) Engine head with pre-chamber, (2) Intake runner (3) Exhaust runner (4) Auxiliary pre-chamber airline (5) Pre-chamber fuel injector line (6) Main chamber injector line (7) Intake plenum (8) Lambda sensor (9) Intake O_2 sensor (10) Intake throttle (11) CAS (12) Supercharger (13) EGR cooler (14) EGR valve (15) Upstream throttle (16) Muffler (17) EGR line (18) HORIBA exhaust gas analyzer (19) Dynamometer (20) Fuel pump (21) Fuel flow meter (22) Liquid Fuel thank (23) Exhaust emission line (24) Intake CO_2 line (25) LFE (26) Pre-chamber pressure regulator (27) Shop compressed air supply (28) Vent (29) Methane fuel cylinder

The engine was instrumented with thermocouples to monitor the intake and exhaust manifold and selected coolant lines and oil gallery temperatures. The engine in-cylinder pressure data used to calculate indicated mean effective pressure (IMEP) and COV_{IMEP} in both chambers was recorded with a pressure transducer (Kistler). The COV_{IMEP} calculated the average of over 200 consecutive engine cycles. Piezoresistive pressure transducers were installed on the intake and exhaust runner manifold to measure the port pressures. An ABB electrical motor was used to operate the engine at a constant speed and act as a dynamometer.

Table 5.1 *Specification of the test engine*

Parameter	**Description**
Engine type	Single-cylinder, four-stroke
Ignition mode	High energy spark ignition
Displacement (L)	0.55 L
Bore	86 mm
Stroke	95 mm
Connecting rod length	170 mm
Compression ratio	13.3:1
Fuel type	Gasoline, E80 ethanol blend, and compressed natural gas.
Injection mode	Direct injection in pre-chamber and port injection in the main chamber
Pre-chamber volume	2.9 ml (~6 % of clearance volume)
Number of Nozzle orifice and configuration	6 holes, Symmetric
Orifice diameter	1.5mm
Number of Valves	2-intake, 2-exhaust, and 1-pre-chamber
Valve timing for max lift	Intake timing - 90 CAD aTDCGE, Air valve timing - 110 CAD bTDCF Exhaust timing - 90 CAD bTDCGE
Aspiration mode	Naturally aspirated and Boosted

A Horiba MEXA-7100 DEGR automotive exhaust gas analyzer bench measured raw emissions of NOx, O_2, CH_4, CO, CO_2, and unburned THC emissions. It also measures the EGR dilution rate, which was calculated using measured CO_2 concentrations in the intake and exhaust manifold while accounting for ambient CO_2 concentration. The analyzer was calibrated prior to the experimental tests with zero and span gases. An exhaust gas recirculation (EGR) system was used, where the charge was fed upstream from the intake surge tank, allowing time for mixing before the intake manifold. A Meriam laminar flow element (LFE) was installed to measure the pre-chamber airflow installed in the pressurized airline upstream from a compressed air plenum. The plenum is used to minimize pressure fluctuation.

Tier III regular certification gasoline fuel, E80 ethanol fuel blends, and compressed natural gas are used as fuel in different combinations. The engine fuel supply line was divided into two lines, each providing fuel to a separate chamber which fueled both the pre- and the main chambers. The combined pre- and main chamber fuel flow rate was measured using a Micro Motion (Mod. No CMFS007M) Coriolis flowmeter for liquid fuels and the displaced bubble method for gas fuel. Both the pre-chamber and main chamber fuel injection pressures were set at 1450 psi (~100 bar) for liquid fuels and 400 psi (27.57 bar) for pre-chamber, and 100 psi (6.89 bar) for the main chamber for gas fuel. The pre-chamber fuel was supplied with a custom-developed two-hole, low-flow DI injector, whereas the main chamber fuel was supplied in PFI configuration but with a higher flow rate six-hole DI injector. The main chamber injector was replaced by a Bosch NGI2 natural-gas port fuel injector for natural gas fuel. The fuel injection time and durations were controlled and adjusted by an in-house developed control system containing NI-PXI chassis and Mototron controllers managed within an NI Veristand environment. Spark timing, intake runner throttle, and EGR valve position are also controlled from this end. Two data acquisition systems were used: A&D Technology Combustion Analysis System (CAS) for high-frequency data sets and National Instruments (NI) device for low-frequency data sets.

5.3 Experimental Results and Discussion

The tests were carried out at stoichiometric conditions under different fuel matrices. A summary of the fuel test conditions is shown in Table 5.2. Different quantities are required to achieve the stoichiometric mixture conditions because the fuels have different energy densities. Before starting the tests, an engine warm-up routine was followed until stable coolant temperature conditions of 90°C were obtained. Lambda was adjusted to one after the engine warm-up and start of data acquisition. Each parameter was assessed at a low and high EGR dilution rate starting from 0% until the fuel EGR limit was reached, which is determined by $COV_{IMEP} < 3\%$. The knock limit is set to be less than 10% cycle crossing a 1.0 bar pressure oscillation difference (POD).

Table 5.2 *Engine fuel test parameter*

	Pre-Chamber	**Main Chamber**
Fuel 1	Gasoline	Gasoline
Fuel 2	Methane	Methane
Fuel 3	E80 ethanol blend	E80 ethanol blend
Fuel 4	Gasoline	Methane
Fuel 5	E80 ethanol blend	Methane

A standard motored operating point was recorded and analyzed to ensure repeatability and consistency between experimental test sets. At the start of each test day, the emission bench was purged and calibrated using span and reference gases. The spark timing was adjusted to achieve Maximum Brake Torque (MBT) operation. More than 30% EGR dilution helps achieve a CA50 combustion phasing of between 6 – 9 CAD aTDCF under the knock limit. When the test point passed the knock limit, the spark timing retarded, and the CA50 might be above 10 CAD aTDCF.

The fuel flow rate into the main chamber was controlled to obtain a stoichiometric mixture (λ=1) for the exhaust gas constituents. The lambda was measured by the exhaust emission bench and ECM Lambda-5200 sensor installed at the exhaust system. Once a stable operating point was achieved, 200 combustion cycles were recorded at a crank angle resolution of 0.1 using the CAS data acquisition system. The low-speed test cell data was recorded at 1Hz for the same duration as the high-speed data recording. The most representative cycle was used for analysis, which was defined to be an individual cycle that was closest to the average CA50 and IMEPg. The combustion stability is defined by the COV_{IMEP} over the recorded combustion cycles. An in-house MatLab script was used to post-process the experimental data.

5.3.1 EGR Sweep Results Using Alternative Fuels

5.3.1.1 Engine Knock

The knock amplitude of the EGR sweeps for the different fuel test matrix are shown in Figure 5.2. Gasoline fuel injection in both chambers shows significant knock amplitude. However, the knock amplitude decreases as the EGR dilution increases, and the engine can operate with a wide range of EGR dilution with low knock amplitude beyond 25% dilution rate. E80 ethanol blend in both chambers operates above the knock limit without EGR dilution; once the EGR dilution starts, the engine can operate with low knock amplitude beyond 10% dilution rate. However, the knock limit is not reached for any combination of methane fuel.

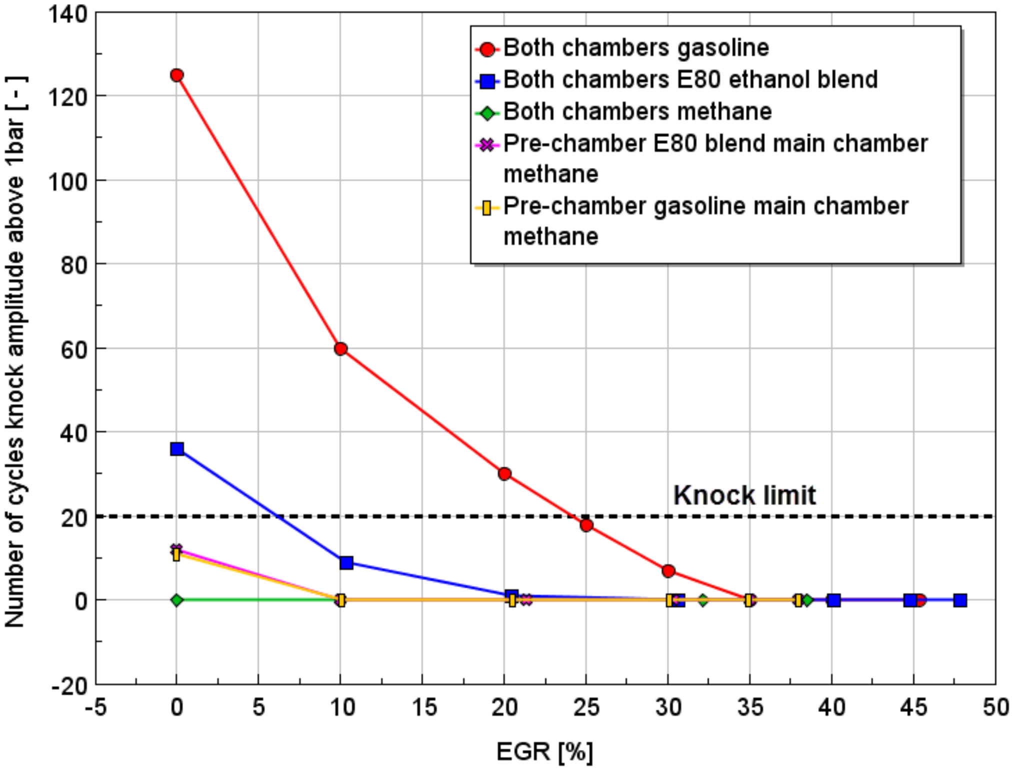

Figure 5.2 *Knock limit of alternative fuels in a DM-TJI engine with EGR dilution rate at 1500 rpm engine speed*

5.3.1.2 Main Chamber Pressure Trace and Apparent Heat Release Rate

EGR dilution in the combustion mixture decreases the laminar flame speed and consequently leads to slower combustion [120]. The ignition chemistry changes through an increase of quenching reactions due to EGR diluents and leads to increased ignition delay. Figure 5.3 shows the benefits of combustion phasing and better knock relief provided by the high EGR dilution rate at a high engine compression ratio. Knock typically exhibits with high heat release rate; the EGR dilution rate provides better combustion phasing, which leads to higher cylinder pressure with decreased heat release rate, which provides more knock relief while still maintaining good combustion stability.

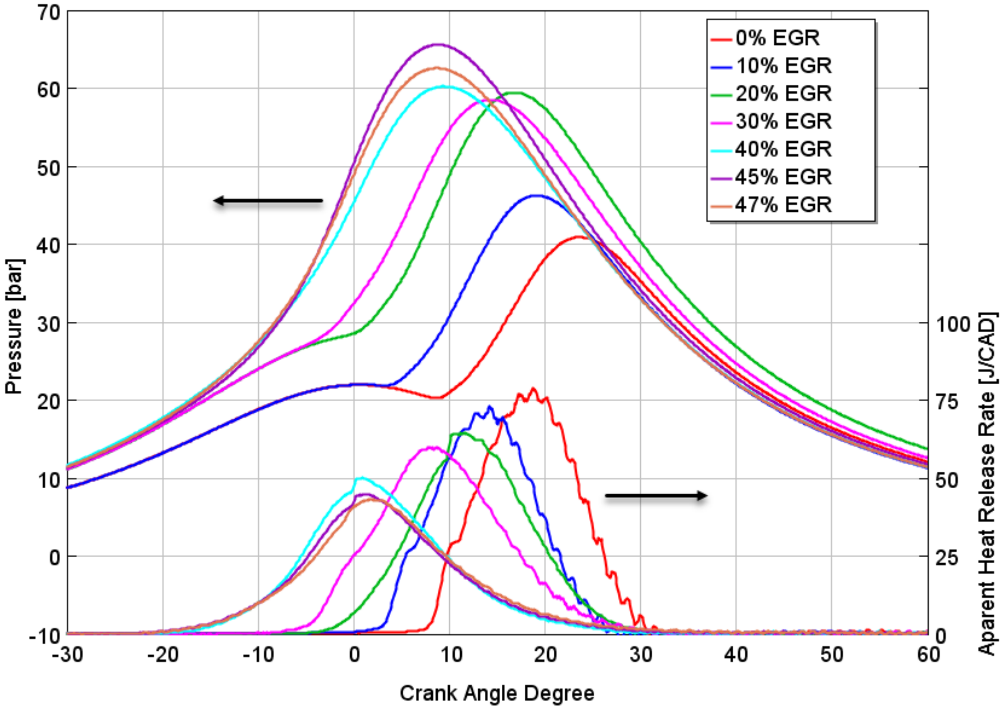

Figure 5.3 *Main chamber pressure and apparent heat release rate with different EGR dilution rates and corresponding spark timing using E80 ethanol blend fuel*

5.3.1.3 Combustion Stability

The combustion stability of the EGR sweeps for different engine fuel are shown in Figure 5.4 for the same fuel in both chambers and Figure 5.5 for different fuel in each chamber. Methane fuel in both chambers and combined with other tested fuel in the main chamber has an EGR tolerance of 38%. However, injecting methane in the pre-chamber using a custom-developed two-hole, low-flow DI injector for such a long time was not successful; more than two injectors were damaged in the test process. Methane gas does not have the same lubrication as liquid fuels; after repeated engine tests, the injector starts to leak and create high CH4 emissions. After the pre-chamber injector started to leak, the maximum EGR tolerance of methane injected in both chambers was 20%. E80 ethanol blend has stable combustion up to 47% EGR dilution, while the gasoline enabled a 45% EGR rate before combustion became unstable. The straight-line markers in Figure 5.4 and

Figure 5.5 represents the spark timing for each fuel type, and it is evident that, with a high EGR dilution rate, all fuel operating conditions required spark advance at the same combustion phasing.

The fuel injection and auxiliary air supply to the pre-chamber increases when the EGR dilution rate exceeds 35%. This indicates that the pre-chamber residual gas fraction increased with a high EGR dilution rate, and it needed more air in the pre-chamber to scavenge the residual gas. More air in the pre-chamber needs more fuel to start stable combustion. The engine has a wide range of spark sweep points with stable combustion with less EGR dilution rate. However, with a high EGR dilution rate, the spark sweep range with stable combustion became smaller and smaller; it needed to find a small window of stable combustion spark timing points to have stable combustion.

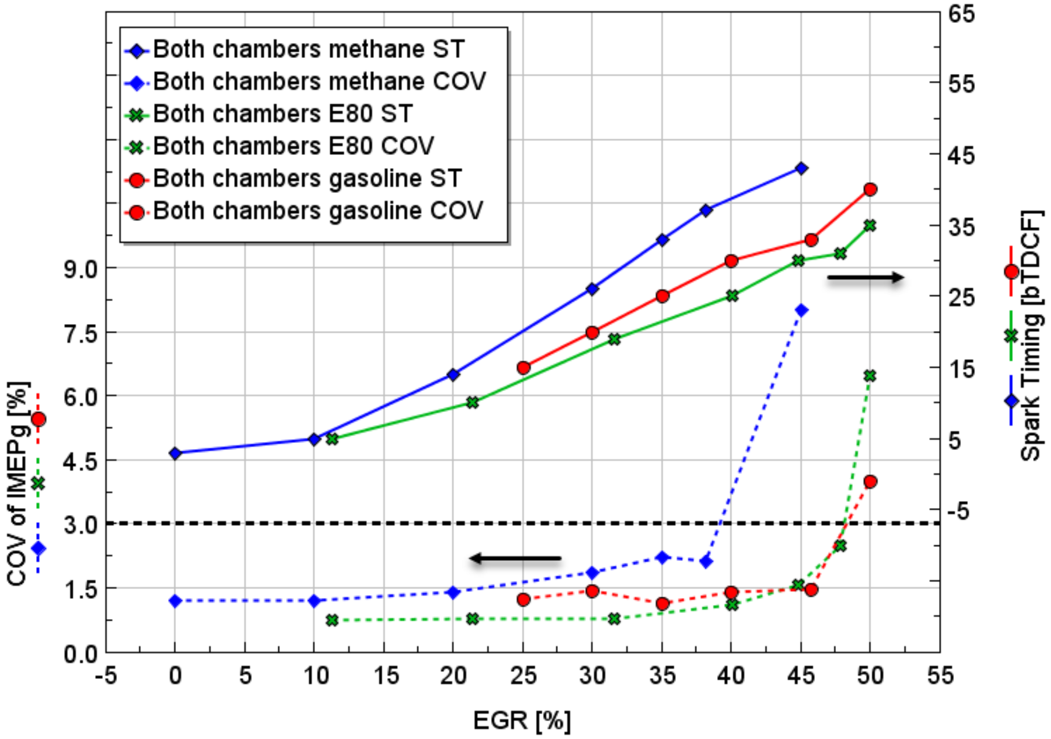

Figure 5.4 *Combustion stability (COV$_{IMEP}$) and spark timing of three different fuels (methane, E80, and gasoline) using the same fuel in both combustion chamber with EGR sweeps.*

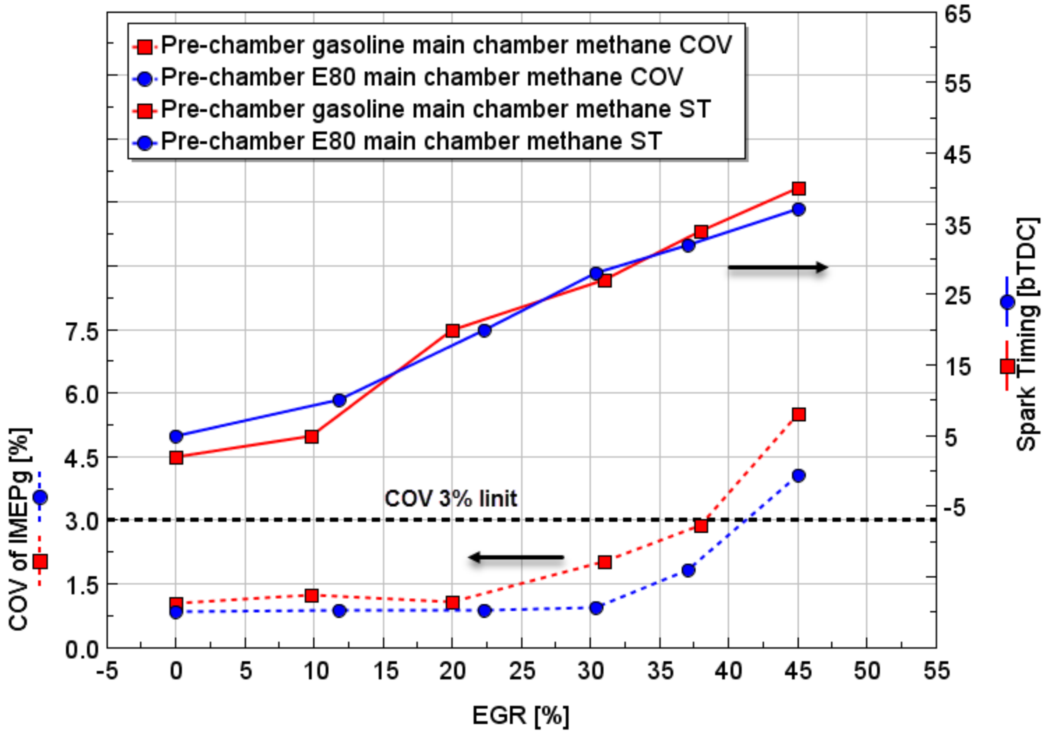

***Figure 5.5** Combustion stability (COV_{IMEP}) and spark timing of three different fuels (methane, E80, and gasoline) using different fuels in each combustion chamber with EGR sweeps.*

Gasoline fuel was more sensitive to knock-in-advance spark timing when injected into both chambers (compared to the rest of the fuels). Methane fuel has better combustion stability in a diluted mixture when the engine burns in lean conditions than in rich conditions. When the EGR sweep performs, the engine burns in lean condition for a time until the combustion reaches the dilution target, and then the combustion state goes back to stoichiometric condition. In contrast, gasoline fuel has better combustion stability when the engine burns in rich conditions than lean at high EGR dilution rate; the engine burns in a rich state for a time to sweep the EGR dilution rate. Conversely, E80 ethanol blend fuel has better combustion stability in both lean and rich conditions, and it is easy and fast to sweep the EGR dilution rate.

5.3.1.4 Combustion Duration

The combustion duration for EGR sweeps is shown in Figure 5.6, and the delay between the spark timing and 10% heat release is shown in panel (a). This time delay is also known as the flame development angle measured in CAD. At zero EGR dilution, the flame initiation was similar for the tested fuel matrix with a maximum of 2 CAD difference. The delay increases as the combustion mixture is diluted with more EGR. E80 ethanol blend fuel has a shorter flame initiation angle than the other fuels. Methane fuel in the main chamber or both chambers' fuels show the most extended delay, while gasoline fuel is in the mid-range between the two fuels. Hence, a shorter flame development angle can be expected using fuels with lower octane ratings [121].

The duration between 10 to 90% heat release (CA10-90) is plotted in Figure 5.6 (b). The combustion duration of each fuel in this study is extended as the EGR dilution rate increases. For a given EGR dilution condition, shorter durations are achieved by E80 ethanol blend fuel. Due to its slow laminar burning velocity, methane fuel shows the most extended combustion duration among the fuels studied for a given EGR percentage. The rate at which the combustion duration increases with increasing EGR dilution rate is similar for all the tested fuels.

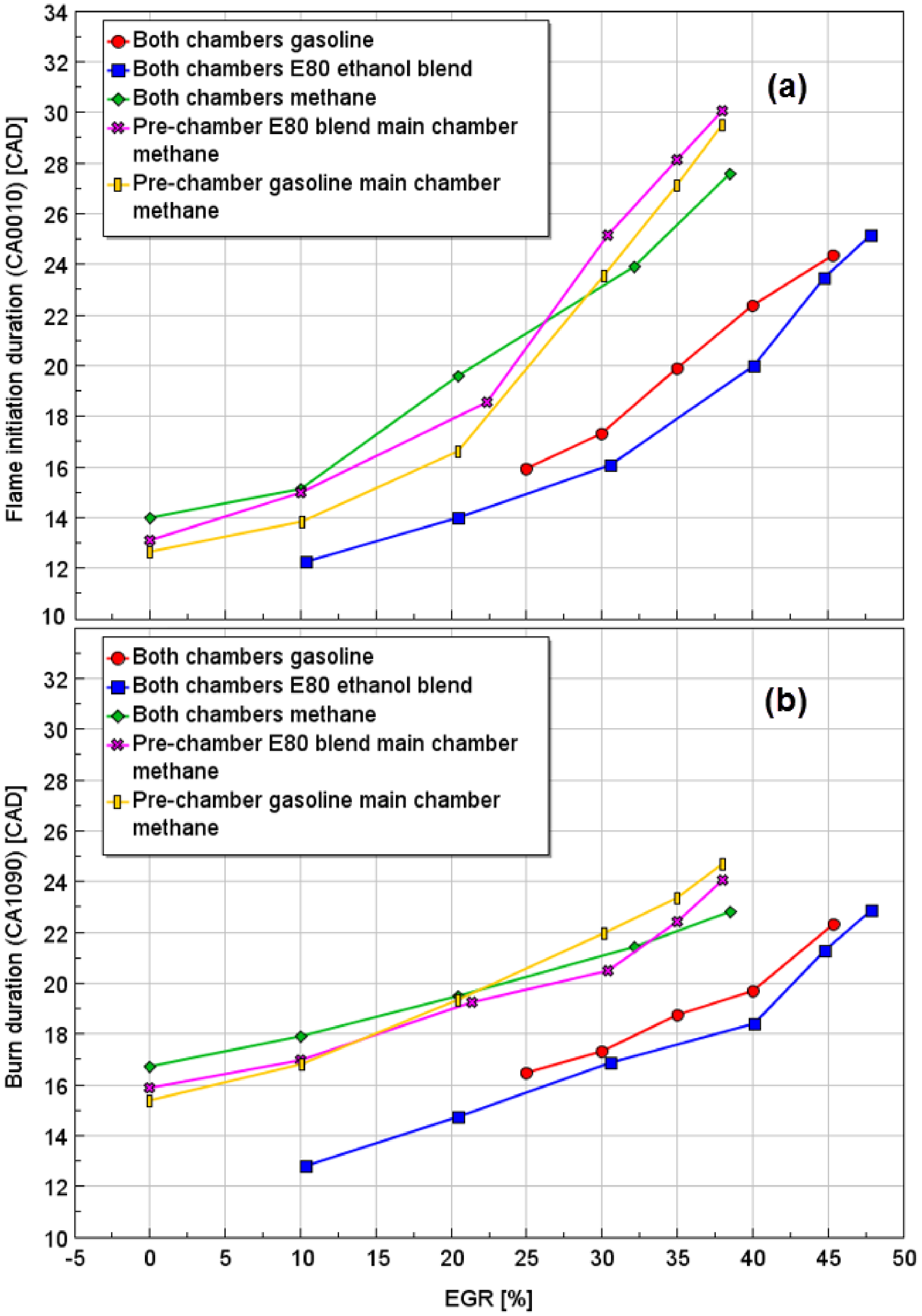

Figure 5.6 *Different fuel combustion durations of CA0010 (a) and Burn1090 (b) in a DM-TJI engine as a function of EGR dilution rate*

5.3.1.5 Exhaust Emissions

Engines emit several pollutants into the atmosphere, significantly contributing to air pollution. The main toxic substances present in the exhaust gases are incomplete combustion oxides of a hydrocarbon containing CO, NOx, HC, and particulates. Unlike CO2, the emission of these pollutants is not directly linked to fuel consumption, being more dependent on engine technology and maintenance. The engine exhaust emissions are typically measured using a gas analyzer and reported in parts per million (ppm) and volume percent (vol %). A portable emissions analyzer (Horiba MEXA-7100) was used. The analyzer consists of a sampling probe, an analyzer box, and a control unit and is equipped with CO(H), CH4, O2, CO2, THC, and NOx analyzers. Table 5.3 summarizes the technical specifications of the exhaust gas analyzer used in this study.

Table 5.3 *Technical specifications of the exhaust gas analyzer.*

Measurement	Accuracy	Range
CO	± 0.5%	0 – 12 % v/v
CO_2	± 1%	0 – 20 % v/v
O_2	± 1%	0 – 25 % v/v
THC	± 10%	0 – 50000 ppmC
CH_4	± 5%	0 – 500 ppmC
NOx	± 10%	0 – 10000 ppm

The exhaust emissions of nitrogen oxides (NOx), unburned total hydrocarbons (THC), carbon monoxide (CO), and carbon dioxide (CO_2) emissions for the EGR sweep and fuel types were analyzed. All tested fuels show close results of NOx (ppm) emission. Figure 5.7 shows the reduction of NOx (ppm) emission with increasing EGR dilution. The NOx emission was reduced due to lower combustion temperature.

The indicated specific nitrogen oxides (ISNOx) emission was calculated for selected fuels. The instantaneous fuel flow rate for gasoline and E80 ethanol blend fuels was measured using a Micro

Motion Coriolis flowmeter. However, the methane fuel flow is measured before and after the test using the displaced bubble method. The methane fuel cylinder is directly connected to the pre- and main chamber injector, and the high pressure inside fuel cylinders drives the fuel to the engine cylinder. The fuel flow rate is measured using the displaced bubble method by injecting fuel inside a displaced bubble with the same injection pulse width and measuring the injected fuel volume. Measuring instantaneous methane flow rate is not possible using the displaced bubble method; the EGR sweep test takes more than 30 minutes, and the compressed fuel cylinder pressure will not be the same before and after the EGR sweep test. Making displaced bubble tests after each EGR sweep is not economical time-wise; removing both injectors from the engine and connecting to the displaced bubble test takes much time. For gasoline and E80 ethanol blend fuels, ISNOx was calculated at each EGR sweep point. For methane fuel, only a high EGR rate was calculated using the instantaneous fuel and exhaust mass flowrate. Figure 5.8 shows indicated specific NOx emission with EGR sweep. At high EGR dilution, NOx emissions fall below 1.0 g/kWh and maintain a stable value of around 0.25 g/kWh above 40% EGR for gasoline and E80 ethanol blend fuels. These emissions fall below 1.0 g/kWh above 35% EGR for methane fuel.

The NOx emission compared with zero EGR dilution rate. In the previous study, the engine was equipped with interchangeable Jetfire® and SI cartridges was tested at 6 bar and 10 bar loads at 1500 rpm [33]. The SI cartridge with no EGR dilution at 10 bar engine load the NOx emission was 14.62 g/kWh. The high EGR dilution rate reduce the NOx emission by 93.2% at 35% dilution rate and reduced by 98.3% at 40% dilution rate.

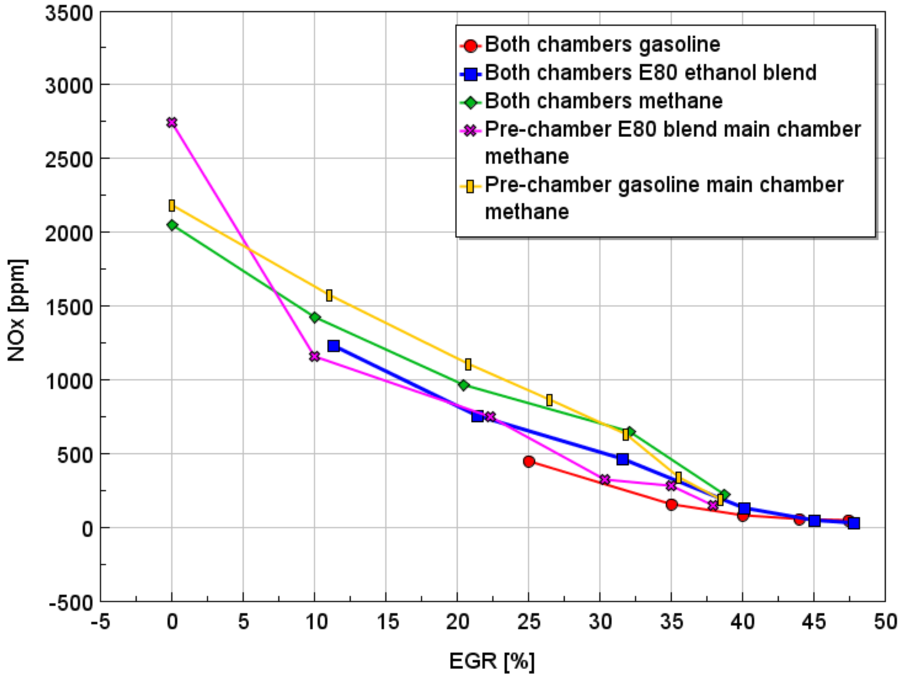

Figure 5.7 *Effect of EGR sweep and different alternative fuels on NOx emissions*

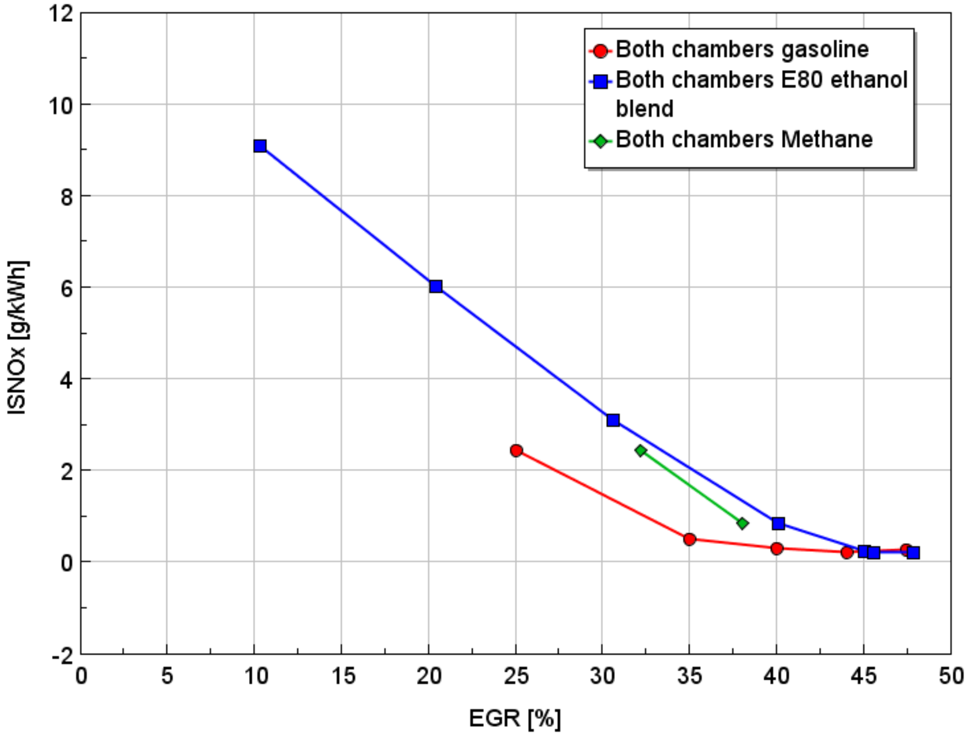

Figure 5.8 *Indicated specific NOx emission with EGR sweeps for gasoline, E80 ethanol blend, and methane fuels.*

Similarly, Figure 5.9 shows the total hydrocarbon emissions at each EGR sweep point. Generally, the hydrocarbon emissions increased with EGR dilution due to reduced combustion temperature and increased cyclic variation. Moreover, low combustion temperature increased the probability of wall quenching, thereby leading to more unburned THC emissions.

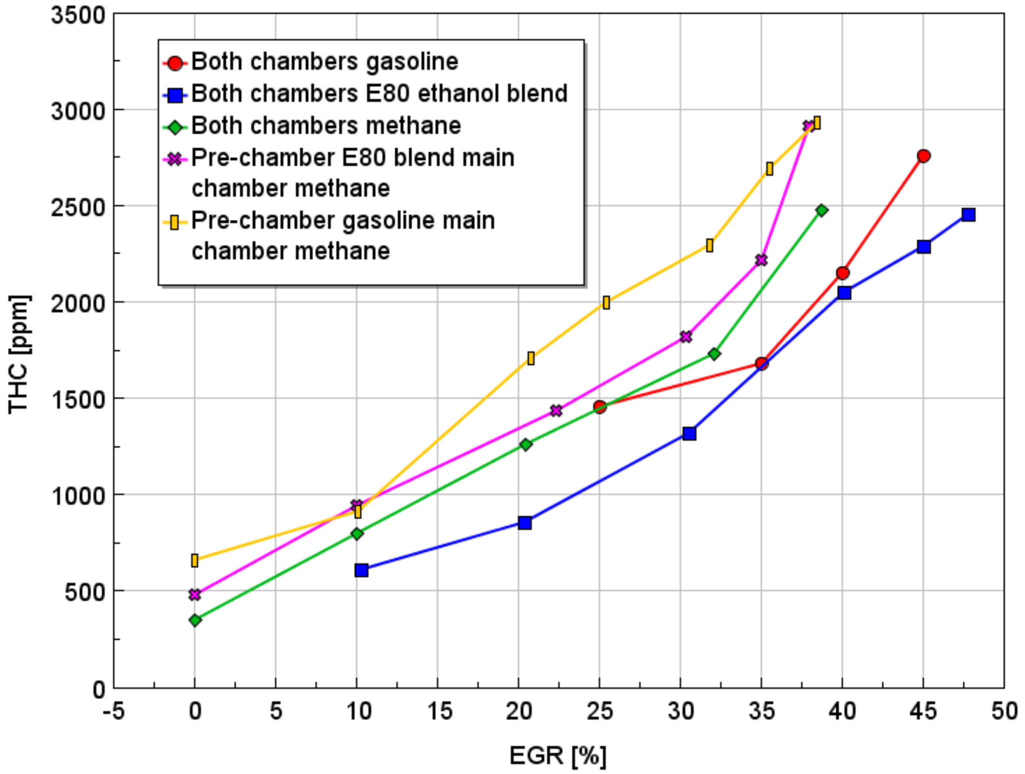

Figure 5.9 *Effect of EGR sweep and different alternative fuels on THC emissions*

Figure 5.10 shows the specific total hydrocarbon emissions of gasoline, E80 ethanol blend, and methane fuels. The total hydrocarbon emissions from ethanol are higher for high EGR dilution rates than the other tested fuels, and methane is relatively lower; gasoline emission is between the two fuels for high EGR dilution. These results could be significantly improved by optimization of the ignition jet geometry.

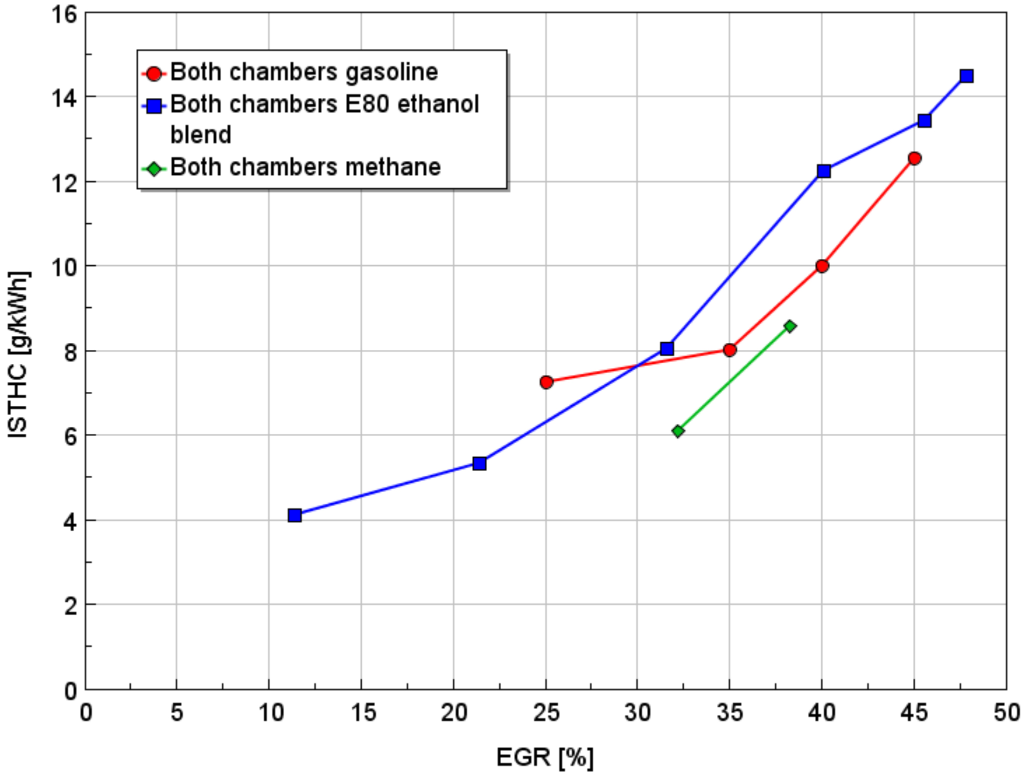

Figure 5.10 *Indicated specific THC emission with EGR sweeps for gasoline, E80 ethanol blend, and methane fuels*

The CO_2 and CO emission are not significantly affected by the EGR sweep. However, each fuel has a different emission level. The average CO_2 emission values of each fuel are shown in Figure 5.11. The average CO_2 emission for gasoline fuels is 14.51 Vol%. Considering gasoline fuel CO_2 emission as a reference, E80 ethanol blend fuel produces 4.5% less CO_2 emission with an average value of 13.9 Vol%. In the pre-chamber gasoline main chamber methane dual-fuel produces 25.2% less CO_2 emission with an average value of 10.9 Vol%. In the pre-chamber E80 blend main chamber, methane dual-fuel produces 26.7% less CO_2 emission with an average value of 10.63 Vol%. Methane fuel produces a small amount of CO_2 emission with an average value of 10.46 Vol%. Compared to gasoline fuel, methane fuel produces 27.9% less CO_2 emission for the condition studied.

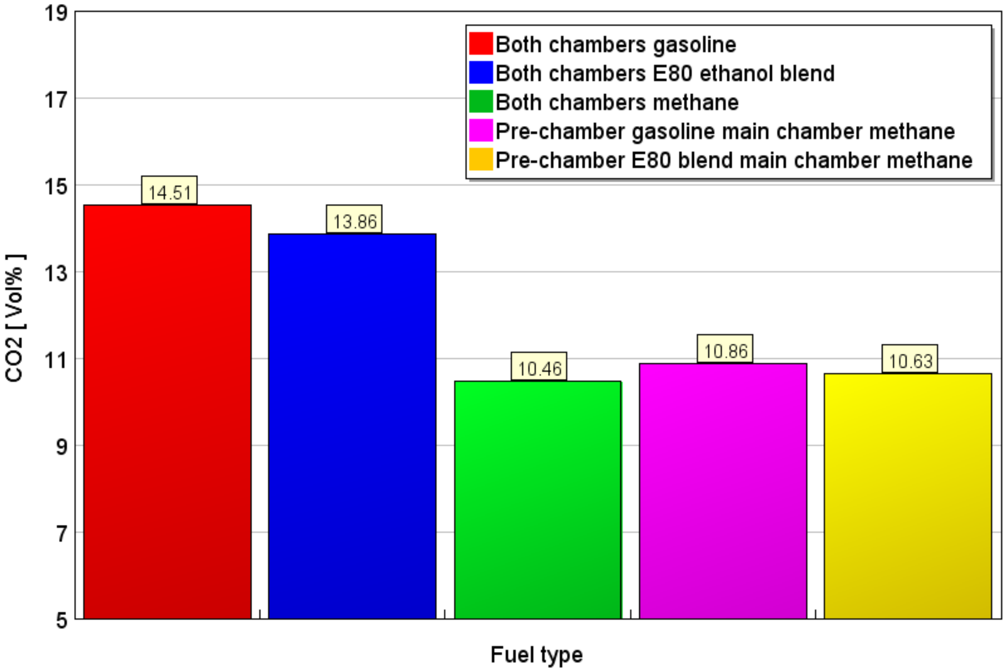

Figure 5.11 *The average CO2 emission of different fuels injected in in a DM-TJI engine*

Figure 5.12 shows the average CO emission value of each fuel combination. Similarly, gasoline fuel has the highest CO emission values with an average of 0.299 Vol%. Considering gasoline CO emission as a reference, E80 ethanol blend fuel produces 25.8% less CO emission with an average of 0.222 Vol%. In the pre-chamber gasoline main chamber, methane dual-fuel produces 46.5% less CO emission with an average of 0.16 Vol%. In the pre-chamber E80 blend main chamber methane dual-fuel produces 49.2% less CO emission with an average of 0.152 Vol%, and methane fuel produces 57.9% less CO emission with an average of 0.126 Vol%.

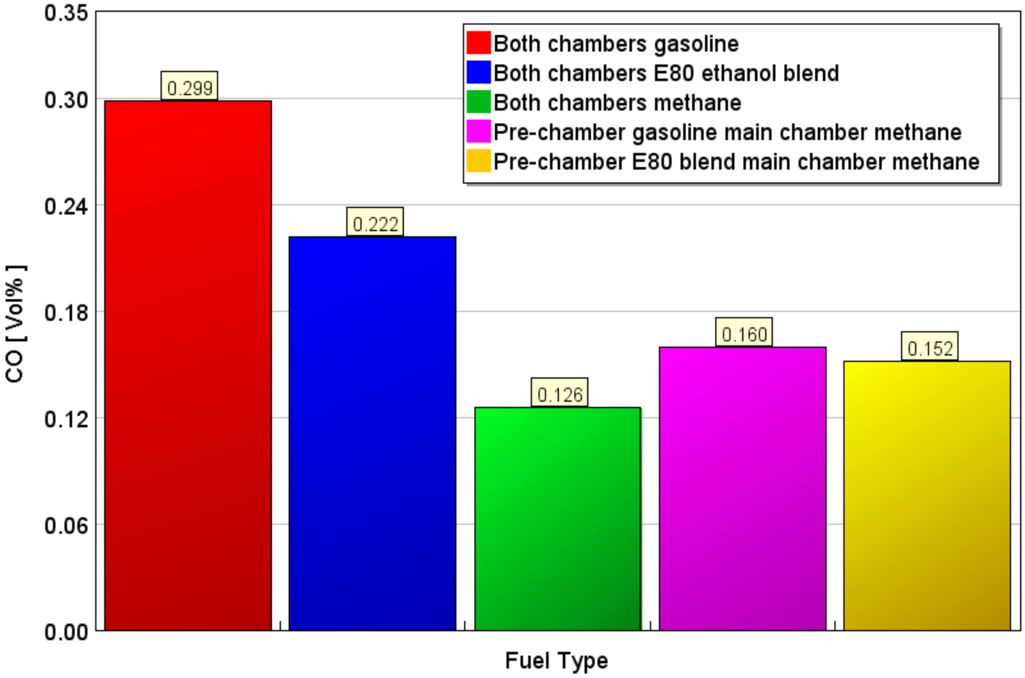

Figure 5.12 *The average CO emission of different fuel combination injected in a DM-TJI engine*

5.3.2 Burn Duration Cycle-to-cycle Variation and Engine Efficiency

5.3.2.1 Burn Duration Cycle-to-cycle Variation

The burn duration cycle-to-cycle variation for each experimental data point gradually increases along with the EGR dilution rate, as reported in the paper [122]. Since the dual-fuel type injection with methane has close results, the study focused on the three fuel types injected in both chambers (gasoline, E80 ethanol blend, and methane). The engine cycle-to-cycle variation shows the knock and the misfire limits of the operating condition.

The maximum cycle-to-cycle variation was compared at the fuel maximum EGR limit and high load with boosted conditions at engine IMEP of 10±0.5 bar and engine speed 1500rpm. Figure

5.13 shows the main chamber 200 cycle burn duration of 1090 CAD using gasoline fuel (a), methane fuel (b), and E80 ethanol blend fuel in both chambers at their maximum EGR dilution limit.

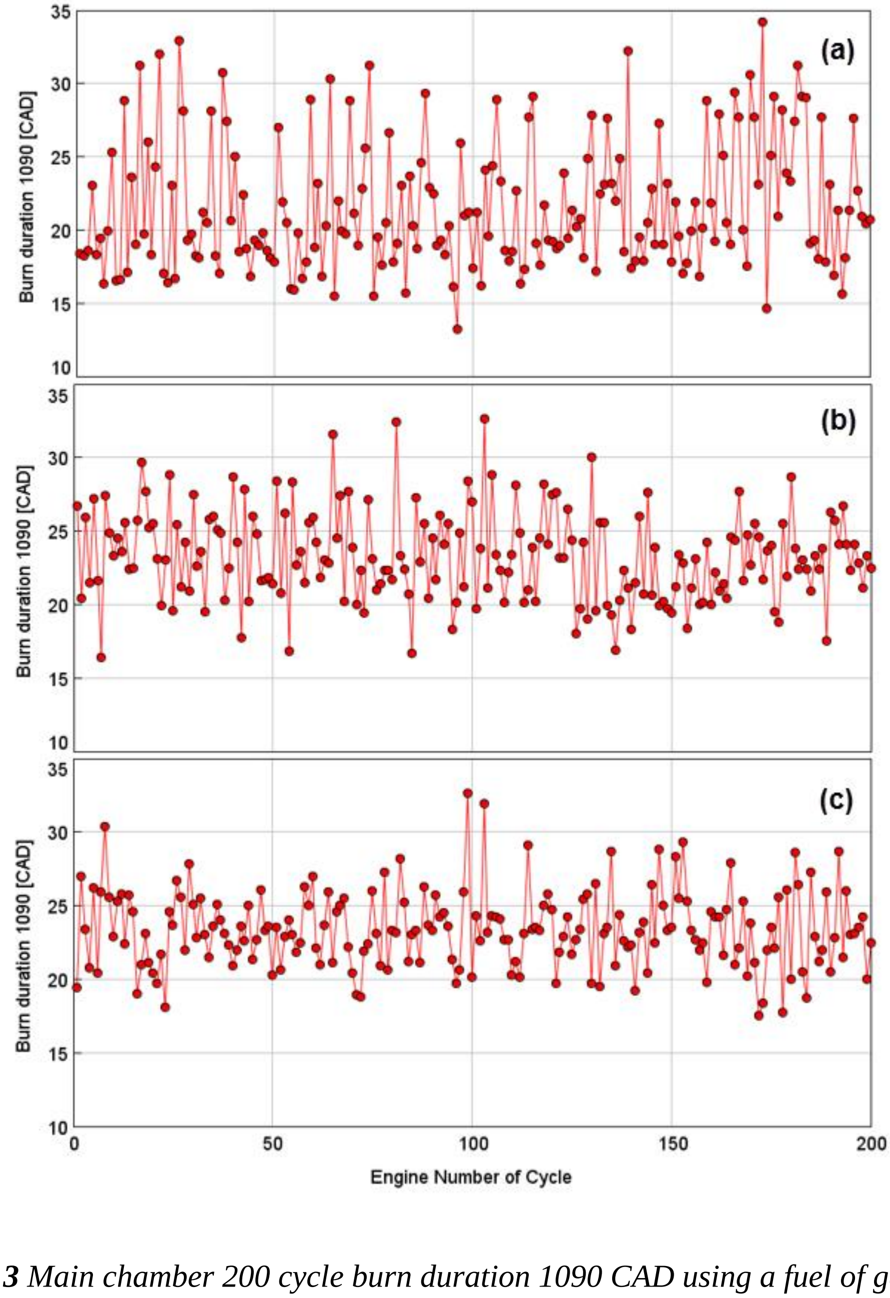

Figure 5.13 *Main chamber 200 cycle burn duration 1090 CAD using a fuel of gasoline (a), methane (b), and E80 ethanol blend (c) at 10±0.5 bar IMEPg.*

Figure 5.14 shows the three fuels' average burn duration and cycle-to-cycle variation as indicated by standard variation bars. Gasoline fuel experiences an average shorter burn duration of 21.58 CAD; however, the cycle-to-cycle variation is higher than the two fuels, with a standard deviation of 4.39. Methane and E80 ethanol blend have a close burn duration of 23.27 and 23.37, respectively. E80 ethanol blend has a lower cycle-to-cycle variation with a 2.62 standard deviation.

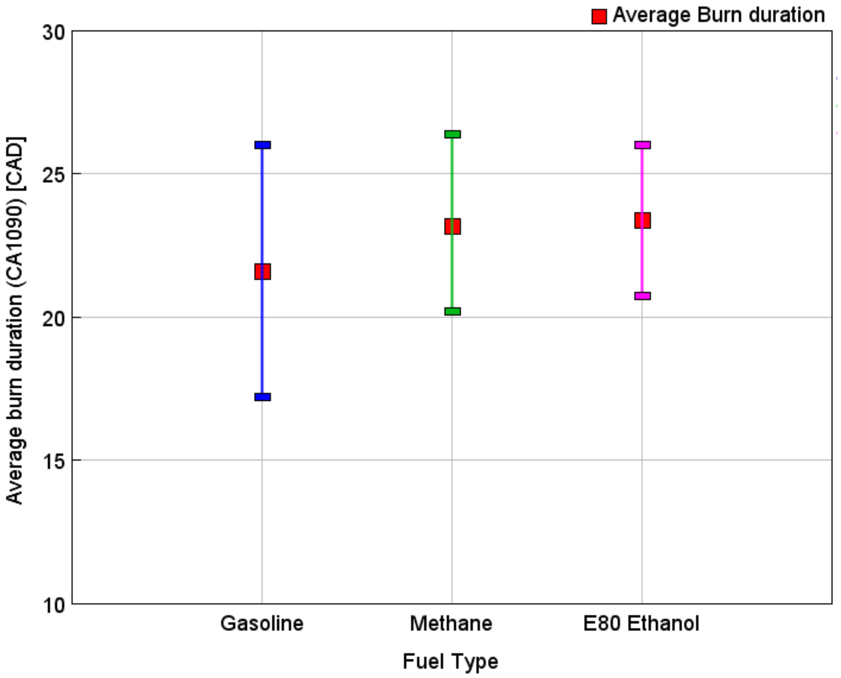

Figure 5.14 *The average burn duration and standard deviation cycle-to-cycle variation of the three fuels at the maximum EGR limit.*

5.3.2.2 Engine Efficiency

The engine gross indicated efficiency is compared for the three fuels at 8±0.5 bar IMEPg and 1500 rpm engine speed. As shown in Figure 5.15, the E80 ethanol blend fuel has the highest indicated efficiency of 45.61% with 45% EGR dilution. Since ethanol can operate with adequate combustion stability, lower burn duration cycle-to-cycle variation, and knock-free across a wide range of EGR dilution, the gross indicated efficiency is maintained above 44% starting from 35% EGR. Due to knock sensitivity and retarded spark timing, the gross indicated efficiency of gasoline is considerably lesser than those two fuels; the maximum indicated efficiency is 44.12% at 45% EGR dilution. The efficiency of methane fuel is calculated only for the peak EGR dilution rate. After measuring the pre- and main chamber injection volumes using a displaced bubble and considering the density of methane at 0^{o}C temperature 1atm pressure, the injection mass flow rate was calculated, and the maximum indicated efficiency of 45.03% with 38.5% EGR dilution was obtained.

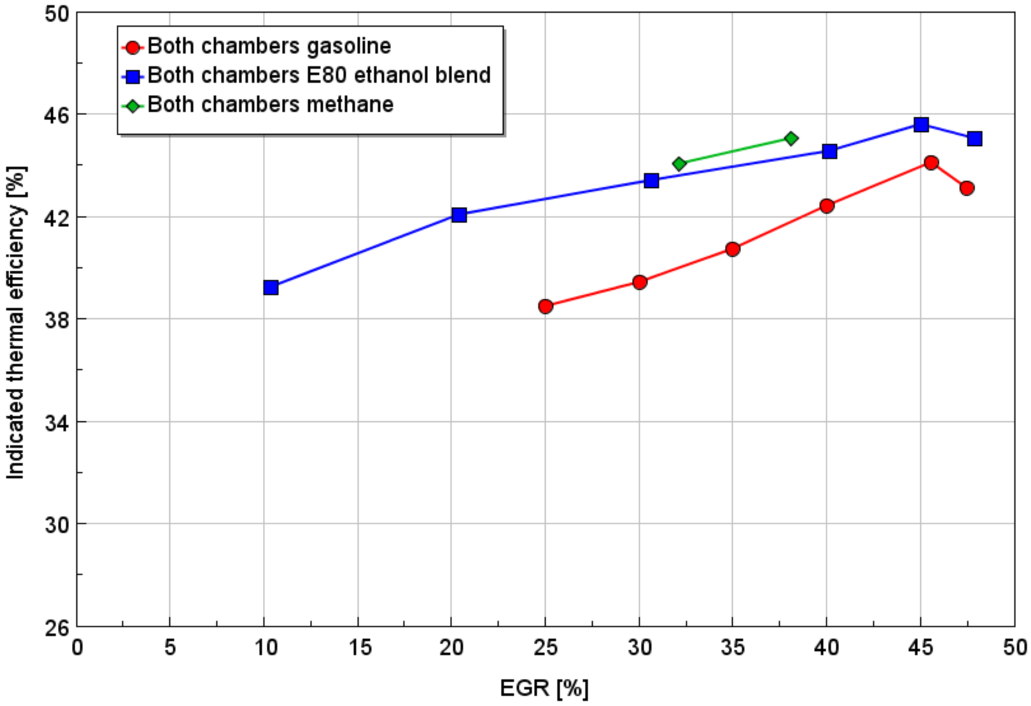

Figure 5.15 *Gross indicated efficiency of DM-TJI engine working with E80 ethanol blend, methane and gasoline fuels*

5.3.3 Engine Speed Variation Impact on Combustion Parameters and Exhaust Emissions

The effect of engine speed using the three different fuel types on the DM-TJI engine performance was examined at 1500, 1750, 2000, and 2300 rpm engine speeds. The engine loads were maintained the same for all engine speeds, whereas the fuel injection duration was varied to maintain the combustion stoichiometric condition at MBT spark timing.

5.3.3.1 Maximum EGR Dilution Rate

The effects of engine speeds on the EGR dilution limit using gasoline, E80 ethanol, and methane fuels are shown in Figure 5.16. The EGR dilution rate decreased by a small percentage with increasing engine speed. At the lowest engine speed, the maximum EGR dilution rate for gasoline and E80 ethanol fuel was 47%, and for methane 38%, with $COV_{IMEP} < 3\%$. At the highest engine speed, the dilution rate decreased to 44% for gasoline, 40% for E80 ethanol, and 30% for methane.

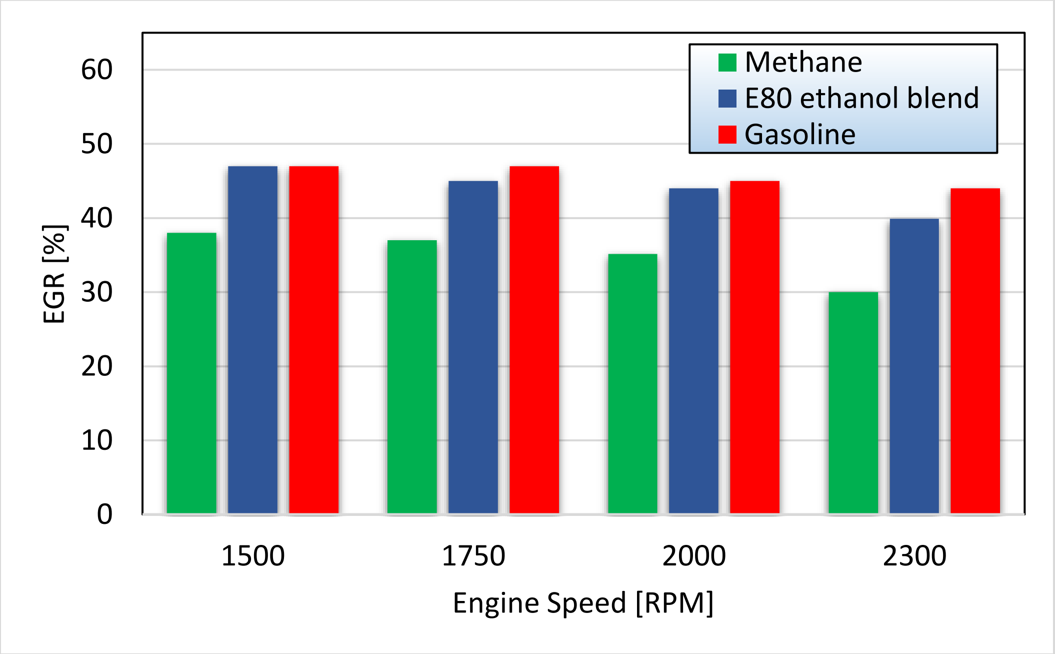

Figure 5.16 *Comparison of EGR dilution limit of DM-TJI engine between different engine speeds (1500, 1750, 2000 and 2300 rpm) with different alternative fuels*

The primary reason for the marginal decrease of EGR dilution rate with higher engine speed is that the residual gas mass fraction in the pre-chamber could be higher due to reduced scavenging by the auxiliary air charge at high engine speed. When the engine speed increases, the auxiliary air opening valve time decreases, which reduces the amount of pre-chamber air supply.

5.3.3.2 Combustion Duration

Figure 5.17 present the effect of different engine speeds on flame initiation (CA0010) and burn duration (CA1090) for different fuels. When the engine speed increases, the flame initiation, and burn duration also increase. The rate of flame initiation change has a lower slope than the burn duration as shown in the figure. The engine speed effect on burn duration is similar for all three fuel types. This also shows the importance of optimizing the reacting jet geometry.

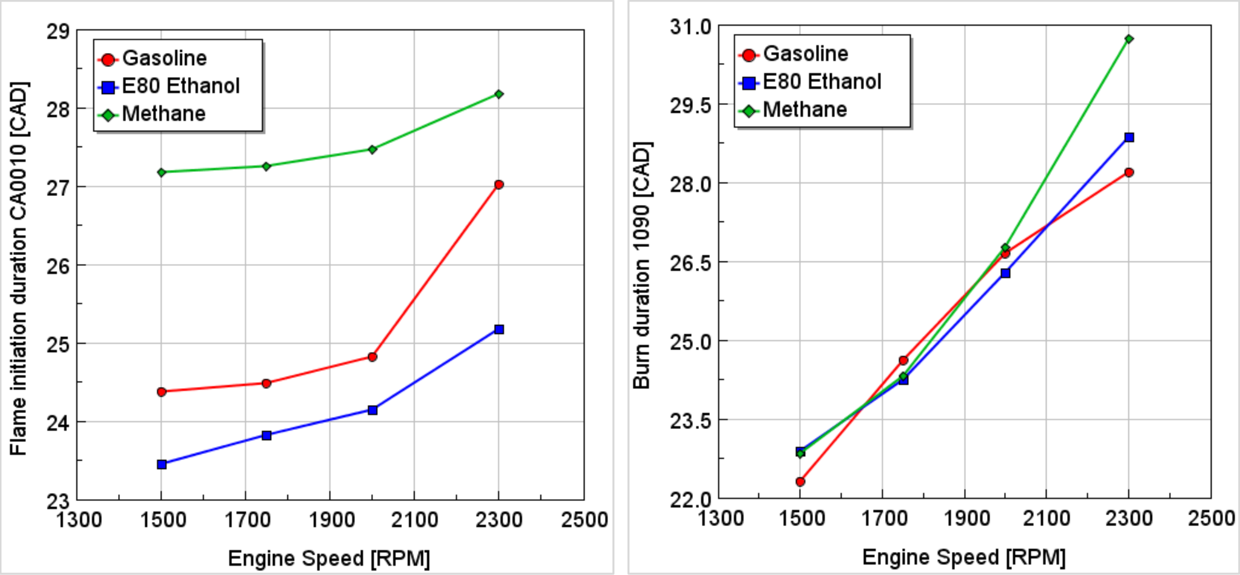

Figure 5.17 *Different fuel combustion durations of CA0010 (left) and Burn1090 (right) in a DM-TJI engine at different engine speed*

5.3.3.3 Emission

The exhaust emissions (NOx and THC) at different engine speeds are presented in Figure 5.18. The NOx emission for gasoline and E80 ethanol blend fuel was not affected by the engine speed; the result is similar for both fuels, and it is under 50 ppm. The methane fuel NOx emission increased with engine speed; the main cause for the increased NOx emission at high engine speed is the methane fuel EGR limit. Compared to other tested fuels, methane EGR limit is lower at high speed, and that leads to high NOx emission. Hydrocarbon emissions remain the same at both end engine speeds; in between engine speeds, a small value variation is shown.

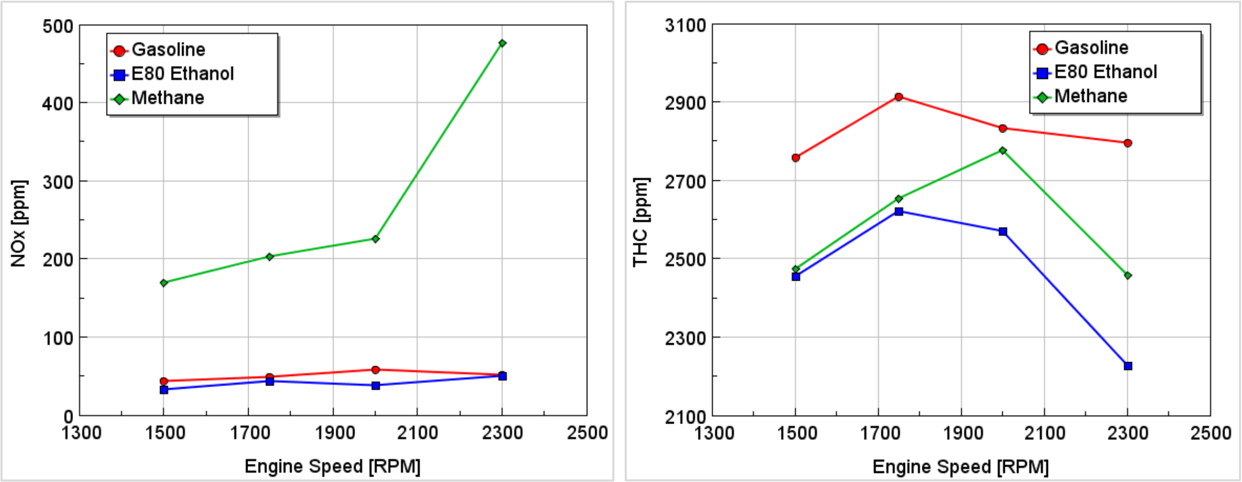

Figure 5.18 *Exhaust emission variation along with engine speed for different fuel in a DM-TJI engine. NOx emission (left) and THC emission (right).*

Spark timing affects NOx emission; advanced spark timing increases the engine's temperature, and high temperature increases NOx formation. Figure 5.19 shows the raw data result of spark advance timing Vs. NOx and THC emission for 45% EGR diluted combustion at an engine speed of 1500 rpm and engine load of 10 bar. As shown in Figure 5.19 (left), the NOx emission increases almost linearly with the spark advance timing from 25 ppm to 77ppm. However, THC emission was not affected significantly by the spark timing; the emission value was distributed between 2137 ppm to 2566 ppm.

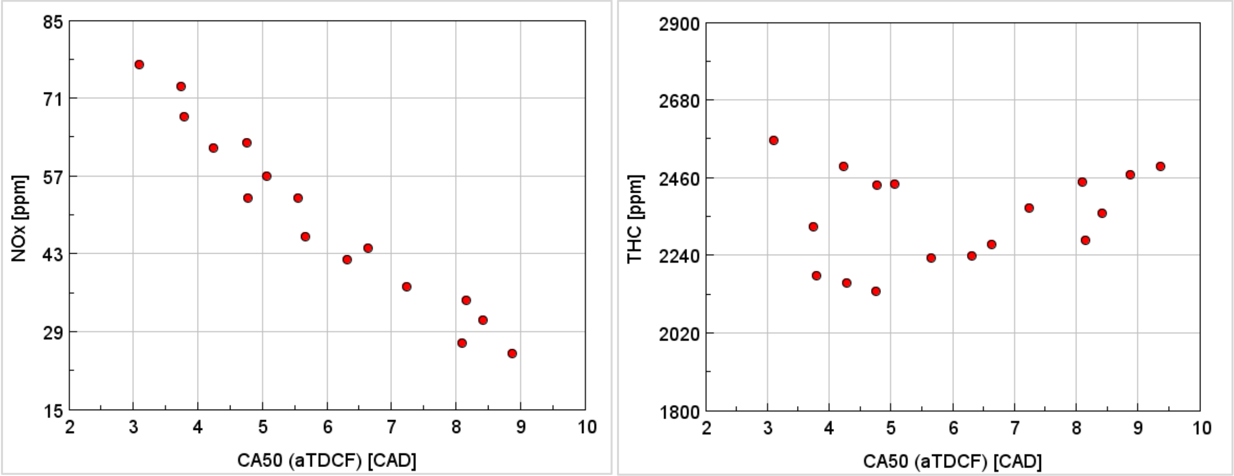

Figure 5.19 *Spark timing sweep result of NOx and THC emission for 45% EGR diluted combustion at engine speed 1500 rpm and engine load 10bar.*

5.4 Summary and Conclusion

This chapter studies the single-cylinder DM-TJI metal engine performance under different alternative fuels. The engine is equipped with a pre-chamber Jetfire® cartridge that contains the conventional spark plug, fuel injector, and auxiliary air valve. The engine head has a pent roof head modified to incorporate the pre-chamber Jetfire® cartridge and air valve driving assembly. An experimental test was carried out at stoichiometric conditions with different fuels, engine speed, engine load, and EGR dilution rates. The engine was equipped with standard test setup equipment and measurement instruments. Two data acquisition systems were used: high-frequency and low-frequency data sets. The results of the experimental investigation and the data analysis are summarized as follows.

- All tested alternative fuels burn in the single-cylinder DM-TJI metal engine without any significant modification to the engine.
- EGR sweep was conducted on all tested alternative fuels, and it shows high EGR dilution tolerance with combustion stability below 3%.
- E80 ethanol blend and methane fuel show less knock sensitivity at different EGR dilution rates compared to gasoline fuel. Methane fuel performs under the knock limit from no EGR dilution until the EGR dilution limit is reached. An E80 ethanol blend in both chambers operates under the knock limit starting from 10% EGR dilution up to the dilution limit. Gasoline fuel performed under the knock limit after 25% EGR dilution.
- EGR diluted combustion shows a decreased heat release rate on all tested alternative fuels, which provides better combustion phasing, leading to higher cylinder pressure and less knock sensitivity.
- Methane fuel in both chambers or combined with other tested fuel has an EGR dilution tolerance of 38% with COVIMEP < 3%. An E80 ethanol blend has stable combustion up to 47% EGR dilution, while the gasoline enabled 45% EGR rate before combustion became unstable.
- Methane fuel in the main chamber or both chambers shows the most extended delay on flame initiation compared to other fuels. The E80 ethanol blend fuel has a small flame initiation angle, while gasoline fuel result is in the range of the two fuel types.

- The burn duration for each fuel type increased as the EGR dilution rate increase. Methane fuel shows the longest combustion duration among the fuels studied for a given EGR dilution rate. The shorter burn durations are achieved by E80 ethanol blend fuel.

- NOx emission is reduced with increasing EGR dilution. All tested fuels show close results of NOx emission at a high EGR dilution rate. NOx emissions fall below 1.0 g/kWh. Compare to SI cartridge with no EGR dilution, the NOx emission reduced by 93.2% at 35% dilution rate and reduced by 98.3% at 40% dilution rate.

- E80 ethanol blend fuel produces 4.5% less CO2 emission compared to gasoline fuel at the same speed and load. In the pre-chamber E80 blend and in the main chamber methane dual-fuel produce 26.7% less CO2 emission. Methane fuel produces 27.9% less CO2 emission. In the pre-chamber gasoline and in the main chamber methane dual-fuel produce 25.2% less CO2 emission.

- Compared to gasoline fuel at the same speed and load, E80 ethanol blend fuel produces 25.75% less CO emission. In the pre-chamber gasoline and in the main chamber methane dual-fuel produces 46.5% less CO emission. In the pre-chamber E80 blend and in the main chamber methane dual-fuel produce 49.2% less CO emission, and methane fuel produces 57.9% less CO emission.

- At maximum dilution rate, gasoline fuel experiences higher cycle-to-cycle variation than the two fuels, with a standard deviation of 4.39. E80 ethanol blend has a lower cycle-to-cycle variation with a 2.62 standard deviation.

- The E80 ethanol blend has the highest indicated efficiency of 45.61% with 45% EGR dilution. Methane fuel has a maximum indicated efficiency of 45.03% with 38.5% EGR dilution. Due to knock sensitivity and retarded spark timing, gasoline fuel has a maximum indicated efficiency of 44.12% at 45% EGR dilution.

- At 1500 rpm engine speed, the maximum EGR dilution rate for gasoline and E80 ethanol fuel was 47% and for methane 38% with COVIMEP < 3%, at the highest engine speed of 2300 rpm, the dilution rate decreased to 44% for gasoline, 40% for E80 ethanol, and 30% for methane.

Chapter 6: Conclusion and Recommendation

6.1 Concluding Remarks

The internal combustion engine is still expected to be part of the powertrain in the following decades. Key technologies are being developed. These include further improving engine efficiency, advanced after-treatment systems, low carbon fuels, and hybrid gasoline engine strategies. The main obstacle in improving the thermal efficiency of the SI engine is combustion knock, reducing the ability of an engine operating at a high compression ratio. Advanced combustion strategies mitigate engine knock, improve the fuel economy of internal combustion engines and reduce CO2 emissions. Burning air-fuel mixtures highly diluted with exhaust gases can improve engine efficiency and fuel consumption through reduced heat loss due to lower in-cylinder temperature and high knock resistance. The Dual Mode, Turbulent Jet Ignition (DM-TJI), or the Jetfire® ignition system with additional auxiliary air supply to the pre-chamber enables a high compression ratio engine with high EGR dilution tolerance to improve engine fuel economy and CO2 emission.

In this dissertation, a single-cylinder high compression ratio DM-TJI metal engine was tested at different engine speeds. The result demonstrates that EGR diluted mixture at stoichiometric conditions with stable combustion improves engine efficiency. Pre-chamber orifice diameters were examined at different engine speeds and showed performance variation. A numerical combustion model was developed using GT-Power tools to create an engine performance map in a four-cylinder boosted configuration under highly dilute conditions. A full vehicle powertrain model was developed and calibrated with tested vehicle data. The DM-TJI engine map was replaced on the calibrated vehicle powertrain, and the fuel economy and CO2 emission were studied at different EPA drive cycles.

The DM-TJI engine demonstrates 10.5 - 17.29% fuel economy improvement and 9.51 - 14.75% CO2 emissions reductions over the tested drive cycles compared to the same vehicle components of the Ford F-150 2.7-Liter EcoBoost® engine. The NOx emission was reduced to below 2.5 g/kWh for the wide engine operating points. The DM-TJI vehicle was upgraded to a mild and parallel hybrid powertrain for further fuel economy improvement. The simulation demonstrates 9.23% and 29.88% improvement, respectively, compared to the conventional DM-TJI powertrain.

The DM-TJI metal engine fuel flexibility was studied with E80 ethanol blend and methane fuels under single and dual fuel injections. The tested alternative fuels perform well at different EGR dilution rates with a maximum indicated efficiency of 45.61% and 45.03%, respectively. Compared to gasoline fuel, CO2 and CO emissions were reduced by 4.47% and 25.75% for the E80 ethanol blend and 27.91% and 57.85% for methane fuel. At maximum dilution rate, gasoline fuel experiences higher cycle-to-cycle variation than the two fuels, and the E80 ethanol blend has a lower cycle-to-cycle variation.

6.2 Recommendations for Future Work

The current analysis showed the value of DM-TJI engine for future combustion applications. The current study focused on the engine's performance with the existing valve timing, which is fixed timing. However, a broader test matrix at different intake, exhaust, and pre-chamber air valve-timing should be done for the different engine speeds to maximize the engine benefit and valve timing optimization. At higher engine speeds, the pre-chamber air supply benefits from variable valve timing to make enough air purge in the pre-chamber. The main and pre-chamber fuel are injected with the same pressure from the same supply line; the pre-chamber injection pressure would be better investigated separately for pre-chamber combustion optimization.

The pre-chamber orifice diameter was analyzed at various engine speeds for the three selected orifice diameters. Each orifice diameter shows an advantage on the tested engine speed. Further research and optimization are required for the pre-chamber nozzle orifice orientation, orifice length to diameter ratio, and pre-chamber shape and volume.

The DM-TJI engine would be a good choice for hybrid powertrain vehicles. The simulated model shows better fuel economy and CO2 emission reduction than the conventional powertrain. The implemented rule-based hybrid control algorithm performs better in switching between the engine and electric motor; charging and discharging battery depend on the battery state of charge. However, the control algorithm needs further optimization to select engine operating points and keep the engine operating at a high-efficiency point.

Fuel flexibility was studied using E80 ethanol blend and methane fuel; both fuels perform stable combustion with a high EGR dilution rate. A methane fuel injector in the pre-chamber was testes with the same injector used for gasoline fuel. Due to lack of lubrication, the injectors start to leak after methane fuel is injected for a while, which affects the EGR tolerance and combustion stability. A specific pre-chamber fuel injector for methane fuel is required to harvest the maximum fuel performance. The methane fuel delivery pipeline connects directly to the fuel injector from the compressed cylinders. Fuel flow rates were measured using the displace bubble method. Standard fuel flow rate and temperature measurement were required for methane fuel to determine the engine efficiency without introducing measurement error.

Methane and E80 ethanol blend fuel show knock-free combustion on 13.3:1 compression ratio at advanced spark timing. The engine performance will clearly accommodates an additional compression. The current experimental engine compression ratio cannot be further increased to examine the compression limit. The next DM-TJI engine prototype should adopt an additional compression ratio to investigate the compression limit of the fuels and maximum fuel efficiency.

APPENDICES

APPENDIX A. Engine Map Data

Table A.1 *Brake thermal efficiency map data of DM-TJI engine with high EGR dilution*

Engine Speed [RPM]	BMEP [bar]	Efficiency [%]	Torque [Nm]
1000	2.3	17.0	35.4
1000	5.7	33.8	100.3
1000	9.0	37.3	158.1
1500	1.5	20.3	25.5
1500	3.6	31.4	63.4
1500	5.0	34.6	88.5
1500	6.2	34.8	109.5
1500	7.3	37.3	128.3
1500	7.6	37.2	140.0
1500	7.9	38.8	152.8
1500	8.7	39.0	152.8
1500	10.9	39.2	192.4
1500	14.1	40.5	248.2
1500	15.0	40.0	264.2
1500	15.8	39.2	276.9
2000	2.5	19.2	26.8
2000	6.0	34.8	105.6
2000	7.3	37.2	127.4
2000	9.3	38.9	163.4
2000	10.8	39.4	183.0
2000	13.9	40.6	243.4
2000	14.9	40.6	262.1
2000	15.7	40.4	275.1
2000	16.4	40.1	288.0
2000	16.8	39.9	296.0
2000	17.5	39.5	307.0
2000	18.9	38.1	331.7
3000	2.3	17.4	23.5
3000	6.1	34.0	107.9
3000	10.5	39.6	184.7
3000	13.9	40.9	243.6
3000	14.8	40.5	259.7
3000	15.6	40.3	274.3
3000	16.4	39.8	288.1
3000	17.7	39.4	311.5
3000	19.4	38.1	341.4
4000	3.0	18.0	23.6
4000	5.7	32.7	100.0
4000	6.5	32.7	114.2
4000	7.1	33.0	125.5
4000	9.2	35.7	162.3
4000	12.4	37.4	219.0
4000	13.6	37.6	238.7
4000	14.5	37.7	254.0
4000	15.3	37.7	268.9
4000	15.3	37.7	268.6
4000	16.4	37.5	289.0
4000	18.3	37.0	321.8

Table A.2 *BSFC map data of DM-TJI engine with high EGR dilution.*

Engine Speed [RPM]	Torque [Nm]	BSFC [g/kW-hr]	BMEP [bar]
1000	35.4	390.6	2.3
1000	100.3	255.2	5.7
1000	158.1	231.5	9.0
1500	25.5	387.9	1.5
1500	63.4	274.7	3.6
1500	88.5	250.0	5.0
1500	109.5	248.4	6.2
1500	128.3	231.8	7.3
1500	152.8	222.8	8.7
1500	192.4	221.4	10.9
1500	248.2	213.5	14.1
1500	264.2	215.8	15.0
1500	276.9	221.4	15.8
2000	26.8	387.9	2.5
2000	105.6	248.3	6.0
2000	127.4	232.4	7.3
2000	183.0	219.4	10.8
2000	243.4	212.8	13.9
2000	262.1	212.7	14.9
2000	275.1	213.8	15.7
2000	288.0	215.3	16.4
2000	296.0	218.8	16.8
2000	307.0	220.1	17.5
2000	331.7	227.8	18.9
3000	23.5	387.9	2.3
3000	107.9	254.1	6.1
3000	184.7	218.4	10.5
3000	243.6	211.1	13.9
3000	259.7	213.2	14.8
3000	274.3	214.3	15.6
3000	311.5	220.1	17.7
3000	341.4	228.9	19.4
4000	23.6	387.9	3.0
4000	100.0	264.5	5.7
4000	122.1	258.2	7.1
4000	139.1	248.3	8.0
4000	162.3	241.7	9.2
4000	219.0	230.8	12.4
4000	238.7	230.1	13.6
4000	254.0	229.3	14.5
4000	268.6	229.9	15.3
4000	289.0	230.9	16.4
4000	321.8	235.7	18.3

Table A.3 *The EGR dilution rate of the DM-TJI engine map data.*

Engine Speed [RPM]	BMEP [bar]	EGR [%]
1000	2.0	15.0
1000	5.7	40.0
1000	9.0	45.0
1500	1.4	15.8
1500	3.6	35.4
1500	5.0	40.0
1500	6.2	42.0
1500	7.3	45.0
1500	7.3	45.0
1500	8.0	45.0
1500	8.7	45.0
1500	10.9	45.0
1500	14.1	45.0
1500	15.0	40.0
1500	15.8	35.0
2000	1.5	15.0
2000	6.0	40.0
2000	7.3	45.0
2000	9.3	45.0
2000	10.8	45.0
2000	13.9	45.0
2000	14.9	43.0
2000	15.7	40.0
2000	16.4	38.0
2000	16.8	36.0
2000	17.5	35.0
2000	18.9	30.0
3000	2.3	15.0
3000	6.1	45.0
3000	10.5	45.0
3000	13.9	45.0
3000	14.8	43.0
3000	15.6	40.0
3000	16.4	38.0
3000	17.7	35.0
3000	19.4	30.0
4000	3.0	15.0
4000	5.7	35.0
4000	6.5	40.0
4000	7.1	45.0
4000	9.2	45.0
4000	12.5	45.0
4000	13.6	45.0
4000	14.5	40.0
4000	15.3	38.0
4000	15.3	35.0
4000	16.4	33.0
4000	18.3	30.0

APPENDIX B. Drive cycle engine operating points

Operating points over the DM-TJI engine fuel consumption equivalent CO2 emission (BSCO2 g/kW-hr) map in the different driving cycle.

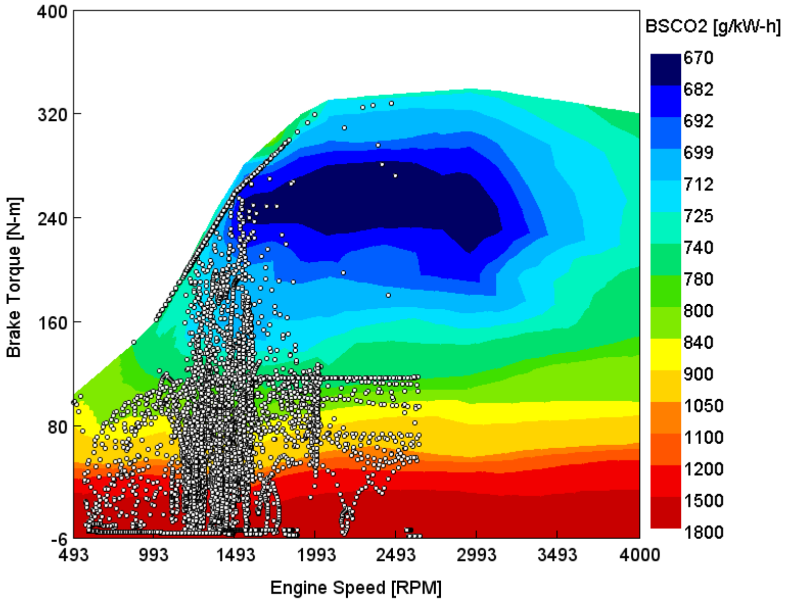

Figure B.1 *FTP city drive cycle.*

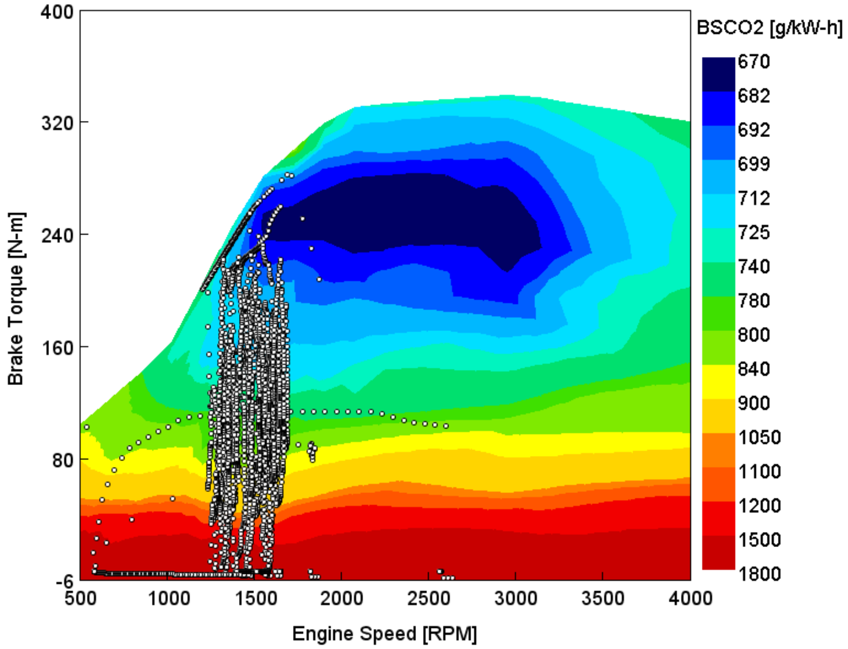

Figure B.2 *Highway drive cycle.*

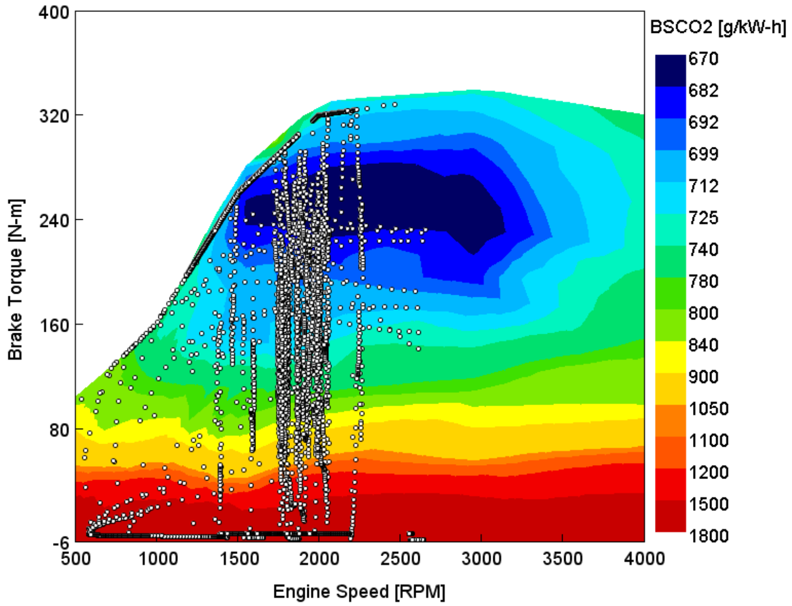

Figure B.3 *US06 drive cycle.*

DM-TJI operating points over the ISNOx (g/kW-hr) engine map for the different drive cycle

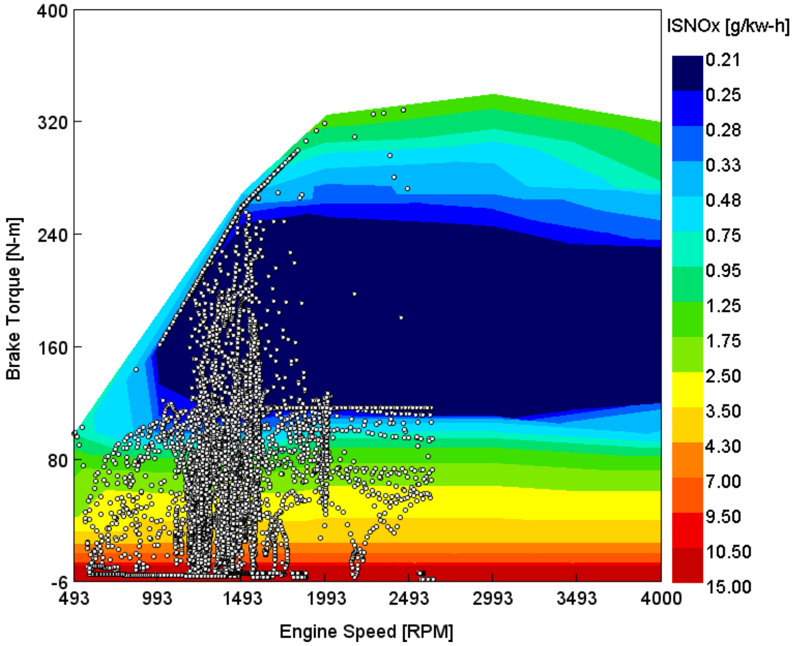

Figure B.4 *FTP city drive cycle.*

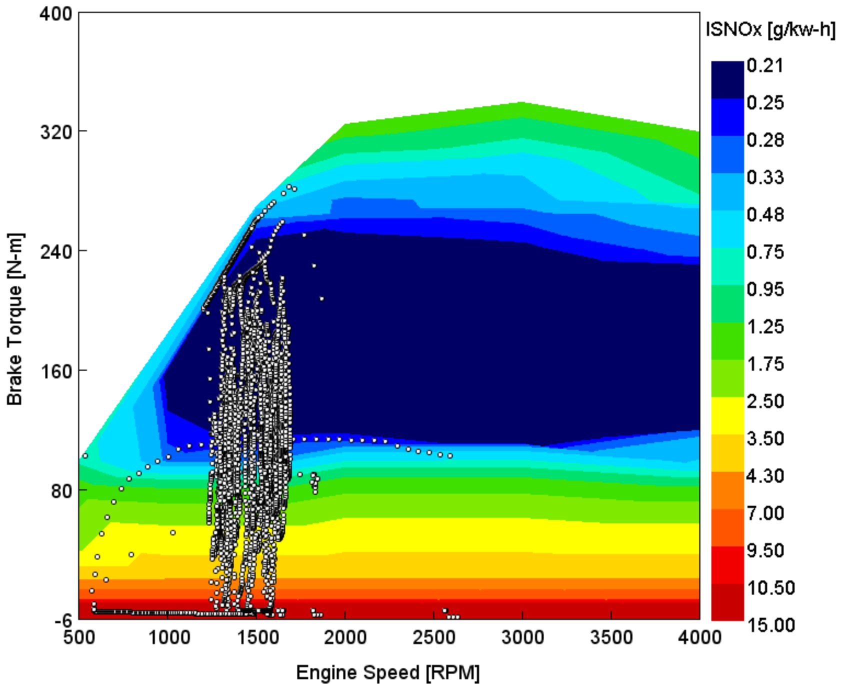

Figure B.5 *Highway drive cycle*

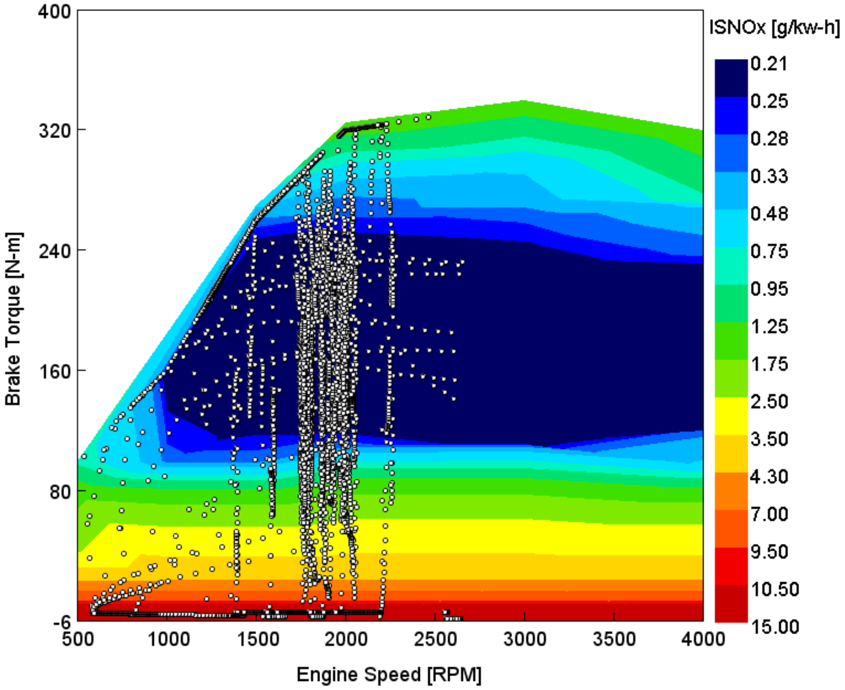

Figure B.6 *US06 drive cycle*

REFERENCES

REFERENCES

1. R. Folkson, Alternative fuels and Advanced vehicle technologies for improved environmental performance towards zero carbon transportation, n.d.

2. P. Moriarty, D. Honnery, Global Transport Energy Consumption, Altern. Energy Shale Gas Encycl. (2016) 651–656. https://doi.org/10.1002/9781119066354.ch61.

3. Global-Greenhouse-Gas-Emissions-Data @ Www.Epa.Gov, (n.d.). https://www.epa.gov/ghgemissions/global-greenhouse-gas-emissions-data#Sector.

4. the-number-of-cars-worldwide-is-set-to-double-by-2040 @ www.weforum.org, (n.d.). https://www.weforum.org/agenda/2016/04/the-number-of-cars-worldwide-is-set-to-double-by-2040.

5. J. Benajes, A. García, J. Monsalve-Serrano, S. Martínez-Boggio, Optimization of the parallel and mild hybrid vehicle platforms operating under conventional and advanced combustion modes, Energy Convers. Manag. 190 (2019) 73–90. https://doi.org/10.1016/j.enconman.2019.04.010.

6. J. Benajes, A. García, J. Monsalve-Serrano, S. Martínez-Boggio, Emissions reduction from passenger cars with RCCI plug-in hybrid electric vehicle technology, Appl. Therm. Eng. 164 (2020) 114430. https://doi.org/10.1016/j.applthermaleng.2019.114430.

7. A. Joshi, Review of vehicle engine efficiency and emissions, SAE Tech. Pap. 2019-April (2019) 734–761. https://doi.org/10.4271/2019-01-0314.

8. ICCT, 2017 Global update: Light-duty vehicle greenhouse gas and fuel economy standards, Icct. (2017) 36. http://www.theicct.org/sites/default/files/publications/2017-Global-LDV-Standards-Update_ICCT-Report_23062017_vF.pdf.

9. R. Folkson, Alternative fuels and Advanced vehicle technologies for improved environmental performance towards zero carbon transportation, in: Altern. Fuels Adv. Veh. Technol. Improv. Environ. Perform., Elsevier, 2014: pp. 1–15. https://doi.org/10.1533/9780857097422.1.

10. M. Melaika, S. Mamikoglu, P. Dahlander, 48V Mild-Hybrid Architecture Types, Fuels and Power Levels Needed to Achieve 75g CO 2 /km, SAE Tech. Pap. (2019) 2019-01–0366. https://doi.org/10.4271/2019-01-0366.Abstract.

11. Y.G. and E.A. Mehrdad Ehsani, Modern Electric, Hybrid Electric, and Fuel Cell Vehicles: Fundamentals, Theory, and Design, 2010. http://ieeexplore.ieee.org/document/5439044/.

12. N. Demirdoven, Hybrid Cars Now, Fuel Cell Cars Later, Science (80-.). 305 (2004) 974–976. https://doi.org/10.1126/science.1093965.

13. Y. Huang, N.C. Surawski, B. Organ, J.L. Zhou, O.H.H. Tang, E.F.C. Chan, Fuel consumption and emissions performance under real driving: Comparison between hybrid and conventional vehicles, Sci. Total Environ. 659 (2019) 275–282. https://doi.org/10.1016/j.scitotenv.2018.12.349.

14. M.F. M. Sabri, K.A. Danapalasingam, M.F. Rahmat, A review on hybrid electric vehicles architecture and energy management strategies, Renew. Sustain. Energy Rev. 53 (2016) 1433–1442. https://doi.org/10.1016/j.rser.2015.09.036.

15. Z. Liu, A. Ivanco, Z.S. Filipi, Impacts of Real-World Driving and Driver Aggressiveness on Fuel Consumption of 48V Mild Hybrid Vehicle, SAE Int. J. Altern. Powertrains. 5 (2016). https://doi.org/10.4271/2016-01-1166.

16. R. Romanato, F. Acquaviva, F. Duma, R. Fuso, A. Tripodi, L. Passilly, M. Vieracker, 48 v Hybrid System Technologies to Develop the Most Efficient and Cleanest Diesel, SAE Tech. Pap. 2018-May (2018). https://doi.org/10.4271/2018-37-0011.

17. A. Rudge, R. Guilherme, Simulation of the fuel consumption reduction potential of a mild hybrid system applied to a popular flexible fuel vehicle, SAE Tech. Pap. (2012). https://doi.org/10.4271/2012-36-0516.

18. S. Lee, J. Cherry, M. Safoutin, A. Neam, J. McDonald, K. Newman, Modeling and Controls Development of 48 v Mild Hybrid Electric Vehicles, SAE Tech. Pap. 2018-April (2018) 1–15. https://doi.org/10.4271/2018-01-0413.

19. F. Millo, M. Badami, C. V. Ferraro, L. Rolando, Different hybrid powertrain solutions for European diesel passenger cars, SAE Int. J. Engines. 2 (2010) 493–504. https://doi.org/10.4271/2009-24-0064.

20. R. Bao, V. Avila, J. Baxter, Effect of 48 v Mild Hybrid System Layout on Powertrain System Efficiency and Its Potential of Fuel Economy Improvement, SAE Tech. Pap. 2017-March (2017). https://doi.org/10.4271/2017-01-1175.

21. F. Millo, M. Badami, C. V. Ferraro, G. Lavarino, L. Rolando, A comparison between different hybrid powertrain solutions for an European mid-size passenger car, SAE Tech. Pap. (2010). https://doi.org/10.4271/2010-01-0818.

22. G.R. Gentz, E. Toulson, Experimental Studies of a Liquid Propane Auxiliary Fueled Turbulent Jet Igniter in a Rapid Compression Machine, SAE Int. J. Engines. 9 (2016). https://doi.org/10.4271/2016-01-0708.

23. W.P. Attard, E. Toulson, A. Huisjen, X. Chen, G. Zhu, H. Schock, Spark ignition and pre-chamber turbulent jet ignition combustion visualization, SAE Tech. Pap. (2012). https://doi.org/10.4271/2012-01-0823.

24. X. Li, W. Zhang, Z. Huang, D. Ju, L. Huang, M. Feng, X. Lu, Z. Huang, Pre-chamber turbulent jet ignition of methane/air mixtures with multiple orifices in a large bore constant volume chamber: effect of air-fuel equivalence ratio and pre-mixed pressure,

Front. Energy. 13 (2019) 483–493. https://doi.org/10.1007/s11708-019-0631-1.

25. C. Atis, S.S. Chowdhury, Y. Ayele, T. Stuecken, H. Schock, A.K. Voice, Ultra-Lean and High EGR Operation of Dual Mode, Turbulent Jet Ignition (DM-TJI) Engine with Active Pre-chamber Scavenging, in: SAE Int. J. Engines, 2020: pp. 2018-01–0329. https://doi.org/10.4271/2020-01-1117.

26. G. Gentz, B. Thelen, M. Gholamisheeri, P. Litke, A. Brown, J. Hoke, E. Toulson, A study of the influence of orifice diameter on a turbulent jet ignition system through combustion visualization and performance characterization in a rapid compression machine, Appl. Therm. Eng. 81 (2015) 399–411. https://doi.org/10.1016/j.applthermaleng.2015.02.026.

27. W.P. Attard, M. Bassett, P. Parsons, H. Blaxill, A new combustion system achieving high drive cycle fuel economy improvements in a modern vehicle powertrain, SAE 2011 World Congr. Exhib. (2011). https://doi.org/10.4271/2011-01-0664.

28. A.A. Validi, H. Schock, F. Jaberi, Turbulent jet ignition assisted combustion in a rapid compression machine, Combust. Flame. 186 (2017) 65–82. https://doi.org/10.1016/j.combustflame.2017.07.032.

29. W.P. Attard, H. Blaxill, A Gasoline Fueled Pre-Chamber Jet Ignition Combustion System at Unthrottled Conditions, SAE Int. J. Engines. 5 (2012) 315–329. https://doi.org/10.4271/2012-01-0386.

30. R.T. Vedula, G. Gentz, T. Stuecken, E. Toulson, H. Schock, Lean Burn Combustion of Iso-Octane in a Rapid Compression Machine Using Dual Mode Turbulent Jet Ignition System, SAE Int. J. Engines. 11 (2018) 3–11. https://doi.org/10.4271/03-11-01-0007.

31. R.T. Vedula, Optical Investigations and Efficiency Measurements of a Dual-Mode Turbulent Jet Ignition Engine Under Lean and High-Egr Near-Stoichiometric Conditions, (2016).

32. S. Tolou, EXPERIMENTS AND MODEL DEVELOPMENT OF A DUAL MODE, TURBULENT JET IGNITION ENGINE, 2019.

33. C.A.A. Atis, HIGH-EGR DILUTION ENABLED BY DUAL MODE, TURBULENT JET IGNITION (DM-TJI) FOR HIGH-EFFICIENCY INTERNAL COMBUSTION ENGINES, (2021) 10–27.

34. C.E.C. Alvarez, G.E. Couto, V.R. Roso, A.B. Thiriet, R.M. Valle, A review of prechamber ignition systems as lean combustion technology for SI engines, Appl. Therm. Eng. 128 (2018) 107–120. https://doi.org/10.1016/j.applthermaleng.2017.08.118.

35. Y. Huang, H. Wang, A. Khajepour, B. Li, J. Ji, K. Zhao, C. Hu, A review of power management strategies and component sizing methods for hybrid vehicles, Renew. Sustain. Energy Rev. 96 (2018) 132–144. https://doi.org/10.1016/j.rser.2018.07.020.

36. M.S. (eds. . Michael Günther, Ignition Systems for Gasoline Engines, in: Ignition Syst.

Gasol. Engines, 2017. https://doi.org/10.1007/978-3-319-45504-4.

37. A. Stadler, H. Sauerland, M. Härtl, G. Wachtmeister, The Potential of Gasoline Fueled Pre Chamber Ignition Combined with Elevated Compression Ratio, SAE Tech. Pap. 2020-April (2020) 1–12. https://doi.org/10.4271/2020-01-0279.

38. D. Serrano, J.M. Zaccardi, C. Müller, C. Libert, K. Habermann, Ultra-Lean Pre-Chamber Gasoline Engine for Future Hybrid Powertrains, SAE Tech. Pap. 2019-Septe (2019) 607–622. https://doi.org/10.4271/2019-24-0104.

39. F. Almatrafi, P. Hlaing, M. Echeverri Marquez, M. Ben Houidi, B. Johansson, Narrow-Throat Pre-Chamber Combustion with Ethanol, a Comparison with Methane, SAE Tech. Pap. i (2020) 1–15. https://doi.org/10.4271/2020-01-2041.

40. X. Yu, A. Zhang, A. Baur, N. Engineer, The Impact of Pre-Chamber Design on Part Load Efficiency and Emissions of a Miller Cycle Light Duty Gasoline Engine, SAE Tech. Pap. (2021) 1–16. https://doi.org/10.4271/2021-01-0479.

41. J. Benajes, R. Novella, J. Gomez-Soriano, I. Barbery, C. Libert, F. Rampanarivo, M. Dabiri, Computational assessment towards understanding the energy conversion and combustion process of lean mixtures in passive pre-chamber ignited engines, Appl. Therm. Eng. 178 (2020) 115501. https://doi.org/10.1016/j.applthermaleng.2020.115501.

42. John Heywood, John Heywood - Internal Combustion Engine Fundamentals-McGraw-Hill Education (2018), (2018). https://www.accessengineeringlibrary.com/content/book/9781260116106.

43. E. Toulson, H.J. Schock, W.P. Attard, A review of pre-chamber initiated jet ignition combustion systems, SAE Tech. Pap. (2010). https://doi.org/10.4271/2010-01-2263.

44. A.K. Oppenheim, Prospects for combustion in piston engines, SAE Tech. Pap. 111 (2002) 1707–1721. https://doi.org/10.4271/2002-01-0999.

45. A. Cooper, A. Harrington, M. Bassett, S. Reader, M. Bunce, Application of the Passive MAHLE Jet Ignition System and Synergies with Miller Cycle and Exhaust Gas Recirculation, SAE Tech. Pap. 2020-April (2020) 1–15. https://doi.org/10.4271/2020-01-0283.

46. J.R. Theis, A. Getsoian, C. Lambert, The Development of Low Temperature Three-Way Catalysts for High Efficiency Gasoline Engines of the Future, SAE Int. J. Fuels Lubr. 10 (2017). https://doi.org/10.4271/2017-01-0918.

47. H.M. Cho, B.Q. He, Spark ignition natural gas engines-A review, Energy Convers. Manag. 48 (2007) 608–618. https://doi.org/10.1016/j.enconman.2006.05.023.

48. H. Schock, G. Zhu, R. Stuecken, INTERNAL COMBUSTON ENGINE, Patent Application Publication, 1 (2014).

49. C. Atis, H. Schock, Comparison of Excess Air (Lean) vs EGR Diluted Operation in a Pre-Chamber Air/Fuel Scavenged Dual Mode, Turbulent Jet Ignition Engine at High Dilution Rate (~40%), SAE Tech. Pap. (2021) 1–16. https://doi.org/10.4271/2021-01-0455.

50. S. Tolou, H. Schock, Experiments and modeling of a dual-mode, turbulent jet ignition engine, Int. J. Engine Res. 21 (2020) 966–986. https://doi.org/10.1177/1468087419875880.

51. R.T. Vedula, R. Song, T. Stuecken, G.G. Zhu, H. Schock, Thermal efficiency of a dual-mode turbulent jet ignition engine under lean and near-stoichiometric operation, Int. J. Engine Res. 18 (2017) 1055–1066. https://doi.org/10.1177/1468087417699979.

52. K.N. Sok Ratnak, Jin Kusaka, Yasuhiro Daisho, Kei Yoshimura, Experiments and Simulations of a Lean-Boost Spark Ignition Engine for Thermal Efficiency Improvement, SAE Int. J. Engines. 9 (2016) 379–396. https://doi.org/SAE Int. J. Engines 9(1):379-396, 2016.

53. R. Song, R.T. Vedula, G. Zhu, H. Schock, A control-oriented combustion model for a turbulent jet ignition engine using liquid fuel, Int. J. Engine Res. 19 (2018) 813–826. https://doi.org/10.1177/1468087417731698.

54. M. Bunce, H. Blaxill, W. Kulatilaka, N. Jiang, The effects of turbulent jet characteristics on engine performance using a pre-chamber combustor, SAE Tech. Pap. 1 (2014). https://doi.org/10.4271/2014-01-1195.

55. R.P. Roethlisberger, D. Favrat, Investigation of the prechamber geometrical configuration of a natural gas spark ignition engine for cogeneration: Part II. Experimentation, Int. J. Therm. Sci. 42 (2003) 239–253. https://doi.org/10.1016/S1290-0729(02)00024-8.

56. B.C. Thelen, E. Toulson, A computational study on the effect of the orifice size on the performance of a turbulent jet ignition system, Proc. Inst. Mech. Eng. Part D J. Automob. Eng. 231 (2017) 536–554. https://doi.org/10.1177/0954407016659199.

57. G. Gentz, B. Thelen, E. Toulson, P. Litke, J. Hoke, Combustion Visualization, Performance, and CFD Modeling of a Pre-Chamber Turbulent Jet Ignition System in a Rapid Compression Machine, SAE Int. J. Engines. 8 (2015) 538–546. https://doi.org/10.4271/2015-01-0779.

58. I. Saanum, M. Bysveen, P. Tunestål, B. Johansson, Lean Burn Versus Stoichiometric Operation with EGR and 3-Way Catalyst of an Engine Fueled with Natural Gas and Hydrogen Enriched Natural Gas, SAE Tech. Pap. (2007). https://doi.org/10.4271/2007-01-0015.

59. G. Surnilla, R. Soltis, J. Hilditch, C. House, T. Clark, M. Gerhart, Intake Oxygen Sensor for EGR Measurement, SAE Tech. Pap. 2016-April (2016). https://doi.org/10.4271/2016-01-1070.

60. Gamma Technologies, Engine Performance Application Manual, Gamma Technologies

LLC, 2019.

61. K.J. Patton, R.C. Nitschke, J.B. Heywood, Development and evaluation of a friction model for spark-ignition engines, SAE Tech. Pap. (1989). https://doi.org/10.4271/890836.

62. Horsepower Required for Compressing Air - Womack Machine Supply Company, (n.d.). https://www.womackmachine.com/engineering-toolbox/data-sheets/horsepower-required-for-compressing-air/ (accessed July 22, 2021).

63. B. Ellies, C. Schenk, P. Dekraker, Benchmarking and Hardware-in-the-Loop Operation of a 2014 MAZDA SkyActiv 2.0L 13:1 Compression Ratio Engine, SAE Tech. Pap. (2016). https://doi.org/10.4271/2016-01-1007.

64. F. Torres, M. Avelar, F. Antonio, R. Filho, R. Berlini, I. Torres, M. Avelar, 1D NUMERICAL MODEL OF SI ENGINE USING GT-POWER CODE NUMERICAL MODEL OF SI ENGINE USING GT-POWER CODE Heitor Belfort de Sousa Gama, (2019) 1–9.

65. M. Yıldız, B. Albayrak Çeper, Zero-dimensional single zone engine modeling of an SI engine fuelled with methane and methane-hydrogen blend using single and double Wiebe Function: A comparative study, Int. J. Hydrogen Energy. 42 (2017) 25756–25765. https://doi.org/10.1016/j.ijhydene.2017.07.016.

66. J. Liu, C.E. Dumitrescu, Single and double Wiebe function combustion model for a heavy-duty diesel engine retrofitted to natural-gas spark-ignition, Appl. Energy. 248 (2019) 95–103. https://doi.org/10.1016/j.apenergy.2019.04.098.

67. V. Giglio, A. di Gaeta, Novel regression models for wiebe parameters aimed at 0D combustion simulation in spark ignition engines, Energy. 210 (2020) 118442. https://doi.org/10.1016/j.energy.2020.118442.

68. J. Galindo, H. Climent, B. Plá, V.D. Jiménez, Correlations for Wiebe function parameters for combustion simulation in two-stroke small engines, Appl. Therm. Eng. 31 (2011) 1190–1199. https://doi.org/10.1016/j.applthermaleng.2010.12.020.

69. F. Maroteaux, C. Saad, F. Aubertin, Development and validation of double and single Wiebe function for multi-injection mode Diesel engine combustion modelling for hardware-in-the-loop applications, Energy Convers. Manag. 105 (2015) 630–641. https://doi.org/10.1016/j.enconman.2015.08.024.

70. S. Awad, E.G. Varuvel, K. Loubar, M. Tazerout, Single zone combustion modeling of biodiesel from wastes in diesel engine, Fuel. 106 (2013) 558–568. https://doi.org/10.1016/j.fuel.2012.11.051.

71. Y. Sun, H. Wang, C. Yang, Y. Wang, Development and validation of a marine sequential turbocharging diesel engine combustion model based on double Wiebe function and partial least squares method, Energy Convers. Manag. 151 (2017) 481–495. https://doi.org/10.1016/j.enconman.2017.08.085.

72. P.C. Aristotelis Babajimopoulos, MODEL-BASED ASSESSMENT OF TWO VARIABLE CAM TIMING STRATEGIES FOR HCCI ENGINES: RECOMPRESSION VS. REBREATHING, (2009) 1–14.

73. C. Mishra, P.M.V. Subbarao, Design, development and testing a hybrid control model for RCCI engine using double Wiebe function and random forest machine learning, Control Eng. Pract. 113 (2021) 104857. https://doi.org/10.1016/j.conengprac.2021.104857.

74. S. Hu, H. Wang, C. Yang, Y. Wang, Burnt fraction sensitivity analysis and 0-D modelling of common rail diesel engine using Wiebe function, Appl. Therm. Eng. 115 (2017) 170–177. https://doi.org/10.1016/j.applthermaleng.2016.12.080.

75. H. Wu, M.F. Li, A Hardware-in-the-Loop (HIL) Bench Test of a GT-Power Fast Running Model for Rapid Control Prototyping (RCP) Verification, SAE Tech. Pap. (2016). https://doi.org/10.4271/2016-01-0549.

76. E. Pipitone, A new simple friction model for S.I. engine, SAE Tech. Pap. 4970 (2009). https://doi.org/10.4271/2009-01-1984.

77. D. Sandoval, J.B. Heywood, An improved friction model for spark-ignition engines, SAE Tech. Pap. (2003). https://doi.org/10.4271/2003-01-0725.

78. S.K. Chen, P.F. Flynn, Development of a single cylinder compression ignition research engine, SAE Tech. Pap. (1965). https://doi.org/10.4271/650733.

79. Gamma Technologies, GT-SUITE Engine Performance Application Manual, in: 2019.

80. Gamma Technologies, GT-SUITE Vehicle Driveline and HEV Application Manual, (2019).

81. S.G. Wirasingha, A. Emadi, Classification and review of control strategies for plug-in hybrid electric vehicles, IEEE Trans. Veh. Technol. 60 (2011) 111–122. https://doi.org/10.1109/TVT.2010.2090178.

82. A.M. Ali, D. Söffker, Towards optimal power management of hybrid electric vehicles in real-time: A review on methods, challenges, and state-of-the-art solutions, Energies. 11 (2018) 1–24. https://doi.org/10.3390/en11030476.

83. J. Benajes, A. García, J. Monsalve-Serrano, S. Martínez-Boggio, Optimization of the parallel and mild hybrid vehicle platforms operating under conventional and advanced combustion modes, Energy Convers. Manag. 190 (2019) 73–90. https://doi.org/10.1016/j.enconman.2019.04.010.

84. R. Rolt, R. Douglas, P. Nockemann, R. Best, Full battery pack Modelling: An electrical Sub-Model using an EECM for HEV applications, SAE Tech. Pap. 2019-April (2019) 1–10. https://doi.org/10.4271/2019-01-1203.

85. R. Ahmed, J. Gazzarri, S. Onori, S. Habibi, R. Jackey, K. Rzemien, J. Tjong, J. Lesage,

Model-Based Parameter Identification of Healthy and Aged Li-ion Batteries for Electric Vehicle Applications, SAE Int. J. Altern. Powertrains. 4 (2015) 233–247. https://doi.org/10.4271/2015-01-0252.

86. H. He, R. Xiong, H. Guo, S. Li, Comparison study on the battery models used for the energy management of batteries in electric vehicles, Energy Convers. Manag. 64 (2012) 113–121. https://doi.org/10.1016/j.enconman.2012.04.014.

87. A. Nikolian, J. De Hoog, K. Fleurbay, J. Timmermans, P. Van De Bossche, J. Van Mierlo, Classification of Electric modelling and Characterization methods of Lithium-ion Batteries for Vehicle Applications, Eur. Electr. Veh. Congr. (2014) 1–15.

88. H. He, R. Xiong, J. Fan, Evaluation of lithium-ion battery equivalent circuit models for state of charge estimation by an experimental approach, Energies. 4 (2011) 582–598. https://doi.org/10.3390/en4040582.

89. M. Daowd, N. Omar, B. Verbrugge, P. Van Den Bossche, J. Van Mierlo, Battery models parameter estimation based on Matlab/Simulink®, EVS 2010 - Sustain. Mobil. Revolut. 25th World Batter. Hybrid Fuel Cell Electr. Veh. Symp. Exhib. 2 (2010).

90. C. Zhang, C. Zhang, J. Liu, S.M. Sharkh, Identification of dynamic model parameters for lithium-ion batteries used in hybrid electric vehicles, High Technol. Lett. 16 (2010) 6–12. https://doi.org/10.3772/j.issn.1006-6748.2010.01.002.

91. M. Chen, G.A. Rincón-Mora, Accurate electrical battery model capable of predicting runtime and I-V performance, IEEE Trans. Energy Convers. 21 (2006) 504–511. https://doi.org/10.1109/TEC.2006.874229.

92. S. Lee, J. Cherry, M. Safoutin, J. McDonald, M. Olechiw, Modeling and Validation of 48V Mild Hybrid Lithium-Ion Battery Pack, SAE Int. J. Altern. Powertrains. 7 (2018) 273–287. https://doi.org/10.4271/2018-01-0433.

93. S. Lee, B. Lee, J. McDonald, E. Nam, Modeling and validation of lithium-ion automotive battery packs, SAE Tech. Pap. 2 (2013). https://doi.org/10.4271/2013-01-1539.

94. S. Lee, B. Lee, J. McDonald, L.J. Sanchez, E. Nam, Modeling and validation of power-split and P2 parallel hybrid electric vehicles, SAE Tech. Pap. 2 (2013). https://doi.org/10.4271/2013-01-1470.

95. AVTA: 2013 Chevrolet Malibu HEV Testing Results | Department of Energy, (n.d.). https://www.energy.gov/eere/vehicles/downloads/avta-2013-chevrolet-malibu-hev-testing-results (accessed November 5, 2020).

96. Ford 2.7L EcoBoost Nano Engine Info, Power, Specs, Wiki, (n.d.). https://fordauthority.com/fmc/ford-motor-company-engines/ford-ecoboost-family/ford-2-7l-ecoboost-nano-engine/ (accessed March 23, 2022).

97. P. Dekraker, M. Stuhldreher, Y. Kim, Characterizing Factors Influencing SI Engine

Transient Fuel Consumption for Vehicle Simulation in ALPHA, SAE Int. J. Engines. 10 (2017) 529–540. https://doi.org/10.4271/2017-01-0533.

98. J.M. Miller, Annual Progress Report for the Power Electronics and Electric Motors Program, 2013.

99. P. Dekraker, J. Kargul, A. Moskalik, K. Newman, M. Doorlag, D. Barba, Fleet-Level Modeling of Real World Factors Influencing Greenhouse Gas Emission Simulation in ALPHA, SAE Int. J. Fuels Lubr. 10 (2017) 217–235. https://doi.org/10.4271/2017-01-0899.

100. K. Newman, J. Kargul, D. Barba, Benchmarking and Modeling of a Conventional Mid-Size Car Using ALPHA, SAE Tech. Pap. 2015-April (2015). https://doi.org/10.4271/2015-01-1140.

101. Energy Systems D3 2013 Chevrolet Malibu Eco, (n.d.) https://www.anl.gov/es/energy-systems-d3-2013-chev.

102. N. Highway, T. Safety, Environmental Protection Agency Department of Emission Standards and Corporate, Environ. Prot. Agency. (2010) 1–25728.

103. S. Zhu, S. Akehurst, A. Lewis, H. Yuan, A review of the pre-chamber ignition system applied on future low-carbon spark ignition engines, Renew. Sustain. Energy Rev. 154 (2022) 111872. https://doi.org/10.1016/j.rser.2021.111872.

104. S. Zhang, X. Duan, Y. Liu, G. Guo, H. Zeng, J. Liu, M.C. Lai, A. Talekar, Z. Yuan, Experimental and numerical study the effect of combustion chamber shapes on combustion and emissions characteristics in a heavy-duty lean burn SI natural gas engine coupled with detail combustion mechanism, Fuel. 258 (2019) 116130. https://doi.org/10.1016/j.fuel.2019.116130.

105. S.K. Mahendar, V. Venkataraman, A.C. Erlandsson, The Impact of Miller Valve Timing on Combustion and Charging Performance of an Ethanol- And Methanol-Fueled Heavy-Duty Spark Ignition Engine, SAE Int. J. Engines. 14 (2021) 3–14. https://doi.org/10.4271/03-14-05-0044.

106. N. Türköz, B. Erkuş, M.I. Karamangil, A. Sürmen, N. Arslanoğlu, Experimental investigation of the effect of E85 on engine performance and emissions under various ignition timings, Fuel. 115 (2014) 826–832. https://doi.org/10.1016/j.fuel.2013.03.009.

107. S.O. Akansu, S. Tangöz, N. Kahraman, M.İ. İlhak, S. Açıkgöz, Experimental study of gasoline-ethanol-hydrogen blends combustion in an SI engine, Int. J. Hydrogen Energy. 42 (2017) 25781–25790. https://doi.org/10.1016/j.ijhydene.2017.07.014.

108. S.M.M.E. Ayad, C.R.P. Belchior, G.L.R. da Silva, R.S. Lucena, E.S. Carreira, P.E.V. de Miranda, C. Ji, S. Wang, S.O. Akansu, S. Tangöz, N. Kahraman, M.İ. İlhak, S. Açıkgöz, P. Geng, E. Cao, Q. Tan, L. Wei, Experimental study of gasoline-ethanol-hydrogen blends combustion in an SI engine, Int. J. Hydrogen Energy. 45 (2017) 523–534.

https://doi.org/10.1016/j.rser.2016.12.080.

109. X. Duan, Y. Liu, J. Liu, M.C. Lai, M. Jansons, G. Guo, S. Zhang, Q. Tang, Experimental and numerical investigation of the effects of low-pressure, high-pressure and internal EGR configurations on the performance, combustion and emission characteristics in a hydrogen-enriched heavy-duty lean-burn natural gas SI engine, Energy Convers. Manag. 195 (2019) 1319–1333. https://doi.org/10.1016/j.enconman.2019.05.059.

110. X. Duan, Y. Liu, M.C. Lai, G. Guo, J. Liu, Z. Chen, B. Deng, Effects of natural gas composition and compression ratio on the thermodynamic and combustion characteristics of a heavy-duty lean-burn SI engine fueled with liquefied natural gas, Fuel. 254 (2019) 115733. https://doi.org/10.1016/j.fuel.2019.115733.

111. P. Geng, E. Cao, Q. Tan, L. Wei, Effects of alternative fuels on the combustion characteristics and emission products from diesel engines: A review, Renew. Sustain. Energy Rev. 71 (2017) 523–534. https://doi.org/10.1016/j.rser.2016.12.080.

112. J. Wang, H. Chen, B. Liu, Z. Huang, Study of cycle-by-cycle variations of a spark ignition engine fueled with natural gas-hydrogen blends, Int. J. Hydrogen Energy. 33 (2008) 4876–4883. https://doi.org/10.1016/j.ijhydene.2008.06.062.

113. E. Toulson, H.C. Watson, W.P. Attard, The Lean Limit and Emissions at Near-Idle for a Gasoline HAJI System with Alternative Pre-Chamber Fuels, SAE Tech. Pap. 2007-Septe (2007). https://doi.org/10.4271/2007-24-0120.

114. P. Sementa, F. Catapano, S. Di Iorio, B.M. Vaglieco, Experimental Investigation of a Fueled Prechamber Combustion in an Optical Small Displacement SI Methane Engine, SAE Tech. Pap. 2019-Septe (2019). https://doi.org/10.4271/2019-24-0170.

115. R.B.R. da Costa, A.F. Teixeira, F.A. Rodrigues Filho, F.J.P. Pujatti, C.J.R. Coronado, J.J. Hernández, E.E.S. Lora, Development of a homogeneous charge pre-chamber torch ignition system for an SI engine fuelled with hydrous ethanol, Appl. Therm. Eng. 152 (2019) 261–274. https://doi.org/10.1016/j.applthermaleng.2019.02.090.

116. J.A.O. Ander Ruiz Zardoya, Iñaki Loroño Lucena, Iñigo Oregui Bengoetxea, Research on an internal combustion engine with an injected pre-chamber to operate with low methane number fuels for future gas flaring reduction, Energy. (2022) 100310. https://doi.org/10.1016/j.energy.2022.124096.

117. P. Liu, L. Zhong, L. Zhou, H. Wei, The ignition characteristics of the pre-chamber turbulent jet ignition of the hydrogen and methane based on different orifices, Int. J. Hydrogen Energy. 46 (2021) 37083–37097. https://doi.org/10.1016/j.ijhydene.2021.08.201.

118. R.B.R. da Costa, F.A. Rodrigues Filho, T.A.A. Moreira, J.G.C. Baêta, M.E. Guzzo, J.L.F. de Souza, Exploring the lean limit operation and fuel consumption improvement of a homogeneous charge pre-chamber torch ignition system in an SI engine fueled with a gasoline-bioethanol blend, Energy. 197 (2020).

https://doi.org/10.1016/j.energy.2020.117300.

119. C.E.C. Alvarez, V.R. Roso, N.D.S.A. Santos, A.T. Fernandes, R.M. Valle, Combustion analysis in a SI engine with homogeneous and stratified pre-chamber system, SAE Tech. Pap. (2018). https://doi.org/10.4271/2018-36-0112.

120. J.P. Szybist, D. Splitter, Effects of Fuel Composition on EGR Dilution Tolerance in Spark Ignited Engines, SAE Int. J. Engines. 9 (2016) 819–831. https://doi.org/10.4271/2016-01-0715.

121. P. Hlaing, M. Echeverri Marquez, P. Burgos, E. Cenker, M. Ben Houidi, B. Johansson, Analysis of Fuel Properties on Combustion Characteristics in a Narrow-Throat Pre-Chamber Engine, SAE Tech. Pap. (2021). https://doi.org/10.4271/2021-01-0474.

122. J. Rohwer, T. Han, A. Shah, T. Rockstroh, Investigations into EGR dilution tolerance in a pre-chamber ignited GDI engine, Int. J. Engine Res. (2022) 146808742210847. https://doi.org/10.1177/14680874221084777.